KAUNAS UNIVERSITY OF TECHNOLOGY

PAULIUS PALEVIČIUS

OPTICAL INTERFEROMETRY BASED METHODS FOR INVESTIGATIONS OF DYNAMICAL PROCESSES IN MICROSYSTEMS

Doctoral Dissertation
Technological Sciences, Mechanical Engineering (09T)

2015, Kaunas

The doctoral thesis was prepared in Kaunas University of Technology, Faculty of Mathematics and Natural Sciences, Department of Mathematical Modeling during 2011-2015. The studies were supported by the State Studies Foundation and Research Council of Lithuania.

Scientific supervisor:

Prof. Dr. Habil. Minvydas Kazys Ragulskis (Kaunas University of Technology, Technological Sciences, Mechanical Engineering – 09T).

Doctoral Dissertation is available on the internet (http://ktu.edu).

ISBN 978-609-02-1140-3

KAUNO TECHNOLOGIJOS UNIVERSITETAS

PAULIUS PALEVIČIUS

DINAMINIŲ PROCESŲ MIKROSISTEMOSE TYRIMAS OPTINĖS INTERFEROMETRIJOS METODAIS

Daktaro disertacija
Technologijos mokslai, mechanikos inžinerija (09T)

2015, Kaunas

Disertacija rengta 2011–2015 m. Kauno technologijos universiteto Matematikos ir gamtos mokslų fakulteto Matematinio modeliavimo katedroje. Mokslinius tyrimus rėmė Lietuvos Valstybinis studijų fondas ir Lietuvos mokslo taryba.

Mokslinis vadovas:

Prof. habil. dr. Minvydas Kazys Ragulskis (Kauno technologijos universitetas, technologijos mokslai, mechanikos inžinerija – 09T).

Su disertacija galima susipažinti internete (http://ktu.edu).

ISBN 978-609-02-1140-3

CONTENTS

LIST OF FIGURES

SYMBOLS AND ABBREVIATIONS

MEMS	Micro Electro Mechanical Systems
CGH	Computer Generated Holography
FEM	Finite Element Method
DOE	Diffractive Optical Elements
FFT	Fast Fourier Transform
DFT	Discrete Fourier Transform
GS	Gerchber-Saxton
VCS	Visual Cryptography Scheme
DVC	Dynamic Visual Cryptography
DVCS	Dynamic Visual Cryptography Scheme
HVCS	Halftone Visual Cryptography Scheme

INTRODUCTION

Relevance of the work

MEMS devices are being integrated with various commercial products such as accelerometers (used to control airbag deployment in vehicles), blood pressure sensors, consumer electronics, medical, communications, defense and other areas. The research and development of MEMS devices depend on scientific fields of mechanical engineering, materials science, electrical engineering, chemical engineering, fluid engineering, optics, instrumentation and packaging. Despite the small size, MEMS devices achieve better performance, reliability, volume, weight and lower costs. MEMS and MOEMS components typically have moving parts. Thus a reliable and traceable metrology techniques are required for testing and development.

Optical methods, based on interferometric techniques, has been successfully applied for MEMS testing. Double exposure moiré and laser holography methods have been successfully applied for static MEMS metrological measurements. Time-averaged moiré and holography methods are used for vibration analysis by generating time-averaged patterns of interference fringes. Accurate interpretation of experimental results is one of the important factors enabling the minimization of the general uncertainty budget. Thus effective techniques are needed for correct interpretation of optical experimental patterns of interference fringes. Methods for fringe identification, such as phase shifting technique, has been successfully applied for double exposure techniques. Though they have limitations for vibrations analysis with high frequencies, as it requires multiple interferograms with a phase shift. Another approach is fringe centerlines identification method though reliable interpretation of undeveloped and fringes contaminated by noise is a difficult task. An appropriate application of time-averaged holography for MEMS analysis performing nonlinear vibrations also has its limits.

A novel application of dynamic visual cryptography has been applied for mechanical vibration testing. In this method, the encoded cover image is fixed on the head of a vibration shaker system, and a human operator can detect the parameters of the vibration processes. A simple look at vibrating cover image diagnoses a problem with the system. This method can be successfully applied for effective experimental investigation and testing of MEMS devices.

The object of the research is interferometry based methods for analysis of microelectromechanical systems.

The aim of the work is to develop optical interferometric techniques for identification, analysis and monitoring of microelectromechanical systems.

The main tasks of this research were as follows:

1. to perform a literature analysis of optical interferometric techniques for identification, analysis and monitoring of microelectromechanical systems.
2. to investigate the methods for the interpretation of time-averaged holographic fringes produced by non-linear oscillations of microelectromechanical systems.

3. to develop a scheme for the identification of experimental optical images of complex, undeveloped interferometric fringes embedded in high background noise.
4. to integrate computer generated holography and dynamic visual cryptography methods for monitoring parameters of microelectromechanical systems.

Methods, software, and experimental tools

- Moiré and holography based methods used for the analysis of microelectromechanical systems.
- Computer vision techniques and mathematical morphology methods are used for processing of experimental images.
- COMSOL Multiphysics (the scientific package for physics-based finite element method modeling) is used for simulation of microelectromechanical systems.
- Matlab R2012b was used to access computational data, modeled using COMSOL Multiphysics. Computational optical model was created using standard Matlab functions to demonstrate time-averaged fringe formation. Matlab was also used to implement Gerchberg-Saxton algorithm and to integrate it with an implementation of digital visual cryptography, to demonstrate the validity of the proposed method.
- Python (including NumPy and SciPy packages) has been used for developing computational tools for centerline identification in experimental optical images.
- Mahotas Python package was used for performing mathematical morphological operations.
- Graphics processing tools, such as GIMP, Inkscape, Adobe Photoshop were used for experimental image processing.
- Shadow moiré experimental setup was used to record deformation field of the printed circuit board.
- Holographic PRISM system was used for experimental investigation of microelectromechanical systems.

Defended statements

- Time-averaged fringes generated by microelectromechanical systems cannot be interpreted by using straightforward techniques based on the assumptions that analyzed systems oscillate according to the harmonic law of motion.
- Straightforward identification of centerlines of time-averaged fringes is not sufficient for the optical interpretation of complex patterns of fringes (where some fringes are not fully developed, or the whole interferogram is contaminated with noise). Continuation and interpolation of fringe centerlines help to interpret even complex interferograms.

- Optical integration of computer generated holography, and dynamic visual cryptography enables to monitor parameters of MEMS elements. Computational experiments prove the validity of the proposed experimental technique.

Scientific novelty and significance

- The proposed technique for the interpretation of time-averaged fringes produced by chaotic oscillations enables to validate actual dynamic displacements of MEMS components. Developed finite element model of a fixed-fixed beam performing nonlinear oscillations provides valuable insight into the motion of investigated system.
- Continuation and extrapolation of fringe centerlines help to interpret interferometric fringes that are not fully developed and contains noise. Such approach is important for the identification of microelectromechanical systems when using interferometric techniques.
- Proposed optical integration of computer generated holography and dynamical visual cryptography. Such optical technique is important for MEMS investigation.

Approval of the results

The major results of the dissertation were published in 8 publications, 4 of which are published in the Institute for Scientific Information (ISI) as the main list of publications with citing indexes; and other 4 were published in peer-reviewed journals and conferences. The topics covered in the dissertation were presented at two international conferences. The results of the research were also presented in the exhibition "KTU Technorama 2012".

Scope and structure of the dissertation

Doctoral dissertation consists of an introduction, 4 major sections, conclusions, list of references and list of the author's publications. There are 46 figures, and the list of 117 cited sources within the main part of the dissertation.

The relevance of the work and problem is discussed in the introduction. Also, the aim of the work and main tasks are formulated. Methods of investigations, software, and experimental tools are provided in this section, together with defended statements, scientific novelty significance, approval of the results, and the scope and structure of this thesis are presented.

The literature analysis on the aim and objectives of this thesis is presented in the first chapter. Interpretation of time-averaged holographic fringes produced by nonlinear oscillations of MEMS devices is discussed in the second chapter. Development of the computational tools for the identification of experimental optical images of complex, undeveloped interferometric fringes embedded in high background noise is presented in the third chapter. Optical integration of computer generated holography, and

dynamic visual cryptography is presented in the fourth chapter. Finally, conclusions, bibliographic references, author‘s scientific publications, and acknowledgments, are presented.

1. LITERATURE REVIEW

MEMS (microelectromechanical systems) are systems that integrate mechanical and electrical elements to perform certain functions. The research, development and manufacturing of MEMS began back in 1960's and has been gaining traction since then (Wise, 2007). Companies started to deploy MEMS components in numerous commercial products such as accelerometers (used to control airbag deployment in vehicles) and pressure sensors (used in the medical sector) in mid-1990's. It resulted in an increasing application, manufacturing and integration of MEMS devices. Consumer electronics, as they are today, would impossible without integration of MEMS devices. Today MEMS are used in many areas such as automotive, electronics, medical, communications, defense and others (Rai-Choudhury, 2000). The research, design and manufacturing of MEMS depends on mechanical, chemical, electrical, fluid, engineering, materials science, chemistry, optics, instrumentation, and packaging, making it an interdisciplinary field.

Because of MEMS size (ranging from micrometers to millimeters), it is possible to integrate them into a wide range of systems, such as smartphones, cars, printers, projectors, blood pressure sensors, mass storage devices, and so on. MEMS can be classified as sensors or as actuators (transducers). The most typical transducers are mechanical, radiation, thermal, magnetic, chemical and biological (Rai-Choudhury, 2000). Mechanical sensors are based on piezoresistive, piezoelectric, resonant or capacitive sensing mechanisms and are used for sensing strains, force, and displacements. Radiation sensors are photodiodes, charge-coupled devices, and pyroelectric sensors. Thermal sensors can be categorized as thermo-mechanical sensors, thermoresistive sensors, and thermocouples. Typical chemical sensors are chemo resistors, chemo capacitors, chemomechanical, calorimetric sensors. Microfluidic devices are also well known for their usage as flow channels, flow sensors, valves, pumps, and droplet generators for chemical analysis, drug delivery, biological sensing, environmental monitoring (Moo-Young, 2011). Despite a small size, MEMS increases performance and reliability, and it also has reduced physical size, volume, weight, and cost.

Much focus of recent research has been inf the fabrication of MEMS. Three general types of fabrication methods are bulk micromachining, surface micromachining and high-aspect-ratio micromachining (HARM) (Mamilla et al., 2014). Bulk micromachining technique is based on the selective removal of the substrate material in order to realize miniaturized mechanical components. The removal is performed by using chemical or physical techniques (Kovacs et al., 1998). Deposition and etching of different structural layers on top of the substrate is performed in case of surface micromachining (Bustillo et al., 1998). High-aspect-ratio micromachining (HARM) involves micromachining as a tooling step followed by injection molding or embossing and, if required, by electroforming. HARM method employs a technique called LIGA (Lithography, Electroplating, and Molding) (Q. Wang et al., 2009). Typical materials used in MEMS fabrication are silicon, polymers, metals and, ceramics (Mamilla et al.,

2014).

It is obvious that a reliability of MEMS is crucial, because of its application in sensitive areas, such as automotive and aerospace safety systems, chemical and biological warfare sensors, and others (Iannacci, 2015). It is critical to ensure the reliability in all steps of development of MEMS devices. One should choose appropriate technology, materials, and packaging solutions. In order to solve this problem, various techniques, methods, and analysis for different types of MEMS were proposed in recent years, such as fast reliability assessment method for Si MEMS-based microcantilever beams (Rafiee et al., 2014), enhancement of RF MEMS switch reliability through an active anti-stiction heat-based mechanism (Iannacci et al., 2010), investigation of packaging influences on the reliability of MEMS resonators (Zaal et al., 2008), and others.

The area of optics and micro-optics can be applied directly to a design of MEMS and is called MOEMS (micro-opto-electromechanical systems). MOEMS are used as waveguides, filters, modulators, micro mirrors, optical switches, and others (Y.-C. Chen et al., 2012; Comtois et al., 1999; Guan et al., 2013). A widely used optical components in MEMS are diffractive optical elements (DOE). DOE is an element that modifies wavefronts by segmenting and redirecting the segments through the use of interference and phase control (Shea, 2004). DOE integration in the optical setup allows to change and control the shape of a laser beam. It accomplishes almost the same optical functionality as elements of the refractive optics, such as optical lenses, prisms, and spheres. Diffractive optical elements are much smaller in size and weighs less compared to standard elements of the refractive optics. DOEs can be used in the form of a transparency or a reflecting mirror. Various techniques are used for the manufacturing of DOEs, such as diamond turning (Smith, 1982), half-tone masking technique (Quentel et al., 2001), electron or ion beam writing (Turunen, 1997; Teijido et al., 1989), and others. E-beam lithography is the technique of choice for applications, that require high quality and sophisticated hologram masters – though e-beam direct writing has the disadvantage of a higher fabrication cost (Gao et al., 2002). The use of regular electron-beam lithography for the fabrication of a computer generated hologram (CGH) is discussed in (Teijido et al., 1989). Most DOEs production technologies have grown from microelectronics and MEMS microfabrication techniques.

Advanced strain measurement and control tools are regarded as primary technology drivers in such industries as MEMS fabrication and high-precision machine tools manufacturing (Shang et al., 2005; Sciammarella et al., 2003; Han, 1998). Optics can be employed in process of designing MEMS for metrological measurements and reliability evaluation, such as dynamic characterization of MEMS diaphragm, using time-averaged in-line digital holography (Singh, Miao, et al., 2007) or static and dynamic characterization of microstructures using acoustic-optic-modulated-stroboscopic-interferometry (Quentel et al., 2001). Most conventional measurement techniques for MEMS are interferometry, holography, image correlation, and structured light based methods. Traditional whole field holographic and moiré based interferometric methods can be used in order to estimate displacements of MEMS objects.

Both methods can be also used for vibration analysis by generating time-averaged patterns of interference fringes. Though sensitivity of the holographic method is better compared to moiré method, moiré method has been successfully applied for deformation analysis of MEMS structures (Z. Liu et al., 2010; Xie et al., 2004). The correct interpretation of results of the experimental measurements is one of the main factors enabling the minimization of the general uncertainty budget. Particularly this is important in projection and shadow moiré applications, where problems, such as non-uniform distribution of moiré fringes in the observed area, poor lighting conditions, complex surfaces of the investigated objects, and noisy backgrounds do not allow a reliable interpretation of the optical measurement results.

1.1. Moiré methods for identification of object surface deformations

The term moiré has been adopted to describe the interaction of two superimposed gratings in the literature of optics. It has origins in a French word for watered, relating moiré to watered silk that has patterns with brighter and darker bands and resembles moiré fringe patterns. Moiré patterns are obtained by the mechanical interference of lines by the superimposed network of gratings. Moiré method can be used for measurement of surface topography, deformation, displacements, strain, and vibrations. The other advantage of this technique is that it has a wide range of measurement sensitivity. The sensitivity depends on the pitch of the gratings used and the optical imaging system. The most common methods are geometric moiré, shadow moiré, projection moiré, reflection moiré, moiré interferometry, and time-averaged geometric moiré. The main advantage of shadow, reflection and projection moiré techniques is that moiré grating is formed by an array of grayscale lines onto the surface of the deformable body instead of physically drawing these lines. This feature is important in applications when the graphical formation of grating lines is complicated or even impossible. Moiré techniques allow both – in-plane and out-of-plane measurements. The in-plane method can be applied for measuring creep, residual stress, fracture dynamic loading and thermal deformations. The out-of-plane method is used to measure out-of-plane displacements.

1.1.1. Fundamentals of moiré technique

Gratings are arrays of opaque and transparent which a are straight and has equal spaces (though concentric circles, cross gratings and dots can be used in some situations). Two gratings are needed to form a pattern of moiré interference fringes. The with of opaque and transparent lines is called pitch p. The number of lines per unit length is called density d. The following conditions has to be satisfied to get a map well–developed moiré fringes (Sharpe et al., 2008):

- bars and spaces have the equal size,
- the two gratings are well defined,
- the angle of intersection of the two gratings is small,

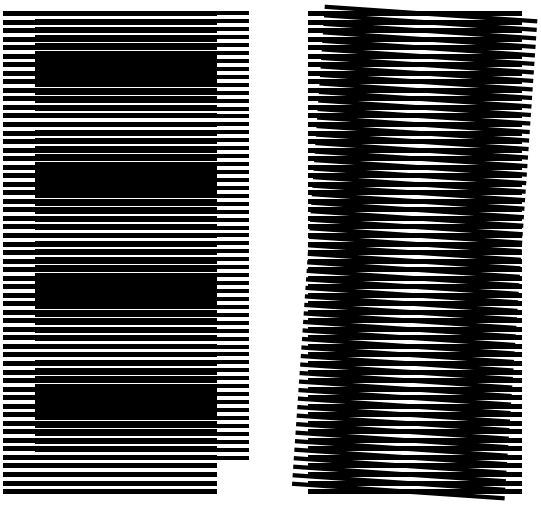

Figure 1.1: Formation of moiré fringes due to rotation of gratings a) and difference in pitch of gratings b).

- the ratio of the pitches of the gratings is small.

In the first case, we have two gratings with slightly different pitches p_1 and p_2 as shown in Figure 1.1. The light fringes are observed in areas where two opaque strips coincide. In this case, the transmitted light intensity is maximum. The dark fringes are observed when transparent strips overlap opaque strips. In this case transmitted light intensity is minimum. Let's denote δ as a distance between fringe centers and m as the number of pitches of the coarser grating that fall within δ. In this case, the distance between centers of fringes

$$\delta = mp_1 = (m \pm 1)\, p_2 \tag{1}$$

In this case, from a well-developed pattern of fringes, one can find nominal strain ϵ using equation

$$\epsilon = \frac{p_1}{\delta - p_1} \approx \frac{p_1}{\delta} \tag{2}$$

In the second case, we have interference of two gratings accomplished by rotation of a second grating. Gratings have the same pitch though the second grating is rotated by an angle θ with respect to the first grating. In this case, the distance between centers of fringes is

$$\delta = \frac{p_1 \cos(\theta/2)}{\sin(\theta)} = \frac{p_1}{2\sin(\theta/2)} \tag{3}$$

In case of rotation fringes are perpendicular to the bisector of angle θ. If we have a well-developed pattern of fringes, parameter θ reads:

$$\theta \approx \frac{p_1}{\delta} \tag{4}$$

A more complicated cases of in-plain moiré employment in two dimensions, such as a combination of previous methods, where gratings have different pitches and are rotated respectively to each other, and application of a displacement method for moiré fringe analysis are discussed in (Sharpe et al., 2008). Although geometric moiré is a classic technique, new research is being performed constantly in this area, such as a comparison of in-plane displacement measurement from circular grating moiré fringes using Fourier transformation and graphical analysis (Yen et al., 2012), combination of high resolution transmission electron microscopy and moiré patterns for determination of thickness of in-plane thin films (Valamanesh et al., 2011), reliability prediction of delamination failures of chip warpage model (S. Y. Yang et al., 2012), and others.

1.1.2. Shadow and projection moiré methods

Shadow moiré and projection moiré methods are topography methods used for measuring out-of-plane displacements (Kobayashi et al., 1993; Lehmann et al., 1999; Breque et al., 2004; Meadows et al., 1970; Takasaki, 1970). Both methods are commonly used to measure the profile of surfaces in order to evaluate displacements caused by temperature, humidity, mechanical load, or other variables of diffusely reflecting objects. Because its optical arrangement is cheap and easy to implement in industry environment, the technique has been widely used and well studied in different fields, such as structural mechanics, impact testing and vibration measurement (Du et al., 2014). The most common setup of projection moiré comprises the projection grating, placed in front of and a camera. The shadow moiré technique is different from the projection moiré as grating is placed close to the object, and the shadow of the object is observed through the grating. The interfere of grating lines with the shadow lines produces interference fringes. Centerlines of these interference fringes represent surface contour map.

A linear reference grating (comprised of black and transparent stripes) of pitch g is placed adjacent to the specimen surface. The specimen and grating are illuminated by an incident light source. A well-defined shadow of the reference grating is cast upon the specimen surface and interferes with a reference grating. Superposition of those two gratings forms a moiré pattern of interference fringes. A generic relation between the fringe order N and the gap W reads (Sharpe et al., 2008)

$$W = \frac{g}{\tan\alpha + \tan\beta} N \tag{5}$$

where g is the pitch of the grating; α is the angle between the camera and normal vector of the reference grating; β is the angle between the light source and the normal vector of the reference grating. A more robust shadow moiré setup is shown in Figure 1.2. In this case, the relationship between the fringe order and the gap is

$$W = \frac{g}{\tan\alpha} N \; or \; W = \frac{g}{(D/L)} N \tag{6}$$

α is the angle between the camera and the source of light. In this case a distance from the camera to the specimen L equals the distance from the camera to the source of light D. This arrangement and usage of collimated light assures constant sensitivity across the field and avoids geometrical distortions.

The projection moiré technique allows obtaining the relief of an object. Its principle consists of projecting a sinusoidal grating of parallel lines onto the surface of the object. The illuminated object is photographed in its original condition, and its deformed condition after loads are applied. The superposition of these gratings generates a pattern of moiré fringes. The relief is then deduced from the analysis of the grating observed by a digital camera and the geometric parameters of the setup.

$$W = \frac{g}{\tan \alpha} N \tag{7}$$

where α is an angle between the light source and the camera; N is fringe order at B. This method is used to find the changes in object topography between two or more states. Another approach, where a reference grating is in front of a camera can be used (Sharpe et al., 2008). In this case, a pattern of moiré fringes is formed, and only one object state is used to retrieve a topography of that object.

Various techniques based on the shadow and projection moiré methods are being continuously developed. Shadow moiré technique is frequently used as a method for evaluating warpage of components. Improvements to the metrology have resulted in increasing of its usefulness for evaluating various board-level manufacturing technologies (Geng et al., 2006). Shadow moiré has been also used to determinate Young's modulus of epoxy coated polyethylene micro-cantilever by using phase shifting technique (Lim et al., 2011), and to analyze higher order behavior of sandwich beams using digital projection moiré (Pourvais et al., 2014). Recently, two wavelengths of the projection topography and the synchronization between a the projector and CCD camera were used to treat large-step discontinuities in 3D measured objects (Ryu et al., 2008). Phase-shifting fringe analysis was used to enhance the measurement resolution of the grating projection moiré topography (Kim et al., 1999). A method was developed which uses FFT (Fast Fourier Transform) and signal-demodulating techniques to generate a wrapped phase map from a clear pattern of projection moiré fringes (He et al., 1998). A continuous phase was obtained by using an unwrapping procedure. The accuracy of the method is increased by a digital method for fractional fringe multiplication. Computer-aided moiré methods use the versatility of modern computers not only for practical measurements but also for teaching moiré techniques (Asundi, 1993). Novel and advanced applications of projection moiré are developed continuously, such as using projection moiré for measurement of instantaneous out-of-plane bending of composite plates on the edges of wings subject to bird strikes (Van Paepegem et al., 2008), or using a combination of moiré-filtering and object adapted fringes to monitor the exact position of a rotating fan with seven wings rotating with 100 Hz (Wagemann et al., 1999).

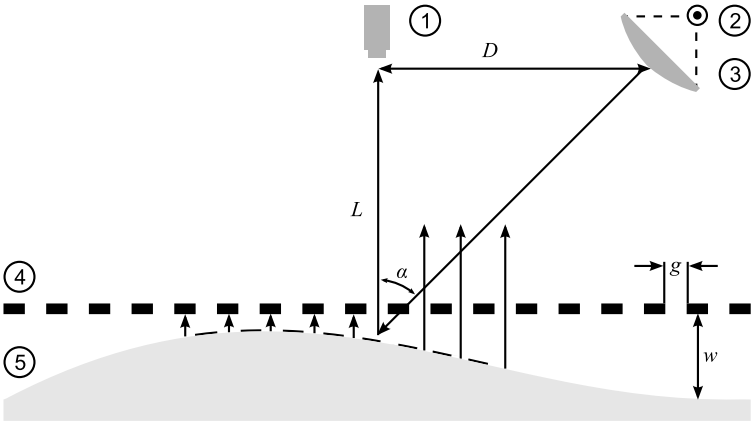

Figure 1.2: A schematic illustration of shadow moiré method. Shadow moiré setup comprises a camera (1), a light source (2), a lens (3), reference grating (4), an object surface (5).

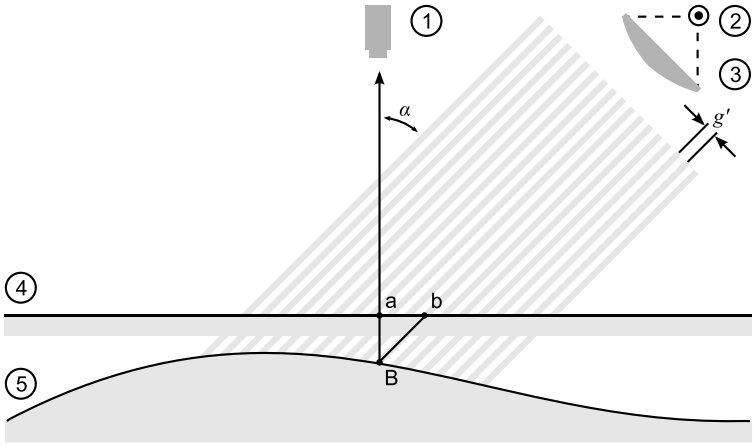

Figure 1.3: A schematic illustration of projection moiré method. Projection moiré setup comprises a camera (1), a light source (2), a lens (3), on object surface in initial state (4), an object surface in deformed state (5).

1.1.3. Time-average geometric moiré

Time-averaged geometric moiré is a dynamic alternative to static double exposure geometric moiré. A single moiré grating is used in time-averaged geometric moiré. An opaque image of the grating is printed on the surface of a vibrating body and time averaging techniques are used to acquire time-averaged moiré fringes (Liang et al., 1979). Exploitation of time-averaged geometric moiré is not limited to optical analysis of vibrating structures. It can be also used for the synthesis of a predefined pattern of time-averaged fringes. Such type of image hiding technique (when the secret image leaks in the form of a time-averaged moiré fringe in an oscillating non-deformable cover image) was first presented in (Ragulskis and Aleksa, 2009). The secret image is embedded into a single cover image by using a stochastic moiré grating. A visual decoding of the secret image can be performed by a human visual system if the amplitude of the harmonic oscillations corresponds to a preselected value. The fact that a human visual system cannot interpret the secret from a static image makes this image hiding technique similar to visual cryptography. Special computational algorithms are required to encode the image, but the decoding is entirely visual. The difference from visual cryptography is that only a single cover image is used and that it should be oscillated to leak the secret.

Lets consider a one-dimensional harmonic moiré grating:

$$F(x) = \frac{1}{2} + \frac{1}{2}\cos\left(\frac{2\pi}{\lambda}x\right) \tag{8}$$

where λ is the pitch of the grating; 1 corresponds to the white color, 0 corresponds to the black color, and all intermediate numerical values of $F(x)$ correspond to an appropriate grayscale level. Lets assume that this moiré grating is oscillated around the state of equilibrium (without being deformed), and a deflection from the state of equilibrium does not depend on x (Ragulskis and Navickas, 2009):

$$u(x,t) = u(t) = a\sin(\omega t + \varphi) \tag{9}$$

where ω is the cyclic frequency; φ is the phase and a is the amplitude of the oscillation. In this case time averaging operator is derived as follows:

$$\begin{aligned}
&\lim_{T\to\infty}\frac{1}{T}\int_0^T\left(\frac{1}{2}+\frac{1}{2}\cos\left(\frac{2\pi}{\lambda}\left(x-a\sin(\omega t+\varphi)\right)\right)\right)dt = \\
&= \frac{1}{2}+\frac{1}{2}\cos\left(\frac{2\pi}{\lambda}(x-b)\right)\lim_{T\to\infty}\frac{1}{T}\int_0^T\cos\left(\frac{2\pi}{\lambda}a\sin(\omega t+\varphi)\right)dt + \\
&\quad +\frac{1}{2}\sin\left(\frac{2\pi}{\lambda}(x-b)\right)\lim_{T\to\infty}\frac{1}{T}\int_0^T\sin\left(\frac{2\pi}{\lambda}a\sin(\omega t+\varphi)\right)dt
\end{aligned} \tag{10}$$

Since

$$\lim_{T\to\infty}\frac{1}{T}\int_0^T\sin\left(\frac{2\pi}{\lambda}a\sin(\omega t+\varphi)\right)dt = 0 \tag{11}$$

previous equation will hold, if we multiply this component by a complex number i and replace $\sin(2\pi x/\lambda)$ with $\cos(2\pi x/\lambda)$, thus:

$$\begin{aligned}
\bar{F}_1(x) &= \lim_{T\to\infty}\frac{1}{T}\int_0^T\left(\frac{1}{2}+\frac{1}{2}\cos\left(\frac{2\pi}{\lambda}\left(x-a\sin(\omega t+\varphi)\right)\right)\right)dt = \\
&= \frac{1}{2}+\frac{1}{2}\cos\left(\frac{2\pi}{\lambda}x\right)\lim_{T\to\infty}\frac{1}{T}\int_0^T\cos\left(\frac{2\pi}{\lambda}a\sin(\omega t+\varphi)\right)dt+ \\
&+i\cdot\frac{1}{2}\cos\left(\frac{2\pi}{\lambda}x\right)\lim_{T\to\infty}\frac{1}{T}\int_0^T\sin\left(\frac{2\pi}{\lambda}a\sin(\omega t+\varphi)\right)dt = \\
&= \frac{1}{2}+\frac{1}{2}\cos\left(\frac{2\pi}{\lambda}x\right)\lim_{T\to\infty}\frac{1}{T}\dots \\
&\dots\int\cos\left(\frac{2\pi}{\lambda}a\sin(\omega t+\varphi)+i\cdot\sin\left(\frac{2\pi}{\lambda}a\sin(\omega t+\varphi)\right)\right)dt = \\
&= \frac{1}{2}+\frac{1}{2}\cos\left(\frac{2\pi}{\lambda}x\right)\lim_{T\to\infty}\frac{1}{T}\int_0^T\exp\left[\frac{2\pi}{\lambda}a\sin(\omega t+\varphi)\right]dt = \\
&= \frac{1}{2}+\frac{1}{2}\cos\left(\frac{2\pi}{\lambda}x\right)J_0\left(\frac{2\pi}{\lambda}a\right)
\end{aligned} \tag{12}$$

where T is the exposure time; J_0 is the zeroth order Bessel function of the first kind.

$$J_0(x) = \lim_{T\to\infty}\frac{1}{T}\int_0^T\exp\left[\frac{2\pi}{\lambda}x\sin(\omega t+\varphi)\right]dt \tag{13}$$

In case, a deflection from the state of equilibrium function is

$$u(x,t) = u(t) = a\sin(\omega t+\varphi)+b \tag{14}$$

where ω is the cyclic frequency; φ is the phase and a is the amplitude of the oscillation, b is a constant, the time-averaged gray level value will be:

$$\begin{aligned}
&\lim_{T\to\infty}\frac{1}{T}\int_0^T\left(\frac{1}{2}+\frac{1}{2}\cos\left(\frac{2\pi}{\lambda}\left(x-a\sin(\omega t+\varphi)\right)-b\right)\right)dt = \\
&= \frac{1}{2}+\frac{1}{2}\cos\left(\frac{2\pi}{\lambda}x\right)\lim_{T\to\infty}\frac{1}{T}\int_0^T\cos\left(\frac{2\pi}{\lambda}a\sin(\omega t+\varphi)\right)dt+ \\
&+\frac{1}{2}\sin\left(\frac{2\pi}{\lambda}x\right)\lim_{T\to\infty}\frac{1}{T}\int_0^T\sin\left(\frac{2\pi}{\lambda}a\sin(\omega t+\varphi)\right)dt
\end{aligned} \tag{15}$$

Derivation is similar to Eq. (12) and thus:

$$\bar{F}_2(x) = \frac{1}{2}+\frac{1}{2}\cos\left(\frac{2\pi}{\lambda}(x-b)\right)J_0\left(\frac{2\pi}{\lambda}a\right) \tag{16}$$

The original moiré grating is mapped into a time-averaged fringe ($\bar{F}_1(x) = 0.5$) when J_0 becomes equal to zero:

$$J_0\left(\frac{2\pi}{\lambda}a\right) = 0 \tag{17}$$

An envelope function which shows gray level changes in original image is

$$\frac{1}{2} \pm \frac{1}{2}J_0\left(\frac{2\pi}{\lambda}a\right) \tag{18}$$

In other words, the explicit relationship between the pitch of the moiré grating λ, the amplitude of harmonic oscillations a and the consecutive number of the time-averaged moiré fringe k reads:

$$\frac{2\pi}{\lambda}a_k = r_k;\ k = 1, 2, \ldots \tag{19}$$

where r_k is the k-th root of J_0; a_k is the discrete value of the amplitude which results in the k-th time-averaged fringe in the time-averaged image.

A pattern of time-averaged fringes is shown in Figure 1.4. Static moiré grating comprises opaque and transparent lines with the interval $0 \leq y \leq 5$ and the pitch of the grating $\lambda = 0.2$. Time-averaged fringes forms as amplitude increases and are modulated by the zero-order Bessel function of the first kind Eq. (12) (Ragulskis and Aleksa, 2009).

A computational demonstration of time-averaged fringe formation can be performed by constructing numerical time-averaged images, where the envelope function is changed by:

$$E_m(s) = \begin{cases} \frac{1}{m}\sum_{i=1}^{m}\left(\cos^2\left(\frac{\pi}{\lambda}\sin\left(\frac{2\pi}{m}\right)(i-1)/a\right)\right) \\ \frac{1}{m}\sum_{i=1}^{m}\left(\sin^2\left(\frac{\pi}{\lambda}\sin\left(\frac{2\pi}{m}\right)(i-1)/a\right)\right) \end{cases} \tag{20}$$

where m is number of discrete frames in one period of oscillations.

1.2. Holographic methods for identification of object surface deformations

Interferometry is an optical experimental technique for analysis of profiles of surfaces, motion, detection of deflections, structural vibrations of microsystems - where the amplitudes of those vibrations are in the range of nanometers to a few micrometers (Krishna Mohan et al., 2009; Kujawinska, 2002; Salbut et al., 2004; L. Yang et al., 2009). Various applications of this experimental method are being developed. Analysis of viscous and material damping in microstructures by means of interferometric microscopy (De Pasquale, 2013), interferometric readout of multiple cantilever sensors in liquid samples (Koev et al., 2010), an interferometric study of reliability of microcantilevers (Krupa et al., 2011), are typical examples of applications of interferometry in microsystems analysis.

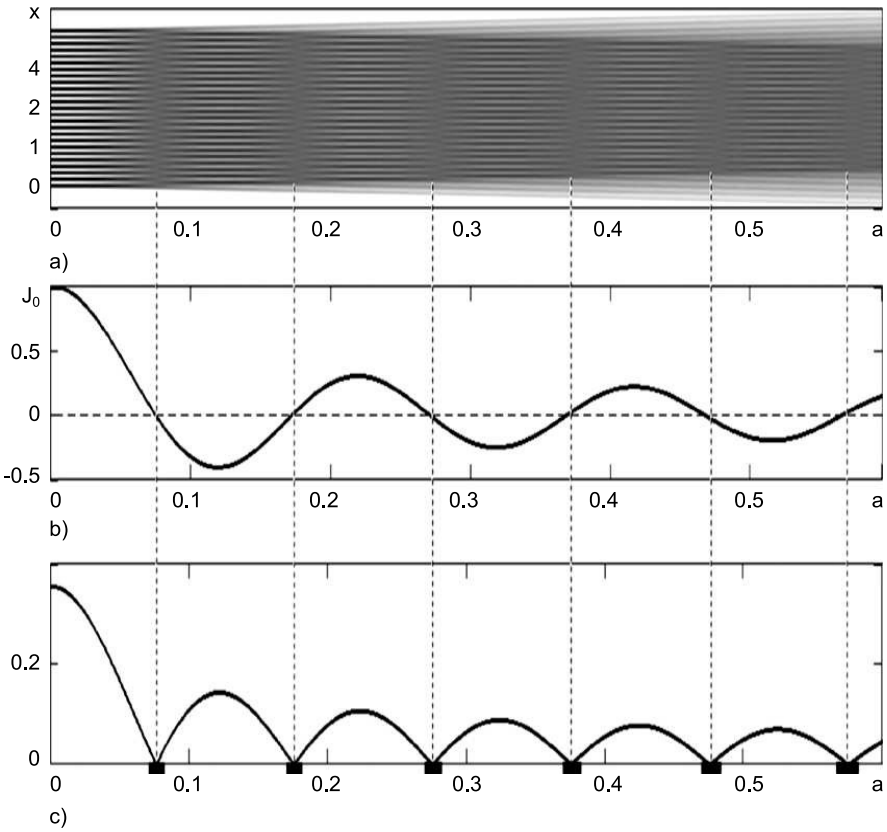

Figure 1.4: A pattern of time-averaged fringes at $\lambda = 0.2$ and $a(x) = x$. The grayscale image of the time-averaged fringe pattern is shown in a) and zero-order Bessel function of the first kind in b), and the standard deviation of the grayscale level in the time-averaged image in c). Centers of time-averaged fringes and roots of Bessel function are connected by dashed lines (Petrauskiene, Aleksa, et al., 2012).

Holographic interferometry is a powerful optical method for mapping changes in the shape of three-dimensional objects with high accuracy. Digital holography is used for nondestructive testing, strain analysis and analysis of vibrations in microsystems (Hariharan, 2007). An overview of a large variety of its applications for MEMS characterization, residual stress measurement, design and evaluation, and device testing and inspection is given in (Asundi, 2011). Digital holography and speckle interferometry are also widely used for the quality inspection and the assessment of the reliability of microsystems. These optical techniques are employed for the measurement of displacements, deformations induced by mechanical, thermal, or electrostatic loads (Pedrini et al., 2009), (Seebacher et al., 2001).

Time averaged holography is an experimental method for quantitative registration of surface oscillations that has been widely applied for the investigation of microsystems. The application of this method has been employed in measuring dynamics

of micro-metrology (Singh, Hedge, et al., 2006), dynamic characterization of MEMS diaphragm (Singh, Miao, et al., 2007), measurement of static and vibrating microsystems (Paul Kumar et al., 2011).

One of the assumptions made when applying time-averaged holography method is that oscillations are harmonic which might not be the case in real life applications of microsystems. It is well known that even a periodic excitation of the non-linear system may result in unpredictable, chaotic behavior (system behaviour, when the deterministic nature of the system does not make it predictable, is known as deterministic chaos, or simply chaos). Nonlinear and chaotic effects in microsystems are widely investigated in (W.-M. Zhang et al., 2011), (Siewe et al., 2011), (Haghighi et al., 2010), (Lin et al., 2006). Nonlinear dynamics and chaotic behavior of electrostatically actuated MEMS resonators subjected to random disturbance are investigated analytically and numerically in (W.-M. Zhang et al., 2011).

Computation and plotting of patterns of time-averaged holographic fringes in virtual numerical environments involves such tasks as modeling of the optical measurement setup, geometrical and physical characteristics of the investigated structures, and the dynamic response of analyzed microsystems (Ragulskis, Palevicius, et al., 2003). Holographic interferometry, being a non-destructive whole field technique, capable of registering oscillations of micro-components, cannot be exploited in a straightforward manner (Ostasevicius et al., 2005). There exist numerous numerical techniques for interpretation of patterns of fringes in the registered holograms of different oscillating objects and surfaces. Unfortunately, sometimes straightforward application of these motion reconstruction methods (for example ordinary fringe counting technique, and others) do not produce acceptable and interpretable results.

1.2.1. Double-exposure holography

Double-exposure holography uses two states of the object that are recorded on the same photo plate (Vest, 1979). In this case, hologram carries two complete and separate holograms. A wave in the plane of the hologram dispersed by any object is defined as

$$U_1(x,y) = A(x,y)\, e^{-i\phi_1(x,y)} \tag{21}$$

and wave in the plane of the hologram dispersed by any object that was under stress or load is defined as

$$U_2(x,y) = A(x,y)\, e^{-i\phi_2(x,y)} \tag{22}$$

where $A(x,y)$ is the amplitude distributions from the object, $\phi_1(x,y)$ and $\phi_2(x,y)$=$\phi_1(x,y) + \Delta\phi(x,y)$ are the initial phase and phase after deformations in object respectively. $U_2(x,y)$ changes because of small deformations in the object. The irradiance distribution of the object multiplied by a phase term created by the reconstructed wave behind the hologram can be expressed by.

$$I(x,y) = 2A^2(x,y)\left(1 + \cos\left[\Delta\phi(x,y)\right]\right). \tag{23}$$

The bright fringes are the places where the phase difference $\Delta\phi(x,y)$ is the even multiple of π, the dark fringes show the places where the phase difference $\Delta\phi(x,y)$ is the odd multiple of π. This method is very useful for such quantities as deformation and displacements though it is hard or sometimes even impossible to use it in real time applications where frequencies of oscillations are high.

1.2.2. Time-average holography

The basic principle of the formation of time-averaged holographic interference fringes can be illustrated by the harmonically oscillating cantilever example (Figure 1.5). Lets assume that the harmonic vibration of the beam is defined as

$$Z(x)\sin\omega t \tag{24}$$

where t is time; x is the longitudinal coordinate of the beam; $Z(x)$ is the transverse amplitude of oscillations of the one-dimensional beam at coordinate x; ω is the frequency of harmonic oscillations. Then the characteristic function defining the complex amplitude of the laser beam M_T in the plane of the hologram takes the form (Vest, 1979):

$$M_T = \lim_{T\to\infty}\frac{1}{T}\int_0^T \exp\left(i\left(\frac{4\pi}{\lambda}\right)Z(x)\sin\omega t\right)dt = J_0\left(\left(\frac{4\pi}{\lambda}\right)Z(x)\right) \tag{25}$$

where T is the exposure time of the hologram, ($T \gg 1/\omega$); λ is the laser wavelength; and J_0 is the zero-order Bessel function of the first kind. Then, the resulting intensity I of the point (x,y) on the hologram is

$$I(x,y) = a^2(x,y)\,|M_T|^2 \tag{26}$$

where $a(x,y)$ is the distribution of the amplitude of the incident laser beam. A schematic diagram of a cantilever oscillating according to the first eigenform is presented in Figure 1.5 a); the time-averaged pattern of holographic interference fringes is illustrated in Figure 1.5 b). Note that the decay of gray-scale intensity is rather fast at increasing amplitudes of oscillation. Better visualization of higher order time-averaged fringes requires contrast enhancement of the time-averaged image. As a limited number of intensity levels is used for the digital representation of images a sigmoid mapping function can be used to distort the intensity scale for better visualization of the results of calculations:

$$F(I) = \frac{\tanh(kI)}{\tanh(k)} \tag{27}$$

where parameter k characterizes the level of distortion, $0 < k < \infty$. Figure 1.6 illustrates the decay of gray-scale intensity without (the solid line) and with intensity mapping at $k = 2$ (the dashed line). The contrast-enhanced time-averaged pattern of holographic fringes at $k = 4$ ($k = 8$) is illustrated in Figure 1.5 c). The identification of fringes centerlines and employment of fringe counting techniques results

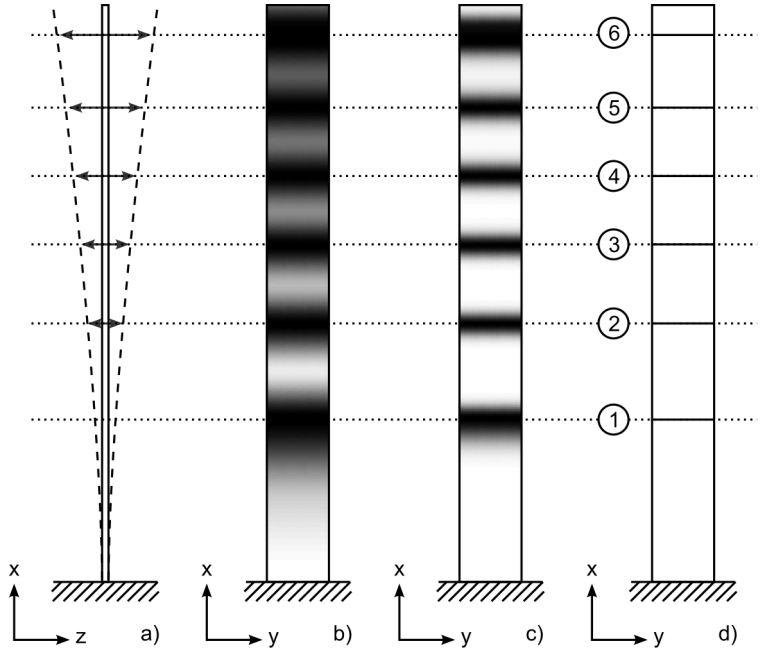

Figure 1.5: A schematic diagram illustrating the formation of time-averaged holographic fringes: the one-dimensional structure oscillating according to its first eigenform is shown in part a); corresponding gray-scale image in the holographic plane is represented in part b); the contrast enhanced time-averaged hologram is shown in part c); centerlines of time-averaged fringes and their consecutive numbers are represented in part d) (Vest, 1979).

into Figure 1.5 d). Note, that schematic illustration presented in Figure 1.5 is based on one-dimensional structure, therefore, finite width along the y-axis is used only for illustrative purposes.

The ability to enumerate time-averaged holographic fringes and to identify their centerlines results into the accurate reconstruction of the field of amplitudes of harmonic oscillations. Really, the amplitude of harmonic oscillations at point x_k corresponding to the centerline of the k-th time-averaged holographic fringe equals to:

$$Z\left(x_k\right) = \frac{\lambda r_k}{4\pi} \tag{28}$$

where $r_k;\ k = 1, 2, ...$ is the k-th root of the zero-order Bessel function of the first kind. Note that the uncertainty of such a reconstruction is directly related to the density of time-averaged fringes in the observation window. On the other hand, the density of time-averaged fringes is directly related to amplitudes of harmonic osculation and laser wavelength. It would be difficult to reconstruct the field of amplitudes from one time-averaged fringe. These constraints define limits of applicability of time-averaged laser holography in engineering applications. The laser wavelength is usually a fixed constant ($\lambda = 632.8[nm]$, for HeNe laser). Thus, one must pre-assess the results of the optical experiment.

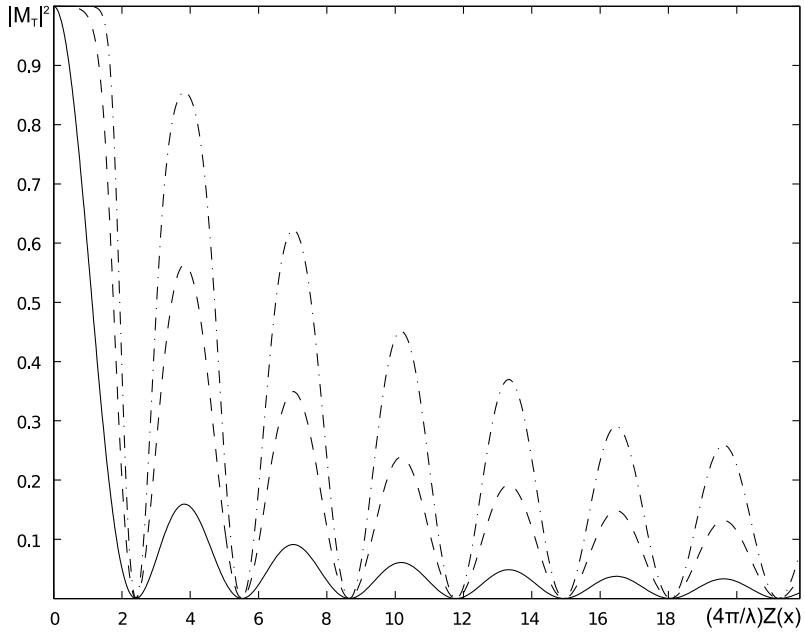

Figure 1.6: Contrast enhancement of time-averaged holographic fringes: the solid line represents the decay of intensity at increasing amplitude $Z(x)$; the dashed line shows mapped intensity levels at $k = 4$ (dashed line) and $k = 8$ (dash-dotted line).

All schematic diagrams in the figure are based on the assumption that the illumination and the observation directions are perpendicular to the plane of the beam in the state of equilibrium (in the par-axial model). In general case the distribution of intensity of the laser beam $a^2(x, y)$ reads:

$$a^2(x, y) = I_L(k_d(NL) + k_s(VR)^n) \tag{29}$$

where I_L is the intensity of the incident laser beam, k_d is the diffuse reflection coefficient, k_s is the specular reflection coefficient, n is a coefficient describing the smoothness of the surface, V is the direction of the viewer, R is the direction of the reflection. The pattern of time-averaged holographic fringes does not depend on the static deformations of the structure, nor from the distance between the structure and the hologram.

1.3. Computer generated holography

Computer Generated Holography (CGH) is the digital method which is used to generate holographic interference patterns. A CGH is different from an optical hologram in a way that there is no need to use real objects in the recording stage. Various computational algorithms are used to design a CGH of a non-existent, synthetic, or even a virtual object. The functionality of a DOE can be optimized mathematically rather than experimentally (Turunen, 1997). CGHs are applied in the fabrication of high spatial-frequency gratings (Suleski et al., 1999), direct laser beam writing (Schilling

et al., 2001), gray-tone lithography (Kley et al., 1999). An estimate of the phase hologram can be computed by using classical iterative Fourier transform algorithms such as Gerchberg-Saxton algorithm (Gerchberg et al., 1972) or Adaptive–Additive algorithm (Dufresne et al., 2001). The most popular method used to generate the computer generated holograms is Gerchberg-Saxton algorithm.

CGHs have been often exploited to implement various image encryption schemes. One of the examples is the method of optical image encryption with a binary CGH and pixel-scrambling technology (Y.-Y. Wang et al., 2007). The orders of the pixel scrambling as, well as the encrypted image, are used as the keys to decrypt the original image in this method. The other method allows optical color image encryption based on computer generated hologram and chaos theory (J. Liu et al., 2013). The tricolor separated images of the secret image are encoded with three random phase arrays constructed by a chaotic sequence of the deterministic non-linear system in this method. Then Burch's encoding method using the modified off-axis reference beam has been adopted to fabricate the CGH as the encryption image.

Optical multiple-image authentication based on modified Gerchberg-Saxton algorithm with random sampling is proposed in (W. Chen and X. Chen, 2014). It is demonstrated that such optical setup is not significantly affected by cross-talk terms and that the quality of recovered images is applicable for optical cryptography applications. A phase-modulated optical system with sparse representation for information encoding and authentication is developed in (W. Chen, X. Chen, et al., 2013). The optical cryptosystem is developed with cascaded phase-only masks, and the plaintext is encoded into the cascaded phase-only masks based on an iterative phase retrieval algorithm during the encryption. It is shown that the optical authentication operation with sparsity strategy can provide an additional security layer for the optical security system.

1.3.1. Fourier transform

Fourier transform is one of the most commonly used techniques in signal processing, and it has been employed in various other fields. It is also very useful in many areas of optics and imaging systems and is usually employed when creating DOE elements as it transforms a periodic function of space to a periodic function of time to generate descriptions of diffraction patterns and further imaging processes (Steward, 2004). A 2D Fourier transform is mathematically defined as follows:

$$F(u,v) = \int\int_{-\infty}^{\infty} f(x,y) \exp\left[-2\pi j\left(ux+uy\right)\right] dxdy \tag{30}$$

where u and v are spatial frequencies in x and y directions, respectively, and $F(u,v)$ is a 2D spectrum of $f(x,y)$. The inverse Fourier transform is defined as follows:

$$f(x,y) = \int\int_{-\infty}^{\infty} F(u,v) \exp\left[-2\pi j\left(ux+uy\right)\right] dudv \tag{31}$$

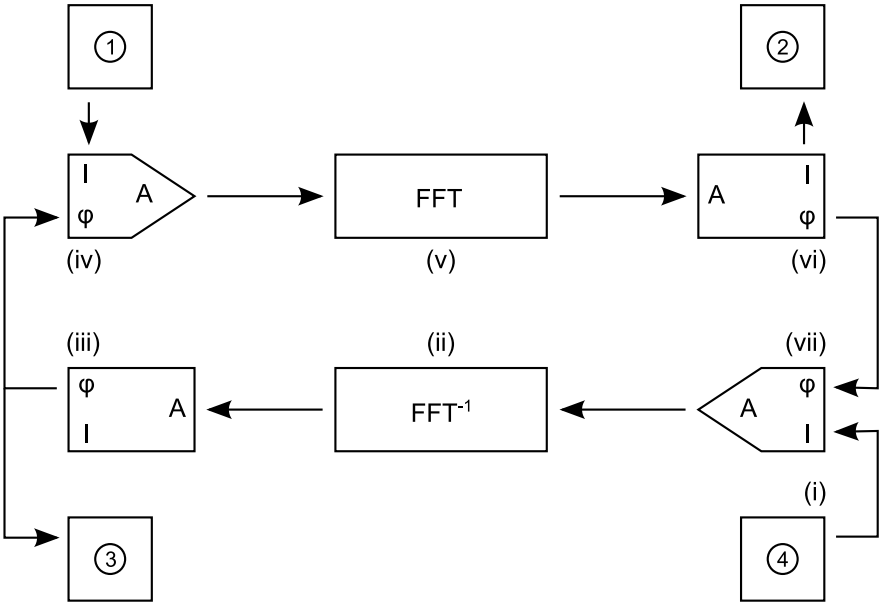

Figure 1.7: A schematic block illustration of Gerchberg-Saxton algorithm. Source intensity is marked as (1), approximation to target intensity as (2), phase mask as (3), and target intensity as (4).

For discrete data, the discrete Fourier transform is used, and it is the primary tool of digital signal processing. The DFT transforms time or space-based data into frequency-based data. The 2D discrete transform is defined as follows:

$$F(u,v) = \frac{1}{NM} \sum_{x=0}^{N-1} \sum_{y=0}^{M-1} f(x,y) \exp\left[-2\pi j \left(\frac{xu}{M} + \frac{yv}{N}\right)\right] dxdy \qquad (32)$$

where u and v are the discrete spacial frequencies, M and N are the number of samples in x and y directions in spacial and frequency domains, $F(u,v)$ is the 2D discrete spectrum of $f(x,y)$. The inverse of 2D discrete transform is defined as follows:

$$f(x,y) = \sum_{u=0}^{N-1} \sum_{v=0}^{M-1} F(u,v) \exp\left[2\pi j \left(\frac{xu}{M} + \frac{yv}{N}\right)\right] dxdy \qquad (33)$$

A direct calculation of N-point DFT requires N^2 complex multiplications and $N(N-1)$ complex additions (Zhou et al., 2015). To reduce the computation speed, various FFT (Fast Fourier Transform) algorithms has been developed to efficiently compute the discrete Fourier transform and its inverse (R. Al Na'mneh et al., 2007; Nibouche et al., 2010; R. A. Al Na'mneh et al., 2013).

1.3.2. Gerchberg-Saxton algorithm

Gerchberg-Saxton algorithm is used for the estimation of the phase field in (Gerchberg et al., 1972). A block diagram is presented in Figure 1.7. The intensity dis-

tribution of the unshaped light beam in the hologram plane is defined as I_H and the target intensity distribution in the Fourier plane as I_T. The light fields are defined by 2D arrays of complex numbers u_n and $\tilde{u}_n$ in the hologram plane and in the Fourier plane respectively. In the beginning, a random number generator is used to generate a phase distribution φ_0^H from a stochastic variable distributed uniformly in the interval $[-\pi, \pi]$. The algorithm (Gerchberg et al., 1972) steps are given as follows:

(i) Calculate initial field in the hologram plane as follows:

$$u_n^T = A\left(I_H\right) \exp\left(i\varphi_{n-1}^H\right), \text{ where } A(z) = \sqrt{x \cdot x + y \cdot y} \tag{34}$$

(ii) This field is propagated from the image-plane to the object-plane. The amplitude information is discarded leaving only the phase information (for the phase mask).

$$\varphi_n^T = P\left(\text{FFT}\left(u_n^H\right)\right), \text{ where } P(z) = \arctan\left(\frac{y}{x}\right) \tag{35}$$

(iii) The amplitude and phase of the illumination field are added to the phase information in order to obtain the resulting object field.

$$u_n^T = A\left(I_T\right) \exp\left(i\varphi_n^T\right) \tag{36}$$

(iv) This field is propagated from the object plane to the image plane.

$$\varphi_n^H = P\left(\text{FFT}^{-1}\left(u_n^T\right)\right) \tag{37}$$

(v) The resulting reconstructed image (the square of the field amplitude) is compared with the expected one. The decision to terminate the process (or continue to iterate) is made by computing the correlation between both images.

$$I_n = \left|u_n^T\right|^2 \tag{38}$$

(vi) The phase from the reconstructed image is combined with the field amplitude obtained from the expected irradiance. The process is repeated from step (i).

1.4. Methods for processing interference fringes

Methods, based upon interference patterns, require tools to analyze interference fringes. Standard methods are carrier Fourier transform method, phase shifting technique, and fringe centering technique. Fourier transform is an automatic method that is suitable for the calculation of full-field displacements. Fourier transform method has practical limitations compared to its theoretical model as it lacks the capability of handling discontinuities that are common in experimental interferograms due to

noise, lighting conditions and other. Phase shifting technique uses multiple records of interference fringe patterns where phase modulation is shifted. This allows to retrieve a wrapped phase map and reconstruct a 3D profile of an object. Fringe centering technique is based on identifying fringe centerlines and enumerating them. Many algorithms exist for the identification of centerlines and enumeration of interference fringes, though most of them has limitations.

1.4.1. Mid-point detection method

The method is based on the algorithm proposed in (Parthiban et al., 1989) and later improved in (Anand, 2003). It uses vertical and horizontal scan lines to determine mid-points of each dark and bright fringe. The detailed description of this method is given in (Anand, 2003). It is based on global thresholding and row-column-wise scanning. This method can be universally applied to all types of interferograms where fringe centering is needed, such as film thickness measurement based on automatic fringe analysis proposed in (Abdelsalam et al., 2012), and others. The location of the mid-point of a fringe can be described by a simple formula:

$$m\left(l,s\right)=round\left(\frac{l-s}{2}\right) \tag{39}$$

where s is the number of column (row) where the zero level pixel is found in the current row (column) and l is the number of column (row) where the first white pixel is detected after a series of zeros. Row and column scans produce two matrices R and C with all locations of mid-points of fringes. Geometric superposition of matrices R and C results into the simultaneous scan matrix S that could be expressed as:

$$S=\sum_{i=1}^{m}\sum_{j=1}^{n}R\left(i,j\right)\oplus C\left(i,j\right) \tag{40}$$

where $\oplus$ is a logical "and" operation if centers of dark fringes are to be identified and is a logical "or" operation if centers of white fringes are to be found. The algorithm proposed in (Anand, 2003) automatically selects the type of the scan depending on the shape of the fringes to give the best trace of the fringes. The type of the scan is determined by scanning the interferogram row-wise and column-wise. Counting the number of times, the scan line crosses a dark or bright fringe allows to select a type of scan.

1.4.2. Phase shifting technique

Phase shifting technique has been often applied to moiré and holographic methods as a tool to identify interference fringes. A common setup where four fringe patterns are recorded is often used in the phase shifting method though lesser or larger number of interference patterns can be also used to improve the the quality of reconstructed image. However a larger number of fringe patterns increases the processing

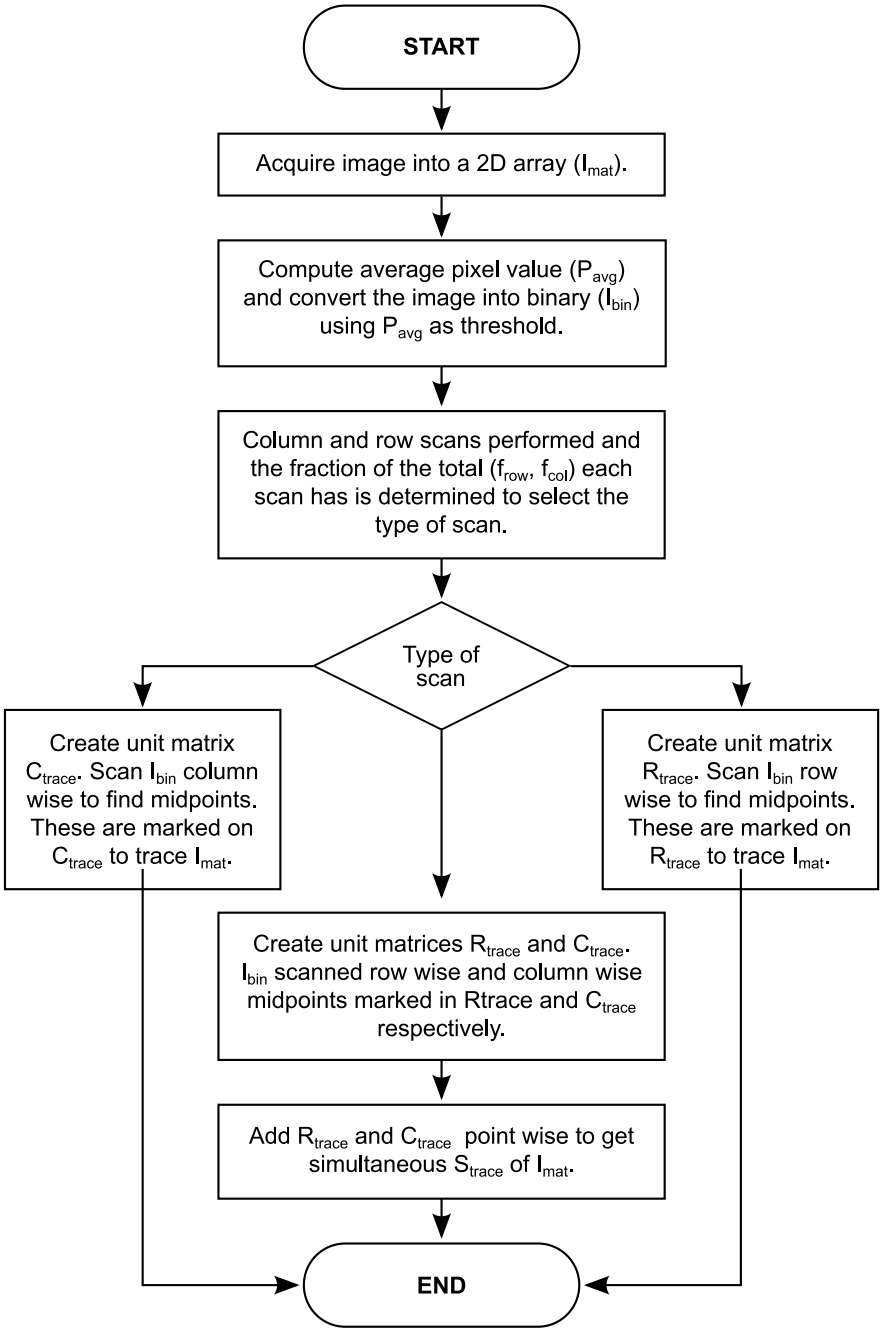

Figure 1.8: An algorithm of a method for tracing of interference fringes using average gray value and simultaneous row and column scan (Anand, 2003).

time. In case of shadow moiré, the common way to record different patterns is to change the distance between the master grid and the specimen. The intensity distribution of recorded interference fringes pattern is described as:

$$g\left(x,y\right)=a\left(x,y\right)+b\left(x,y\right)\cos\left(\varphi(x,y)\right) \tag{41}$$

where $a\left(x,y\right)$ is background illumination, $b\left(x,y\right)$ is amplitude modulation of fringes, $\varphi(x,y)$ is the phase modulation of fringes. Three unknown variables are present in this equation, where $\varphi(x,y)$ should be solved. Four patterns, each with a phase shift of $\pi/2$ are being recorded:

$$\begin{aligned} g_1\left(x,y\right)&=a\left(x,y\right)+b\left(x,y\right)\cos\left(\varphi(x,y)\right)\\ g_2\left(x,y\right)&=a\left(x,y\right)+b\left(x,y\right)\cos\left(\varphi(x,y)+\Delta\varphi_1\right)\\ g_3\left(x,y\right)&=a\left(x,y\right)+b\left(x,y\right)\cos\left(\varphi(x,y)+\Delta\varphi_2\right)\\ g_4\left(x,y\right)&=a\left(x,y\right)+b\left(x,y\right)\cos\left(\varphi(x,y)+\Delta\varphi_3\right) \end{aligned} \tag{42}$$

where $\Delta\varphi_1$, $\Delta\varphi_2$, $\Delta\varphi_3$ are phase differences applied to patterns of images equal to $\pi/2$, π, $3\pi/2$ respectively. A phase map can be acquired as follows:

$$\begin{aligned} \Psi\left(x,y\right)&=\tan^{-1}\left(\frac{g_4\left(x,y\right)-g_2\left(x,y\right)}{g_1\left(x,y\right)-g_3\left(x,y\right)}\right)=\\ &=\tan^{-1}\left(\frac{2b\left(x,y\right)\cos\left(\varphi(x,y)\right)}{2b\left(x,y\right)\sin\left(\varphi(x,y)\right)}\right)=\left[\varphi\left(x,y\right)\right]\mod\pi \end{aligned} \tag{43}$$

One should note that a phase field is not uniform and has discontinuities which have to be removed by adding grating pitch p at the boundaries of these discontinuities. This operation is called phase unwrapping and can be performed with methods such as (Guo et al., 2014) and (Y. Li et al., 2015). Recent applications of phase shifting technique includes but are not limited to 3D profile reconstruction of biological sample by in-line image-plane phase-shifting digital microscopic holography (Lu et al., 2012), usage of quasi common path phase-shifting interferometer for measurement of natural convection fields (Shoji et al., 2012), employment of phase shifting technique for Compressive optical image encryption with two-step-only quadrature (J. Li et al., 2015). Various methods and improvements has been made to this technique in recent years such as adaptation of Monte Carlo simulation method to characterize the probabilistic properties of the systematic and random sensitivities in non-linear two-stage phase-shifting algorithms (Miranda et al., 2011), creation of phase-shifting technique for 3-D measurement using spectral-transform (Huo et al., 2013), composite phase-shifting algorithm for absolute phase measurement (S. Zhang, 2012), and others.

This method has an advantage against centerline detection methods as it is more reliable and provides more accurate results. Nevertheless, it is clear from the above equations, that phase shifting technique is not applicable or complicated in cases, where we need to investigate an object that is changing in time and where different states

of an object should be recorded. An example would be a warpage of printed circuit boards, where the 3D profile would be reconstructed with different temperatures. Thus, a centerline detection method should be used in this case.

1.5. Visual cryptography

Visual cryptography is a cryptographic technique that encrypts visual information (pictures, text, etc.). In case of visual cryptography, the decryption is a mechanical operation that can be performed without an aid of the computer. One of the first and best-known visual cryptography techniques has been proposed by Moni Naor and Adi Shamir (Naor et al., 1995). In this scheme, an image was broken into n shares in such way, that only having all n shares would reveal the secret image, and $n - 1$ shares would not leak any information about the secret image. The shares were printed on the transparent material and overlaying the shares revealed the secret image. A demonstration of this method is shown in Figure 1.9. It is clear that shares shown in parts a) and b) does not leak any information about the original image in part c). A decrypted image is visible in part d) where parts a) and b) have been superimposed.

Various other techniques have been developed since the proposal of a method by Moni Naor and Adi Shamir. A halftone visual cryptography scheme was proposed that uses minimum auxiliary black pixels and provides uniform image quality (Yan et al., 2015b). This and similar methods decreases suspicion of secret image encryption since meaningful information is visible in the cover image. It allows to hide the fact that information has been encoded in the first place. Similar techniques and approaches are also presented in (Yan et al., 2015a; Ou et al., 2015; Chiu et al., 2015).

Most visual cryptography techniques concentrate on binary images. Nevertheless, methods or schemes for processing grayscale and color images are being developed. A technique developed by (Hou, 2003) proposes three methods for visual cryptography of grayscale and color images based on binary visual cryptography, the halftone technology, and the color decomposition method. In many CVCS techniques, larger pixel expansion is needed in order to produce more colors, but it has a negative impact on size. Thus a technique of additive color mixing in a probabilistic way and a new color visual cryptography scheme with the fixed pixel expansion was proposed in (C.-N. Yang et al., 2008). Though this method reduces contrast quality of decoded secret image. Another method that uses color transfer scheme and incorporates it into the (k, n) visual cryptography model is proposed in (Luo et al., 2014). During encoding state, a color image is encrypted into n binary share images. When k or more than k shares are collected, a high quality colorful variation of the secret image is reconstructed.

1.5.1. Dynamic visual cryptography

An alternative approach to visual cryptography is proposed in(Ragulskis and Aleksa, 2009). Instead of using several separate shares, authors of (Ragulskis and Aleksa, 2009), did employ stochastic moiré gratings for hiding a secret image in a sin-

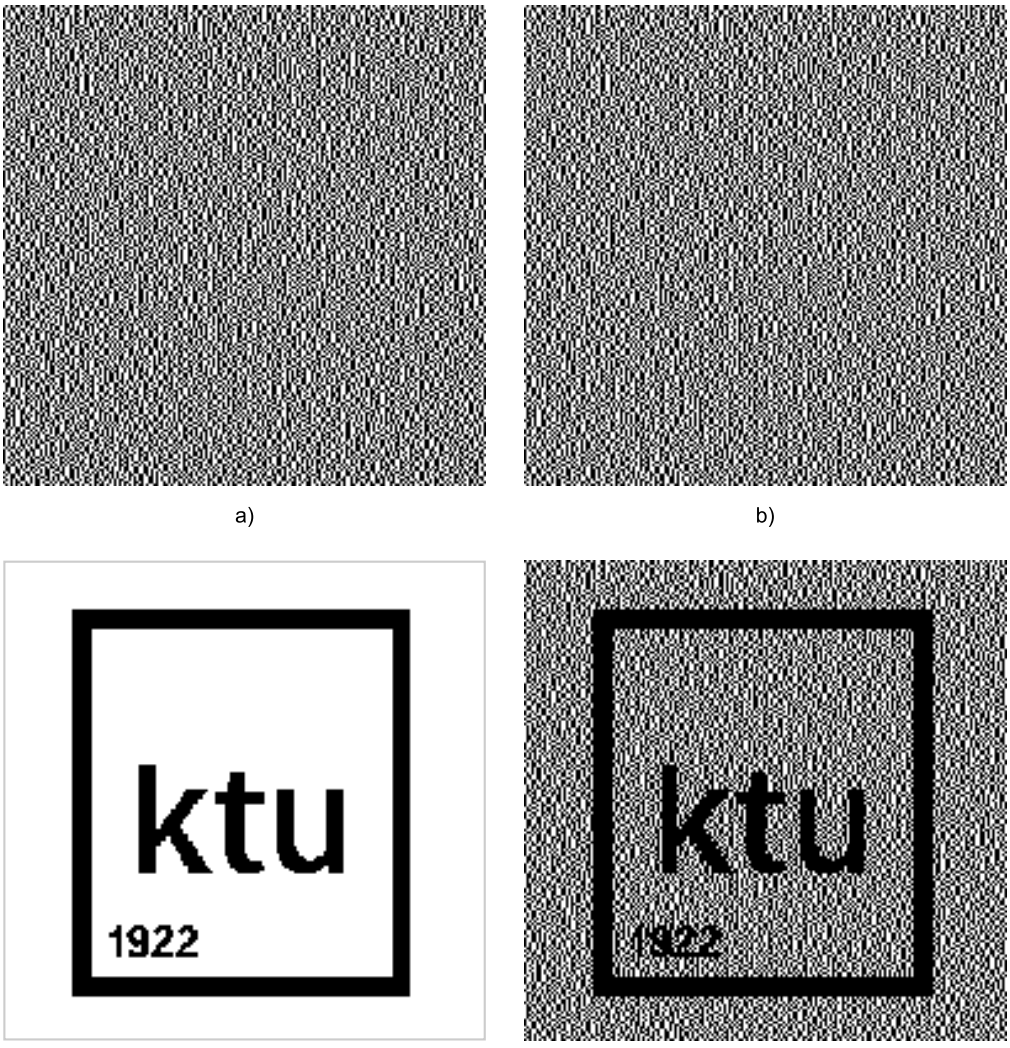

a) b)

c) d)

Figure 1.9: A demonstration of visual cryptography method proposed by Moni Naor and Adi Shamir. In this figure the two shares needed to decrypt secret information are shown in a) and b), original secret image is shown in c), the result of superimposed shares a) and b) is shown in d).

gle cover image. The secret image is leaked in a form of time-averaged moiré fringes if cover image is oscillated according to a predefined function determining the deflection from the state of equilibrium and time-averaged optical techniques are used to register the optical image. A secret image can be interpreted by a human visual system only when the original cover image is oscillated in a predefined direction. This visual cryptography technique requires only one image; the encoded image looks completely random in the state of the static equilibrium. The secret image is visualized only at strictly defined parameters of oscillation.

The principle of the encoding of the secret image in the cover image is based on two chaotic scrambling algorithms. The first one – initial moiré grating stochastic phase algorithm is applied to all columns of the cover image. Secondly, moiré grating phase regularization algorithm is used eliminate phase jumps at the boundaries of the background and the secret image. Though such encoding is not cryptographically secure, the static cover image cannot be interpreted by a naked eye until the cover image is oscillated according to a predefined law of motion. Image splitting techniques are also proposed in (Ragulskis and Aleksa, 2009), what ensures the cryptographical security – but then the separate shares should be first stacked together, and then resulting image must be oscillated according to the same predefined law of motion.

Such dynamic visual cryptography scheme enables encoding of dichotomous digital images only. Moreover, the oscillation of the cover image predefines the minimum size of an interpretable optical primitive of the secret image. In other words, deformation of time-averaged moiré fringes predetermines the resolution of the secret image.

It appears that dynamic visual cryptography has a strong potential for applications in mechanical engineering. Particularly, dynamic visual cryptography can be effectively used for optical monitoring of harmonic and even chaotic oscillations. The encoded cover image is fixed on the head of a vibration shaker system in (Petrauskiene, Aleksa, et al., 2012). A human operator can detect the parameters of the vibration processes by simply taking a look at vibrating cover image – something is wrong with the system if the secret image cannot be interpreted by a naked eye. The sensitivity of such non-destructive non-contact time averaged moiré based optical method is predetermined by the pitch of the stochastic moiré grating used to encode the secret. In other words, one can preselect a required sensitivity that appears to be astonishingly high in the context of structural dynamics applications.

1.5.2. Chaotic visual cryptography

Similar approach based on optical time-averaged moiré gratings has been proposed for optical monitoring of chaotic oscillations (Petrauskiene, Palivonaite, et al., 2014). Mathematical relationships show that time-averaged moiré fringes do not form when moiré gratings are oscillated according to the chaotic law – the envelope function, in this case, is a decaying exponential function in contrast to zero-order Bessel function of the first kind in case of harmonic oscillations (Petrauskiene, Palivonaite, et al., 2014). However the optical contrast between the background and secret moiré

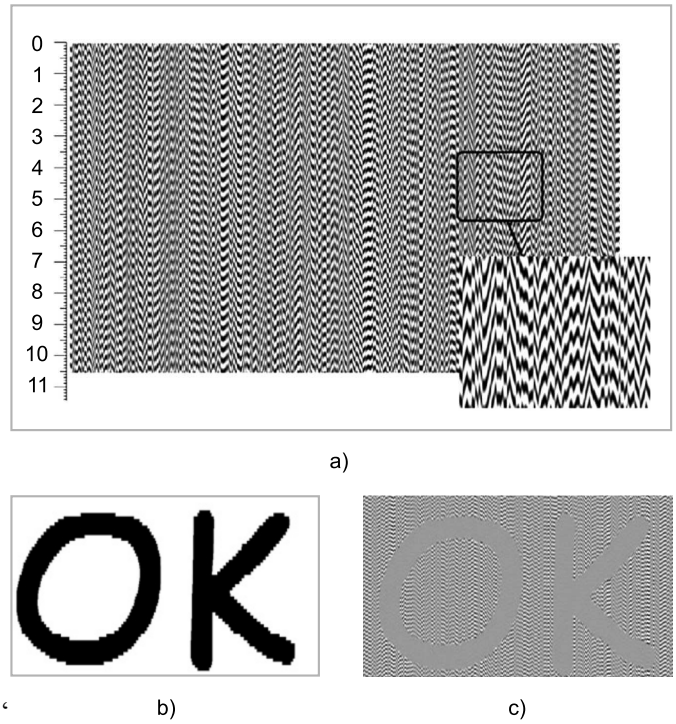

Figure 1.10: An example of the encrypted image (the structure of moiré grating is visible in the zoomed part) is shown in part a). The secret image is shown in part b). The decryption of the secret is shown in part c) (Petrauskiene, Aleksa, et al., 2012).

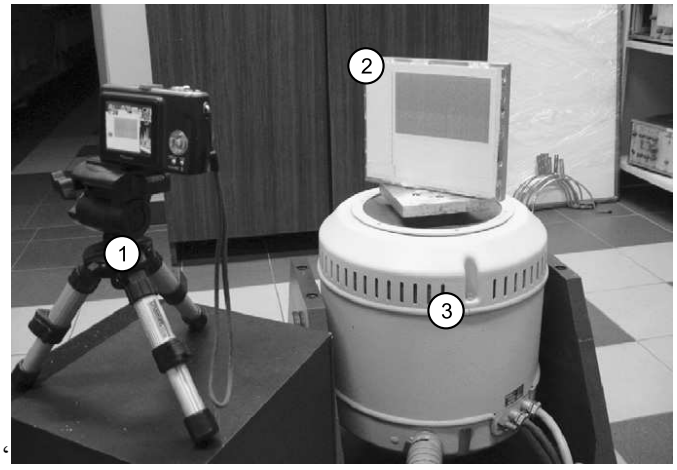

Figure 1.11: A photo of the experimental setup comprising: digital camera (1); the encoded image (2) fixed to a rigid structure, which is attached to the head a shaker table (3) (Petrauskiene, Aleksa, et al., 2012).

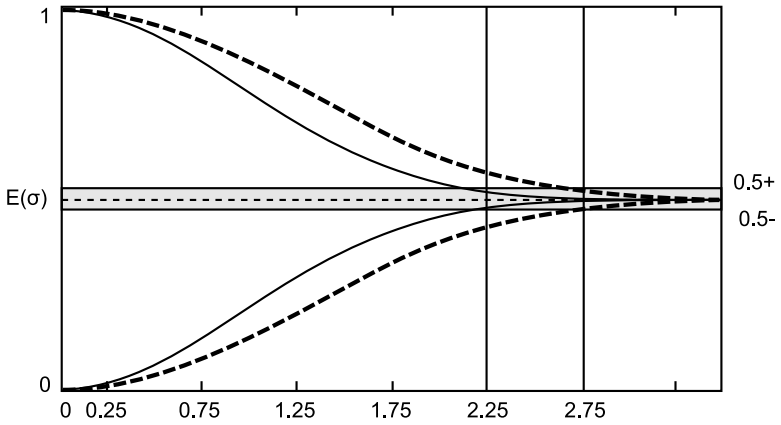

Figure 1.12: The schematic diagram demonstrating the experimental implementation of chaotic visual cryptography: the gray region shows where fully developed fringes are visible in the time-averaged image; solid curves and dashed curves illustrates the decay of the envelope function (with pitches λ_0 and λ_1 respectively; vertical lines illustrate a region of σ that can be used for chaotic visual cryptography (Petrauskiene, Palivonaite, et al., 2014).

gratings in the time-averaged mode can be efficiently exploited for chaotic vibrations too – a schematic diagram of such image hiding technique is illustrated in the Figure 1.12.

An expansion of periodic moiré grating into Fourier series is

$$F(x) = \frac{a_0}{2} + \sum_{k=1}^{+\infty} \left(a_k \cos\left(\frac{2\pi k}{\lambda} x\right) + b_k \sin\left(\frac{2\pi k}{\lambda} x\right) \right) \tag{44}$$

where λ is the pitch of grating. Lets denote $p_\xi(x)$ as the density function of $\xi(t)$. $\xi(t)$ is a function that describes time-dependent deflection from the state of equilibrium. In this case, the time-averaged image oscillated according to function $\xi(t)$ reads:

$$\bar{F}(x) = \frac{a_0}{2} + \sum_{k=1}^{+\infty} \left(a_k \cos\left(\frac{2\pi k}{\lambda} x\right) + b_k \sin\left(\frac{2\pi k}{\lambda} x\right) \right) P_\xi\left(\frac{2\pi k}{\lambda}\right) \tag{45}$$

where P_ξ is Fourier transformation of $p_\xi(x)$. Thus, the time-averaged image is blurred according to the function $p_\xi(x)$. The envelope function of the contrast decay of the time-averaged moiré grating, that is blurred by chaotic oscillation is

$$\begin{aligned} \bar{E}(\sigma) &= \frac{1}{2} \pm \frac{1}{2} \exp\left[-\frac{1}{2}\left(\frac{2\pi\sigma}{\lambda}\right)\right] \cdot \ldots \\ \ldots &\sum_{k=1}^{+\infty} \left(a_k \cos\left(\frac{2\pi k}{\lambda} x\right) + b_k \sin\left(\frac{2\pi k}{\lambda} x\right) \right) P_\xi\left(\frac{2\pi k}{\lambda}\right) \end{aligned} \tag{46}$$

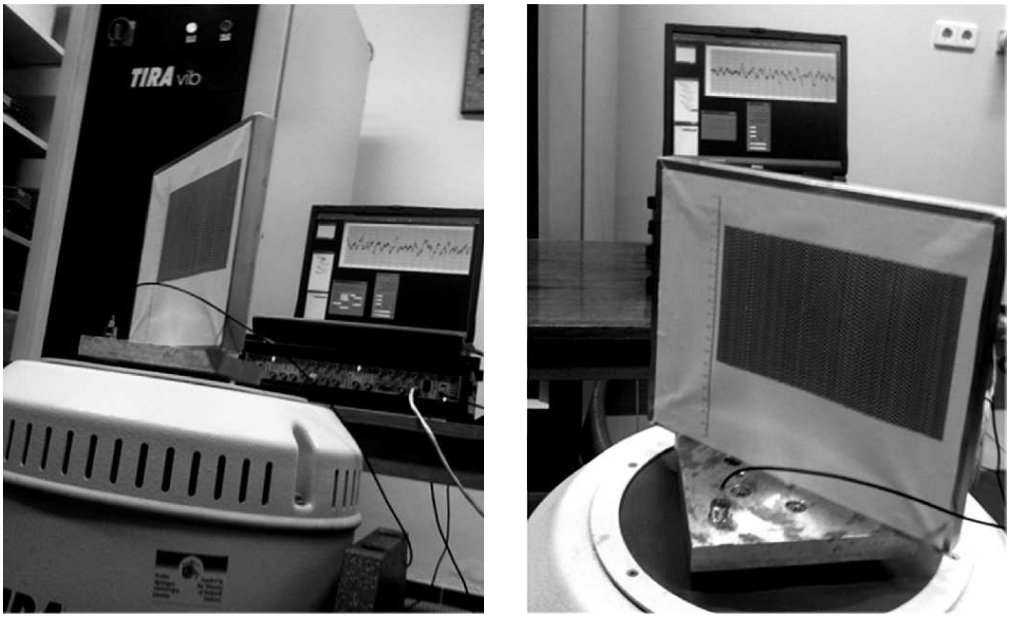

Figure 1.13: The general view of the experimental setup is shown in part a); a lightweight piezoelectric accelerometer is used to monitor the vibration of the shaker table (part b) (Petrauskiene, Palivonaite, et al., 2014).

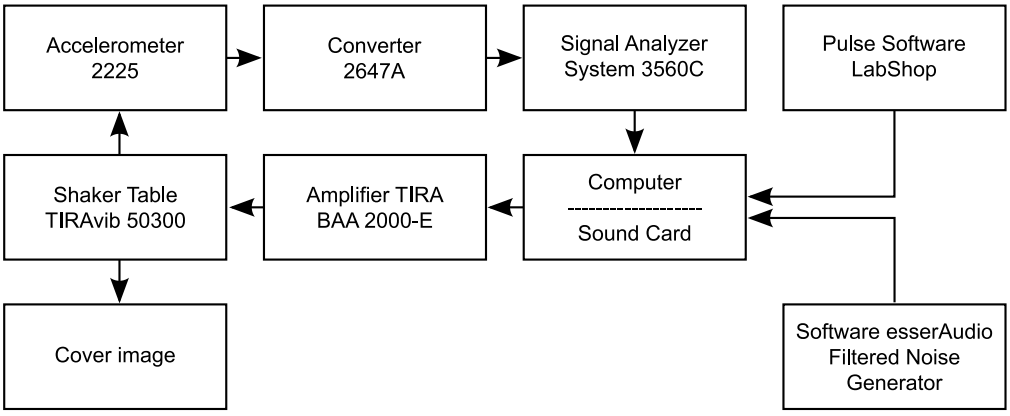

Figure 1.14: The schematic diagram of the experimental setup (Petrauskiene, Palivonaite, et al., 2014).

In this case no time-averaged fringes are formed by chaotic oscillations as moiré grating is blurred when σ is increased (Figure 1.12). The sharp image of the static moiré grating is produced when $\sigma = 0$ and the time-averaged image is blurred as σ tends to infinity.

Chaotic dynamic visual cryptography is effectively applied for optical experimental monitoring of chaotic oscillations (Petrauskiene, Palivonaite, et al., 2014). The encoded cover image is fixed on to the surface of vibration shaker performing chaotic vibrations (Figure 1.13).

The schematic diagram of the optical experimental setup is shown in Figure 1.14. In this setup amplifier (TIRA BAA 2000-E) is used to control the shaker table (TIRAvib 50300). Filtered noise generator software (Esser-Audio) is used to produce the white noise, to pass it through the low pass filter, and to send the signal to the amplifier. The cover image and the lightweight piezoelectric accelerometer (Endevco 2225, sensitivity $0.07655\ [pC/m/s^2]$) is mounted on the head of the shaker table. Charge to voltage converter (Type 2647A, amplification $1\ [mV/pC]$) is used to connect piezoelectric accelerometer to the pulse multi-analyzer system (Type 3560). The whole process is controlled by Bruel & Kjaer Pulse LabShop. In this setup, low-frequency chaotic oscillations are being generated, together with control the instantaneous waveform of the generated motion. It allows to set, monitor and control the variables of chaotic oscillations.

The proposed optical technique based on time-averaged moiré fringes and chaotic oscillations can be effectively used to asses chaotic processes by a naked eye.

1.6. Conclusions

The literature review shows that a reliable application of optical experimental techniques is important in MEMS analysis. Thus, analytical techniques for the interpretation of time-averaged holographic fringes produced by non-linear oscillations of microelectromechanical will be investigated in this thesis. Also, computational tools for the reliable identification of experimental optical images of complex, undeveloped interferometric fringes embedded in high background noise, that allows continuation and extrapolation of fringe centerlines, will be developed. Finally, the literature review suggests, that an experimental technique, based on the optical integration of computer generated holography, and dynamical visual cryptography could be developed that is used for MEMS investigation and monitoring.

2. APPLICATION OF TIME-AVERAGED HOLOGRAPHY FOR MEMS ANALYSIS

The interpretation of time-averaged fringes produced by harmonic oscillations allows validation dynamic displacements of MEMS components. However, it has been shown that MEMS resonators can perform nonlinear vibrations (Ghayesh et al., 2013; Bao et al., 2007; Jia et al., 2012). In this chapter, a finite element model of a fixed-fixed beam performing nonlinear oscillations is developed and integrated with optical time-averaged holography model. The simulations provide valuable insight into the motion of MEMS devices.

2.1. Fixed-fixed beam FEM model

A fixed-fixed beam model will be used for the computational experiment illustrating the formation of time-averaged holographic fringes when the beam performs complex transient oscillations. A schematic diagram of a typical MEMS device comprising a deformable fixed-fixed beam over a fixed ground electrode is shown in Figure 2.1. The potential difference is applied between the beam and the ground electrode that induces electrostatic charges. These two electrostatic charges creates electrostatic pressure normal to the surface of the conductor.

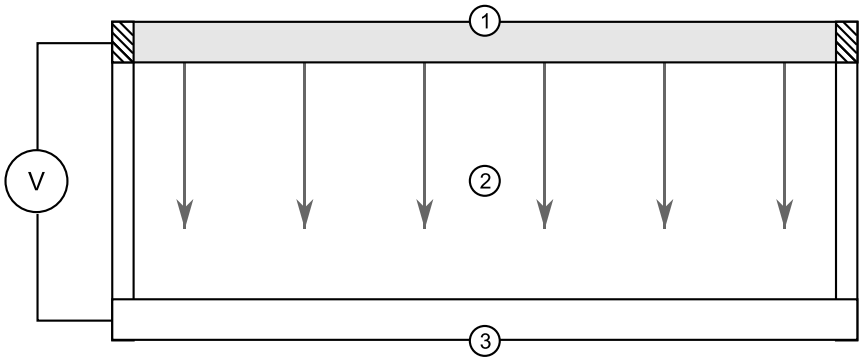

Figure 2.1: The schematic diagram of the MEMS device – a fixed–fixed beam with an applied voltage V over a ground plane. Fixed-fixed beam is shown in (1), electrostatic pressure in (2), ground electrode in (3).

Finite element method (FEM) is used for the simulation of the MEMS device. Time-dependent simulation is implemented in COMSOL Multiphysics package; figure 2.2 provides the geometry and meshing of the MEMS device.

A material used for the beam structure is Silicon with relative permittivity $\epsilon = 11.7$, density $\rho = 2329[kg/m^3]$, Young's modulus $E = 170e9[Pa]$, and Poisson's ratio $\nu = 0.28$. The silicon is assumed to be heavily doped, so that electric field penetration into the structure can be neglected. The beam resides in an air-filled chamber that is electrically insulated. The dimensions of the beam are: Length $300[\mu m]$; Depth $20[\mu m]$; and Height $1[\mu m]$. The model considers a layer of air $6[\mu m]$ thick above and

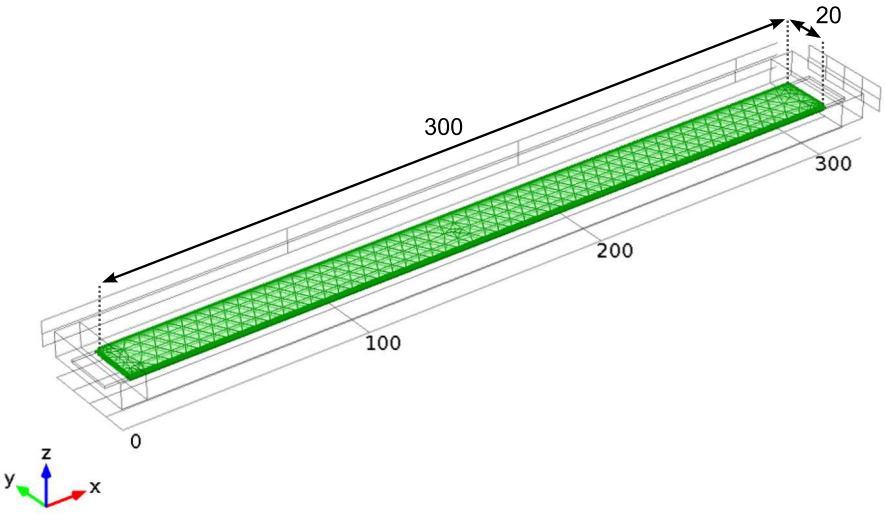

Figure 2.2: The geometry and FEM mesh of the fixed-fixed beam MEMS model

$10[\mu m]$ thick to the sides of the beam, and the air gap between the bottom of the beam and the grounded plane is initially set to $3[\mu m]$. An unstructured tetrahedral mesh is used for the fixed-fixed beam and its surroundings.

Electromechanics physics Comsol interface is used for computational simulation. It combines solid mechanics and electrostatics with a moving mesh to model the deformation of electrostatically actuated structures:

$$\rho \frac{\partial^2 u}{\partial t^2} - \nabla \cdot \sigma = Fv \tag{47}$$

$$\nabla \cdot D = \rho_v \tag{48}$$

here u denotes the displacement field; t is time; ρ is the material density; σ is the stress tensor; F is an external volume force; D is electric displacement or electric flux density; v is velocity and ρ_v is charge density in vacuum.

An electrostatic force caused by the potential difference between the two electrodes bends the beam toward the grounded plane beneath it. This model calculates the electric field in the surrounding air in order to compute the electrostatic force. As the beam bends, the geometry of the air gap changes continuously, resulting in a change in the electric field between the electrodes. The coupled physics is handled automatically by the Comsol electromechanics interface.

The electrostatic field in the air and in the beam is governed by Poisson's equation:

$$-\nabla \cdot (\varepsilon \nabla V) = 0 \tag{49}$$

where derivatives are taken with respect to the spatial coordinates. The force density that acts on the electrode of the beam results from Maxwell's stress tensor:

$$F_{es} = -\frac{1}{2} (E \cdot D) n + (n \cdot E) D \tag{50}$$

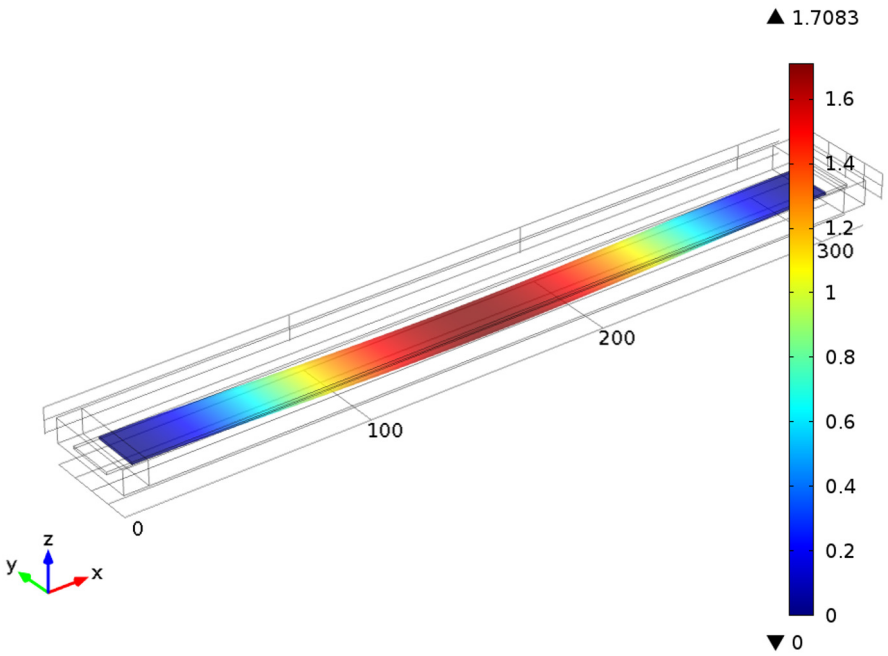

Figure 2.3: The shape of the fixed-fixed beam in the state of maximum deformation while performing periodic oscillations according to the first computational experiment.

where E and D are the electric field and electric displacement vectors, and n is the outward normal vector of the boundary. Note that this force is always oriented along the normal of the boundary.

A condition of the zero charge on the boundary is used, as this is the default boundary condition at exterior boundaries.

$$-n \cdot D = 0 \tag{51}$$

The initial values for electric potential and solid displacement field are:

$$u|_{t=0} = 0,\ V|_{t=0} = 0 \tag{52}$$

The fixed constraint condition that makes the geometric entity fixed (the displacements are zero in all directions) are applied to the boundaries of the beam. The ground boundary condition is applied to the bottom plain that gives zero potential on the boundary. The boundary condition is applied to fixed-fixed beam of an electric potential V_0.

$$V = V_0 \tag{53}$$

2.2. Computational results for a fixed-fixed beam

Computational simulation is performed for the model of the fixed-fixed beam (the model is described in details in Section 2.1) with three different electric potential

boundary conditions. In order to simplify the visualization of transient processes a single point is selected at the center of the beam (where the displacements are largest) and plot time signals and phase diagrams for all three different potential boundary conditions.

During the first computational experiment (i) a DC (direct current) bias of $V_{DC} = 40[V]$ is applied to the micro-device in order to obtain the system's response. The DC bias is applied using the standard Comsol smoothed step function which allows to increase the voltage incrementally from 0 to V_{DC} during the transient interval ranging from 0 to $6e-6$. After the transient interval the DC bias is set to a constant:

$$V = V_{DC} \tag{54}$$

The second computational experiment (ii) employs a DC bias on top of a sinusoidal AC voltage:

$$V = V_{DC} + V_{AC} \sin(2\pi f t) \tag{55}$$

where $V_{DC} = 38[V]$ and $V_{AC} = 2[V]$. Finally, a DC bias of $V_{DC} = 35[V]$ with AC voltage of $V_{AC} = 5[V]$ is applied in the last computational experiment (iii). The exposure time t used in all simulations is ranging form 0 to $1e-4$ with a time step of $2e-7[s]$.

The results of computational experiments are presented in Figure 2.4. It can be seen that the response of the system is periodic under the constant DC bias excitation. Note that these periodic oscillations are caused not by a harmonic excitation – the beam is deflected from the state of equilibrium during the short transient process and continues to oscillate because the damping is small (mass damping parameter $\alpha_{dM} = 418.9[1/s]$ and stiffness damping parameter $\beta = 8.29e-13[s]$).

The results of the second computational experiment are different compared to the periodic oscillation caused by the short DC transient in the first computational experiment. The harmonic AC component interacts with the natural frequency of the beam - the resultant process of oscillations is no longer periodic (Figure 2.4 (c), (d)). Finally, the response of the system to last excitation is clearly nonlinear. The attractor in the phase plane diagram looks like a chaotic attractor even in a relatively short observation window (Figure 2.4 (f)). Also, a estimated value of Lyapunov exponent $\lambda = 1.7565$ is positive, which confirms that a response of the system is chaotic.

2.3. Computational reconstruction of time-averaged holographic fringes

Time-averaged holographic fringes illustrated in Figure 2.1 are based on the assumption that the structure performs harmonic oscillations. Dynamics analysis of the fixed-fixed beam MEMS model shows that transient processes can be very complex. Even in the most simple case periodic oscillations of the beam are not harmonic. This fact requires a separate analysis of processes governing the formation of time-averaged holographic fringes in the hologram plane.

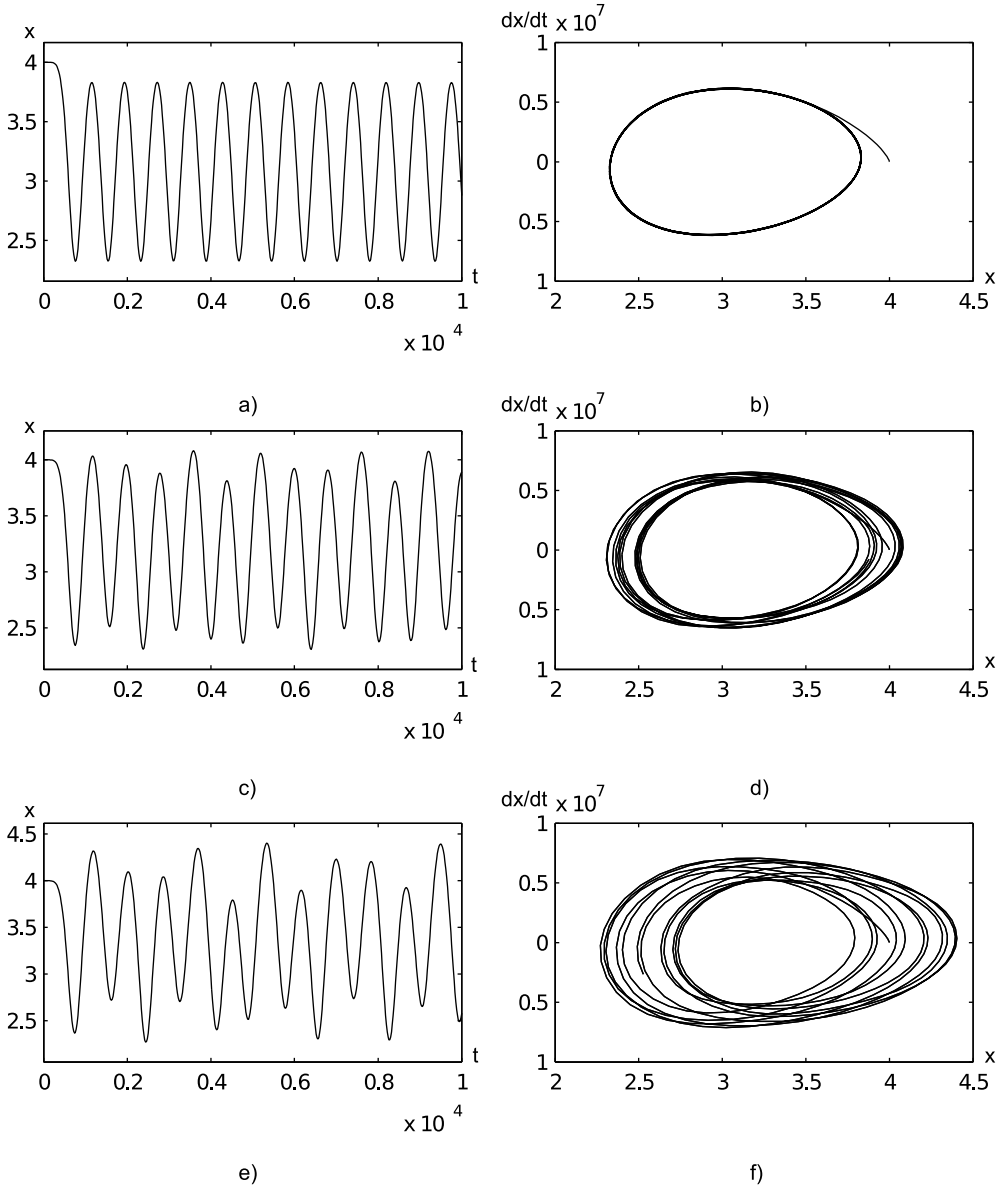

Figure 2.4: Results of simulations illustrating the dynamics of central node of the fixed-fixed beam. Parts a) and b) show the transient process in time and in phase diagram when the micro-device is excited according to the first computational experiment. Parts c) and d) [e) and f)] illustrate the results of the second (the third) computational experiments.

2.3.1. Computational reconstruction of time-averaged fringes

The characteristic function defining the complex amplitude of the laser beam M_T, when the according surface point performs oscillations defined by function $\xi(t)$, reads:

$$\begin{gathered} M_T = \lim_{T\to\infty}\frac{1}{T}\int_0^T \exp\left(\imath\frac{4\pi}{\lambda}\xi(t)\right)dt = \\ = \lim_{T\to\infty}\frac{1}{T}\int_0^T \cos\left(\frac{4\pi}{\lambda}\xi(t)\right)dt + \imath\lim_{T\to\infty}\frac{1}{T}\int_0^T \sin\left(\frac{4\pi}{\lambda}\xi(t)\right)dt = \\ = R_c + \imath R_s \end{gathered} \tag{56}$$

Note that when $\xi(t) = Z\sin(\omega t)$ the complex part R_s tends to zero because integrant is an odd function. Then M_T can be computed as an arithmetic average over discrete time steps in a period of harmonic oscillations:

$$\begin{gathered} M_T = \lim_{T\to\infty}\frac{1}{T}\int_0^T \cos\left(\frac{4\pi}{\lambda}Z\sin(\omega t)\right)dt = \\ = \lim_{n\to\infty}\sum_{k=1}^{n}\cos\left(\frac{4\pi}{\lambda}Z\sin\left((k-1)\frac{2\pi}{k}\right)\right)dt = J_0\left(\frac{4\pi}{\lambda}Z\right) \end{gathered} \tag{57}$$

But when oscillations are defined by a non-harmonic function $\xi(t)$, R_s does not converge to zero and the gray-scale level in the hologram plane reads (assuming that $a^2(x,y) = 1$):

$$|M_T|^2 = R_c^2 + R_s^2 \tag{58}$$

In practice one needs to compute arithmetic averages of R_c and R_s over a sufficiently long set of discrete points in the exposure time interval.

2.3.2. Time-averaged fringes induced by chaotic oscillations

It is well known that a non-linear system with a harmonic load may exhibit complex, chaotic solutions.

Lets denote intensity level of interference bands as stochastic time series defined by process $\xi(t)$. If given time series ξ_i is normally distributed with variance σ^2 then the intensity level of interference bands decrease exponentially.

$$E\xi^{2k-1} \equiv 0,\ k = 1, 2, \ldots$$

$$E\xi^{2k} \equiv 1\cdot 2\cdot \ldots \cdot (2k-1)\,\sigma^{2k} = (2k-1)!!\sigma^{2k},\ k = 1, 2, \ldots$$

$$|M_T|^2 = \lim_{m\to\infty}\left(\left(\frac{1}{m}\sum_{i=1}^{m}\cos\left(\frac{2\pi}{\lambda}\xi_i\right)\right)^2 + \left(\frac{1}{m}\sum_{i=1}^{m}\sin\left(\frac{2\pi}{\lambda}\xi_i\right)\right)^2\right) =$$

$$= \lim_{m\to\infty}\left(\frac{1}{m}\sum_{i=1}^{m}\sum_{k=0}^{+\infty}\frac{(-1)^k\left(\frac{2\pi}{\lambda}\xi_i\right)^{2k}}{(2k)!}\right)^2 =$$

$$= \left(\sum_{k=0}^{+\infty}\frac{(-1)^k\left(\frac{2\pi}{\lambda}\right)^{2k}}{(2k)!}\lim_{m\to\infty}\sum_{i=1}^{m}\frac{(\xi_i)^{2k}}{m}\right)^2 =$$

$$= \left(\sum_{k=0}^{+\infty}\frac{(-1)^k\left(\frac{2\pi}{\lambda}\right)^{2k}}{(2k)!}\cdot(2k-1)!!\cdot\sigma^{2k}\right)^2 = \left(\sum_{k=0}^{+\infty}\frac{(-1)^k\left(\frac{2\pi}{\lambda}\sigma\right)^{2k}}{(2k)!!}\right)^2 =$$

$$= \left(\sum_{k=0}^{+\infty}\frac{(-1)^k\left(\frac{2\pi}{\lambda}\sigma\right)^{2k}}{2^k k!}\right)^2 = \left(\sum_{k=0}^{+\infty}\frac{(-1)^k}{k!}\left(\frac{1}{2}\left(\frac{2\pi}{\lambda}\sigma\right)^2\right)^k\right)^2 =$$

$$= \exp^2\left(-\frac{1}{2}\left(\frac{2\pi}{\lambda}\sigma\right)^2\right)$$

The importance of this derivation cannot be overestimated - time-averaged holographic fringes do not form when the oscillation of the investigated object is chaotic. One should make sure that chaotic oscillations do not affect the components of the experimental setup before questioning the operability of the optical system - if only time-averaged hologram does not produce any fringes.

2.3.3. The formation of interference fringes

So far, the dynamics of the central point of the fixed-fixed beam is discussed (where the deflections from the state of equilibrium are largest). In order to visualize the dynamic of the whole surface of the beam, the whole field time-averaged holography simulation techniques were used, that were implemented in Matlab R2012b environment.

FEM modeling yields complete data on the dynamics of the fixed-fixed beam – distances between the beam plane and the ground plane are available from the simulation results for all time steps. The method described in the Sections [1.2.2, 2.3.1] will be applied for the data produced by all three computational experiments. Equation 26 is used for each point on the plane in order to determine the gray-scale level in time-averaged hologram. Laser wavelength used for calculation is set to $\lambda = 632.8[nm]$. Other parameters are set to $I_L = 1$; $k_d = 1$; $k_s = 0$. Note that non-specular surface of the beam is modeled.

Numerically reconstructed time-averaged holograms generated by the fixed-fixed beam according to the computational experiments (i), (ii) and (iii) are illustrated in parts a), b) and c) in Figure 2.5. Note that time-averaged fringes in part b) are less

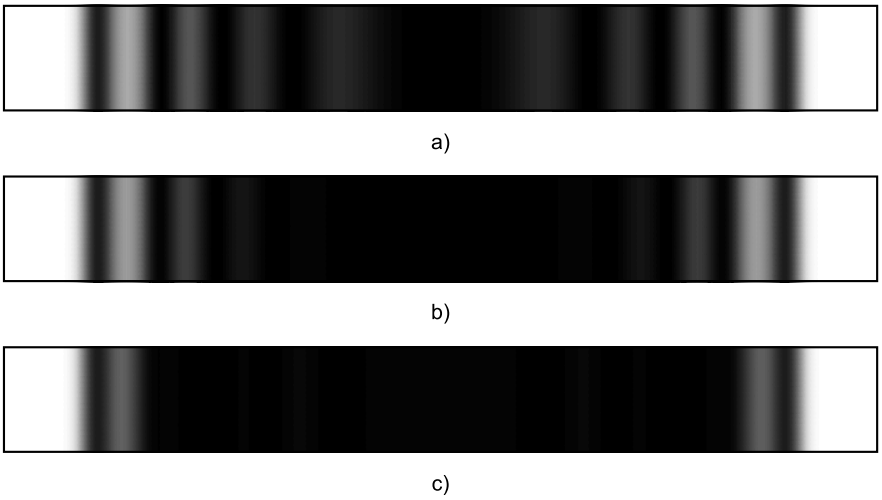

Figure 2.5: The formation of interference fringes for computational experiments (i), (ii) and (iii).

developed compared to part a). This can be explained by a much more complex transient process the beam is experiencing under excitation (ii). It is almost impossible to observe time averaged fringes in part c) – complex, chaotic oscillations do not generate time-averaged holographic fringes (these results correspond well to the analytical conclusions in Section 2.3.2).

2.3.4. The formation of interference fringes for periodic and harmonic oscillation laws

As mentioned previously, Figure 2.5 a) shows a well-developed pattern of time averaged-holographic fringes. Nevertheless Figures 2.6 a), c) suggest that oscillation process of the beam is not harmonic (though it is periodic). Natural is the question if it is possible to reconstruct such harmonic oscillation of the beam that its time-averaged hologram would look almost identical to Figure 2.5 a). In order to illustrate the complexity of the problem, maximum deflections of the beam are visualized when it does oscillate according to the data produced by computational experiment (i). Time graphs of three different points on the surface of the beam are shown in Figure 2.6 a); maximum deformations of the beam – in Figure 2.6 b).

Harmonic oscillations around the state of equilibrium (according to the first eigenmode of the beam) are illustrated in Figure 2.6 c), d). Now the maximum amplitude of harmonic oscillations must be preselected in such a way that the generated pattern of the time-averaged holographic fringes would be as close as possible to the pattern in Figure 2.5 a). It can be seen that the centers of time-averaged fringes in Figure 2.6 e) correspond to centers in Figure 2.5 a) (peak signal to noise ration value between these images is $PSNR = 23.2$).

An important conclusion follows from the above observations. One should not

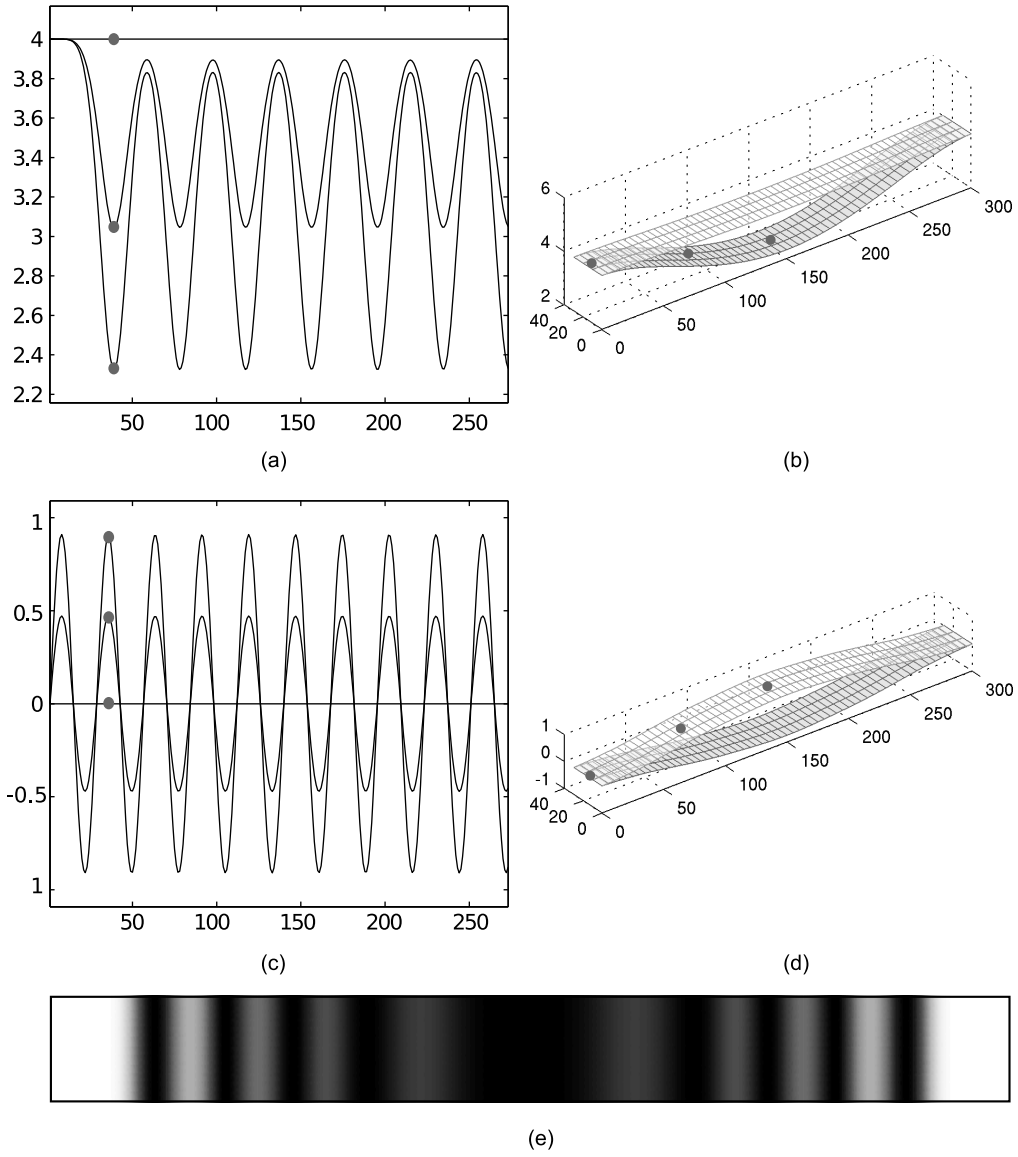

Figure 2.6: The formation of interference fringes for periodic and harmonic oscillation laws. Periodic oscillation process of the beam is is demonstrated in a). Minimum and maximum deflections of periodic oscillation are demonstrated in b). Harmonic oscillation process of the beam is is demonstrated in c). Minimum and maximum deflections of harmonic oscillation are demonstrated in d). A pattern of time-averaged fringes according to harmonic oscillations are demonstrated in e).

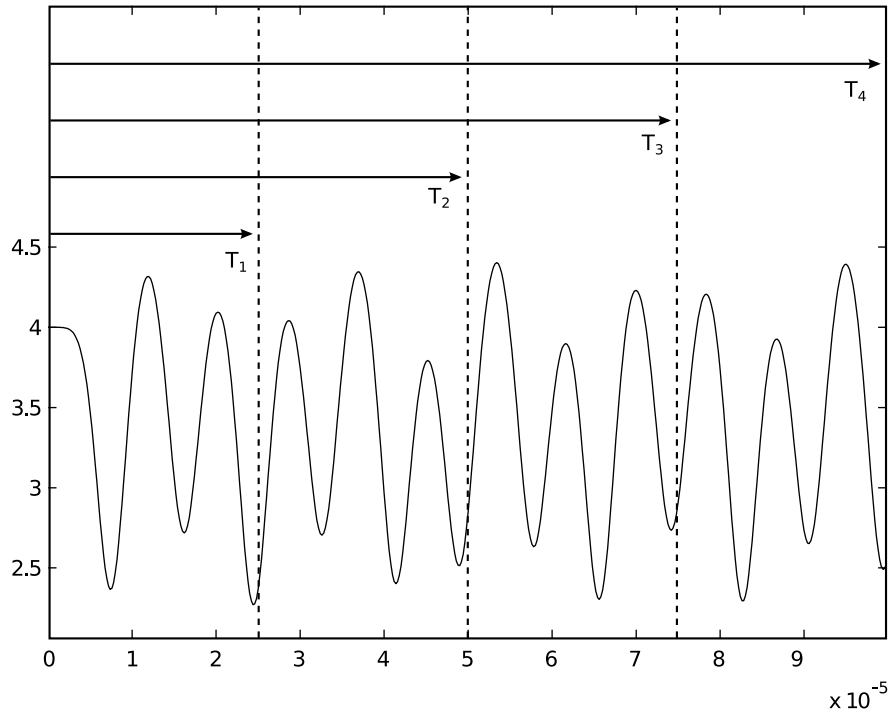

Figure 2.7: Computational experiment (iii) divided into time intervals (T1), (T2), (T3), (T4).

use straightforward techniques for the identification of the process of the oscillation from the available image of the time-averaged hologram. This inverse problem may become very complex if the motion law governing the dynamics of the analyzed structure is not known before the experiment.

2.3.5. The formation of interference fringes for different time intervals

The situation becomes even more complex when the oscillation is not periodic but is chaotic. As mentioned previously chaotic oscillations do not generate time-averaged holographic fringes. However, this result holds when exposure time tends to infinity. Finite exposure times result into interpretable patterns of fringes even for chaotic oscillations.

The same data produced by computational experiment (iii) is used, but time-averaged holograms are constructed for different exposure times (Figure 2.7). Time-averaged holograms for exposure times T_1, T_2, T_3 and T_4 are illustrated in Figure 2.8. A gradual loss of the time-averaged fringes can be observed as exposure time increases. That suggests another important conclusion. A straightforward identification of the motion law from time-averaged holographic fringes is prone to severe errors if the motion law of the investigated structure is not known. A short exposure time over a chaotic motion (Figure 2.8 a)) suggests a harmonic oscillation of the fixed-fixed beam - though this is completely not true. Another important conclusion follows from Figure

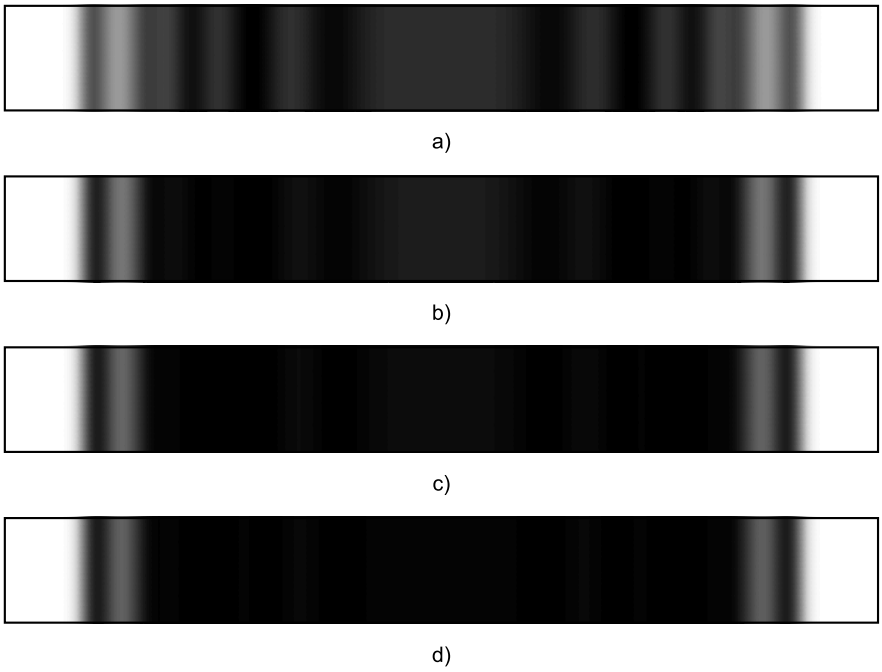

Figure 2.8: The formation of interference fringes for time intervals (T1), (T2), (T3), (T4).

2.8 d). One should not blame his optical setup if the generated time-averaged hologram does not yield a pattern of fringes. The optical setup may be in perfect order – simply the structure may be oscillating according to a chaotic law.

2.4. Experimental results

The methods of holographic interferometry allow to get much more information about the deformable surface comparing with other experimental methods. Because of this holographic interferometry methods are widely applied in mechanics, biology, non-destructive control, automotive industries, microsystem engineering ,and others areas.

Digital holography technology uses real-time, 3D, full field-of-view surface measurements to eliminate point-by-point data gathering. Holograms are used to measure the surface of any component. Superb resolution allows for monitoring shape changes that are smaller than 20 nanometers for superb accuracy and resolution of the results.

Measurements of vibration amplitudes of the surface of MEMS, as functions of operating conditions of the MEMS, were performed using the optoelectronic laser interferometric microscope. The methodology of investigation using optical microholographic system for recording resonance frequencies of vibrating mechatronic system is presented in paper Hayman et al. (2006).

The general view of PRISM setup is presented in Figure 2.9. PRISM combines all the necessary equipment for deformation and vibration measurement of most materials in a small, lightweight system. A standard system includes holography and computer

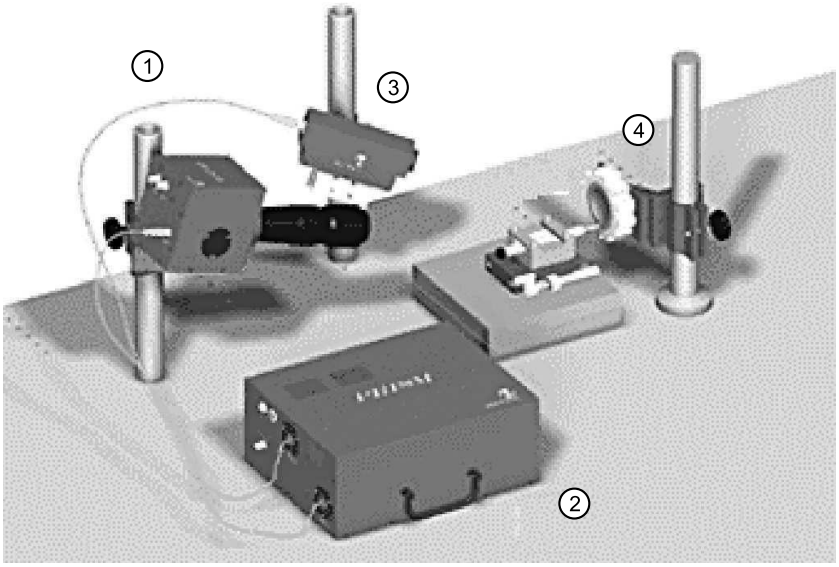

Figure 2.9: PRISMA system setup: (1) - videohead; (2) - control block; (3) - illumination head of the object; (4)-investigated object.

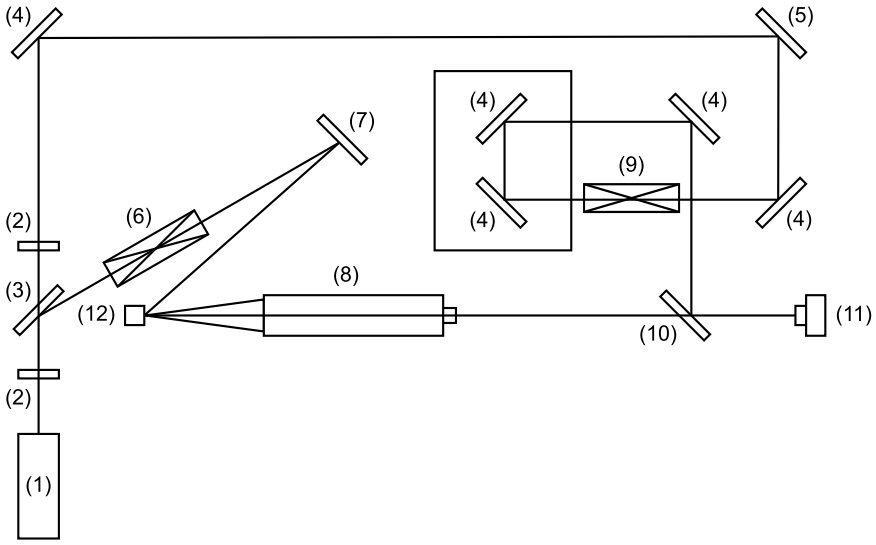

Figure 2.10: Schematic diagram of the microscopic holographic system: (1) - He-Ne laser; (2) - $\frac{\lambda}{2}$ plate (λ - length of the laser wavelength); (3) directional beam splitter (PBS); (4), (5), (7) - mirrors; (6) spatial filter; (8) - microscope; (9) - telescope; (10) proximal beam splitter; (11) - CCD camera; (12) - analyzed object MEMS.

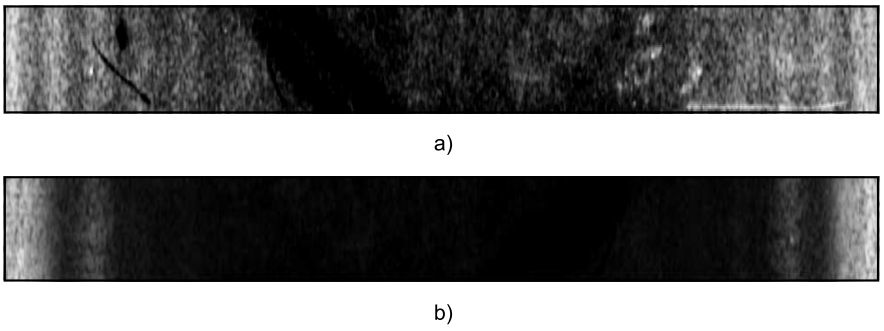

Figure 2.11: Holographic interferogram of vibrating fixed-fixed beam when performing: periodic oscillations a); chaotic oscillations b).

systems integrated with proprietary state of the art software. The main parts of the PRISMA system setup are presented in Figure 2.9.

Success in deformation and vibration measurement requires a fast affordable solution. PRISM offers a high-speed holographic technique for production measurement of vibration and deformation without surface contact and minimal sample preparation. PRISM can access complex geometries (deep recesses or curves) difficult or impossible for other techniques and can be configured for specific needs in experimental investigation of mechatronics systems. The PRISM system videohead was modified in order to make registration microscale objects possible.

Optical micro-holographic system for recording resonance frequencies of MEMS is illustrated in Figure 2.10. A coherent laser beam is passed through $\lambda/2$ plate (2). It then passes to a directional beam splitter where one part through the spatial filter (6) and mirror (7) illuminates investigated MEMS (12) and mirror to MEMS device (12). The other through optical elements (2), (4), (5), (9), (10) are directed to CCD (11).Consequently, from the observation point, two intensity distributions are viewed: one of the light reflected from the object (12) and second arising from reflection off the bottom surface of proximal beam splitter (10). The reflected light from MEMS is transmitted back through the long distance microscope objective (8) and proximal beam splitter (10) to a digital camera CCD (11). Images are recorded by the camera of vibrating fixed-fixed beam that is performing periodic and chaotic oscillations. The results are given in Figure 2.11. These experiments were conducted according to sections 2.1 and 2.2 of this thesis. It can be seen from Figure 2.11 that results correspond well with computational results in Section 2.3.3 – decay of intensity is obvious in part b), when the fixed-fixed beam is performing chaotic oscillations.

The wave fronts are planar in the setup that used in this study, thus parallel interference fringes result when the proximal beam splitter is introduced into the path. Single frame images captured by the CCD and proceeded by computer gives a valuable insight in the motion of investigated MEMS.

2.5. Conclusions

Time averaged holography is a powerful optical experimental technique for investigation of microsystem components. The inverse problem for the interpretation of time-averaged holographic fringes is a well defined and straightforward task if only the oscillations of the investigated structures are harmonic. It is demonstrated that complex, chaotic motions can be generated even in rather simple micro-electromechanical systems. Therefore, a straightforward interpretation of time-averaged holographic interferograms of micro-mechanical components can not only be misguiding but the experimental holographic images may not reveal any interpretable fringes at all.

A relationship between the decay of intensity in a time-averaged holographic interferogram and the intensity of chaotic motion is explicitly derived. It is shown that chaotic oscillations do not generate time-averaged holographic fringes. Thus, one needs to make sure that the response of the excited electro-mechanical system is not chaotic before questioning the functionality of the optical experimental setup. The derived analytical results yield a deeper insight into the dynamical properties of MEMS components.

3. INTERPRETATION OF OPTICAL PATTERNS OF FRINGES

As mentioned previously, applicability of the interferometric techniques in more demanding environments requires reliable computational tools for the interpretation of experimental images. The reconstruction of the 2D map of fringe centerlines is one of the main factors ensuring the accuracy of the interpretation of optical measurement results. The main objective of this chapter is to propose a general scheme for the construction of the centerline contour map from an experimental optical image. The proposed computational technique comprises three main steps:

- The thresholding of the experimental image.
- The thinning of the fringes on morphological mathematical operations and midpoint detection method.
- The reconstruction of the map of continuous curves from the binary matrix of pixels representing fringe centerlines.

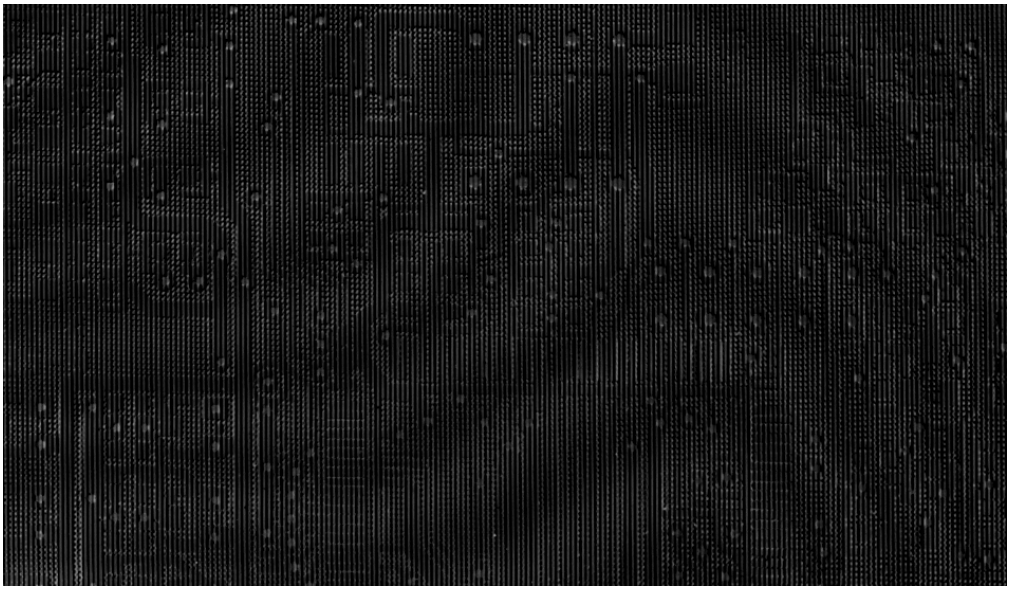

Figure 3.1: The experimental image of PCB containing interfernce fringe pattern

3.1. Experimental image

Experimental image shown in Figure 3.1 will be used to demonstrate the proposed algorithm. The shadow moiré technique was used to acquire interference fringe pattern. A digital image of an array of dark and white lines is projected onto the surface of a printed circuit board (PCB); the angle of the incident light is 20 degrees. This image contains background noise as well as non-uniform lightning. Thus, straightforward processing might yield incorrect results. The general view of the optical experimental

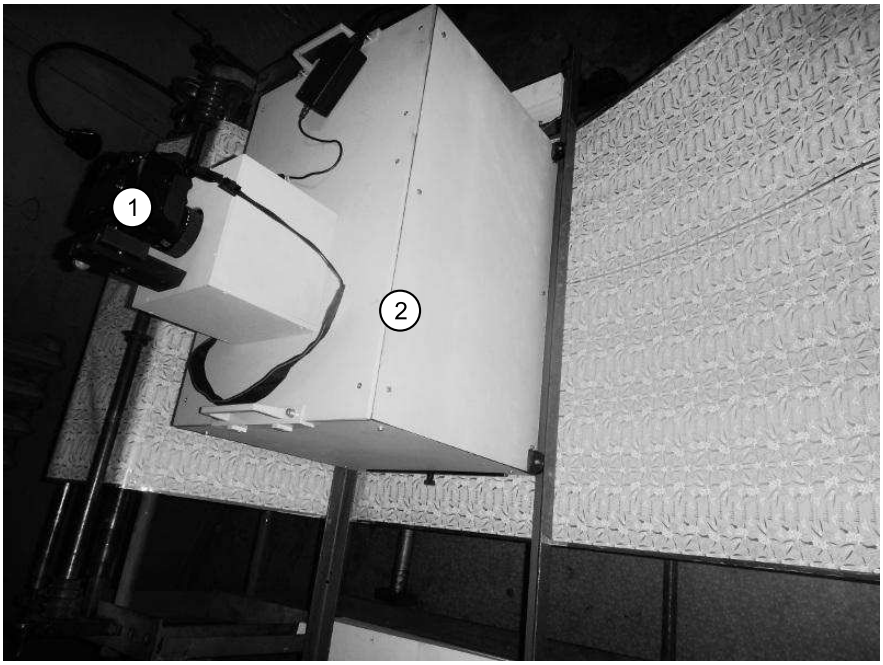

Figure 3.2: The optical experimental setup of a shadow moiré system comprising a camera (1) and a shadow moiré experimental system (2).

setup is shown in Figure 3.2.

The main objective of this chapter is the development of a reliable algorithm for the reconstruction of 2D map of centerlines of projected fringes. Computational aspects of the algorithm will be discussed in the following sections, and experimental image in Figure 3.1 will be used for testing of the proposed approach.

Computational tools were developed, for centerline identification in experimental optical images, proposed in this section. Python (including NumPy and SciPy packages) has been used for developing these tools.

3.2. Thresholding

The first step towards the identification of centerlines is the construction of a binary representation of the optical experimental grayscale image. The quality of the resulting binary image is crucial for the remaining steps. Various thresholding techniques can be exploited for the construction of the binary representation of the original experimental image (Sankur, 2004) (though not all of them may produce a desired result). Thresholding may be viewed as an operation that involves tests against a function T of the form:

$$T = [x, y, f(x), p(x)] \tag{59}$$

where $f(x, y)$ is the gray level of point (x, y) (the original experimental image) and $p(x, y)$ denotes some local property of this point Gonzalez (2008). A thresholded im-

age $g(x, y)$ is defined as:

$$f(x,y) = \begin{cases} 1, & f(x,y) < T \\ 0, & f(x,y) \geq T \end{cases}. \tag{60}$$

The threshold is called global in case when T depends only on $f(x, y)$ and the threshold is called local if T depends on both $f(x, y)$ and $p(x, y)$.

It is clear that straightforward application of global thresholding methods (like histogram shape-based methods) to the test image cannot produce acceptable results due to the non-uniformity of lighting Figure 3.1; even though global methods are fast and reliable with images having uniform lighting (Anand, 2003).

Local thresholding based on the mean gray value of neighboring pixels surrounding the current pixel (x, y) are to be used in order to produce the binary image. The following convolution operation with a square matrix of order w is used for that purpose:

$$\rho = \frac{1}{m \times n} \cdot \begin{bmatrix} 1 & 1 & \dots & 1 \\ 1 & 1 & \dots & 1 \\ \dots & \dots & \dots & \dots \\ 1 & 1 & \dots & 1 \end{bmatrix} \tag{61}$$

Moreover, it is required that w is an uneven number. The matrix p is constructed as a result of convolution between matrices g and ρ:

$$p(x,y) = \sum_{k_1=-a}^{a} \sum_{k_2=-a}^{a} \rho(k_1,k_2)\, g(x+k_1, x+k_2) \tag{62}$$

where the parameter a ensures that the pixel (x, y) is located at the center of the current observation window:

$$a = \frac{w-1}{2} \tag{63}$$

The resulting matrix p comprises mean values of neighboring pixels and can be effectively used to perform the local thresholding operation. The selection of the size of the matrix ρ is in general empirical, but a well-balanced choice could be determined as:

$$w = \frac{\max(m,n)}{10} \tag{64}$$

where m and n are the dimensions of the original image (measured in pixels). Such a selection could be explained by the requirement, that at least one moiré fringe (including a portion of the background) would fit into the observation window. Note that the convolution may be computed using the FFT what will give a definite speed advantage against direct convolution operation.

The structure of the original optimal image suggests that initial smoothing before the thresholding procedure may help to gain better representation of fringes in the

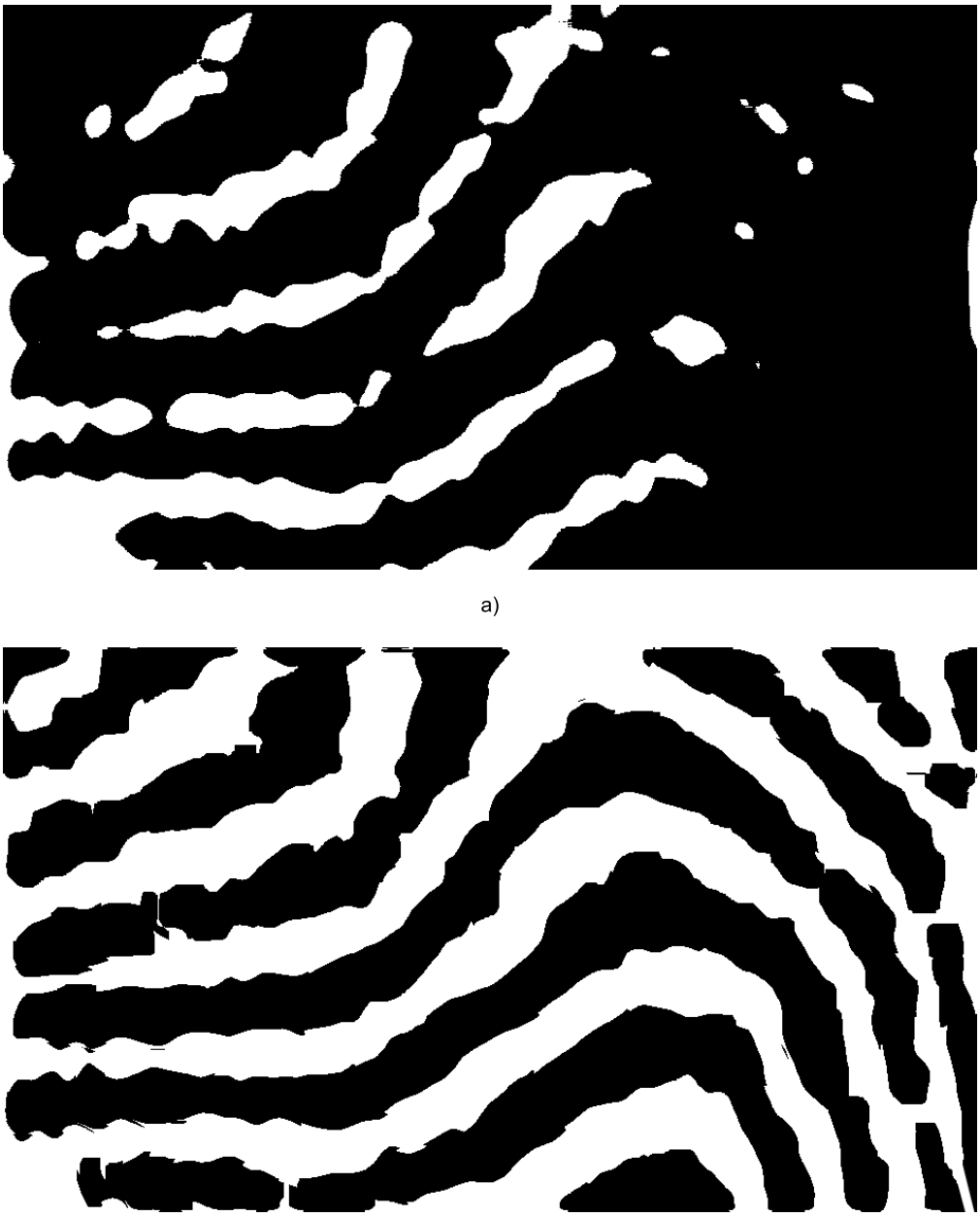

a)

b)

Figure 3.3: The binary representation of image when using global thresholding a) and local thresholding b) methods.

thresholded image. Note that the smoothing operation could be performed applying the convolution operation described above by using the Gaussian kernel matrix. The size of Gaussian kernel matrix depends on the noise level.

Special care should be paid to the boundary regions of the initial image. The computation of $p(x, y)$ requires values of $g(x + k_1, y + k_2)$ –- but there could be situations when those values do not exist:

$$\begin{array}{c} x < |k_1|\,,\ k_1 < 0,\ \text{or}\ y < |k_2|\,,\ k_2 < 0 \\ x > |m - k_1|\,,\ k_1 > 0,\ \text{or}\ y < |n - k_2|\,,\ k_2 > 0 \end{array} \tag{65}$$

The most common way to deal with this problem is to calculate $p(x, y)$ only in the area $k_1 < x < m-k_1$ and $k_2 < y < n-k_2$. But such approach has a disadvantage of losing information on the boundaries. A better method would be to extend the thresholded image by $(w - 1)/2$ to all directions and to fill these parts by flipping corresponding parts of the original matrix at the boundaries.

The results of the thresholding step are demonstrated in Figure 3.3. It is clear that a local thresholding method provides more reliable and betters results compared to global thresholding.

3.3. Identification of fringe centerlines

Two alternative techniques for the identification of centerlines from the thresholded experimental image are investigated in this section. The first technique is based on the identification of centerlines by the mid-point method and the second technique is based on mathematical morphological operations.

3.3.1. Mid-point detection method

The direct application of the algorithm proposed in (Anand, 2003) would produce poor results due to non-uniform lightning conditions in the initial experimental image. And though local thresholding and image smoothing operations can improve the functionality of the mid-point detection method, the described row and column scans still produce an unsatisfactory image (as shown in Figure 3.4) due to a large number of fractures in the pattern of centerlines and loose spurs in areas between centerlines.

3.3.2. Mathematical morphological operations

Mathematical morphology is a tool for extracting image components that are useful in representation and description of regions or shapes such as boundaries of a region, skeletons or other patterns. Various morphological operations like dilation, erosion, opening, closing, thinning, thickening and others have been developed and are successfully applied in different areas of pattern recognition science and technology (Banon, 2013). In this section, the thinning operation will be used based on the hit-or-miss algorithm since simple erosion operation would destruct smaller parts of moiré fringes in the thresholded image. The thinning operation is defined through the erosion

Figure 3.4: The identification of centerlines using mid-point detection method.

"-" operation and the hit-or-miss "*" operation (Gonzalez, 2008):

$$A * B = (A - B) \cap A^C - B_2 \tag{66}$$

where A denotes the thresholded image; A_c is the compliment matrix of A; B_i stands for the structuring element of the thinning operation. Note that B_i may contain values 0, 1 or the empty element that does not discriminate between 0 or 1. All possible rotations of both structuring elements are being used in each step.

The structuring element B_i slides over the binary image and the pixel corresponding to the center of the template is set to 1 if the template matches the image and is set to 0 otherwise.

In each iteration structuring elements B_i, $i = 1, 2$ defined in Figure 3.7 are being used to identify the edge pixels to be removed, followed by the removal of them.

Thus, the thinning operation $\otimes$ can be explicitly defined by:

$$A \otimes B = A / (A * B) \tag{67}$$

The thinning operation is an iterative process and is repeated until no further changes occur.

The execution of the thinning process produces undesired parasitic components (spurs) around actual centerlines of moiré fringes Figure 3.5. These spurs are caused during erosion by non-uniformities in objects and may be removed by performing the pruning operation Gonzalez (2008).

A smooth and noise-free pattern of centerlines is produced in the result of the described digital image processing operations (Figure3.6). Unfortunately, a number of

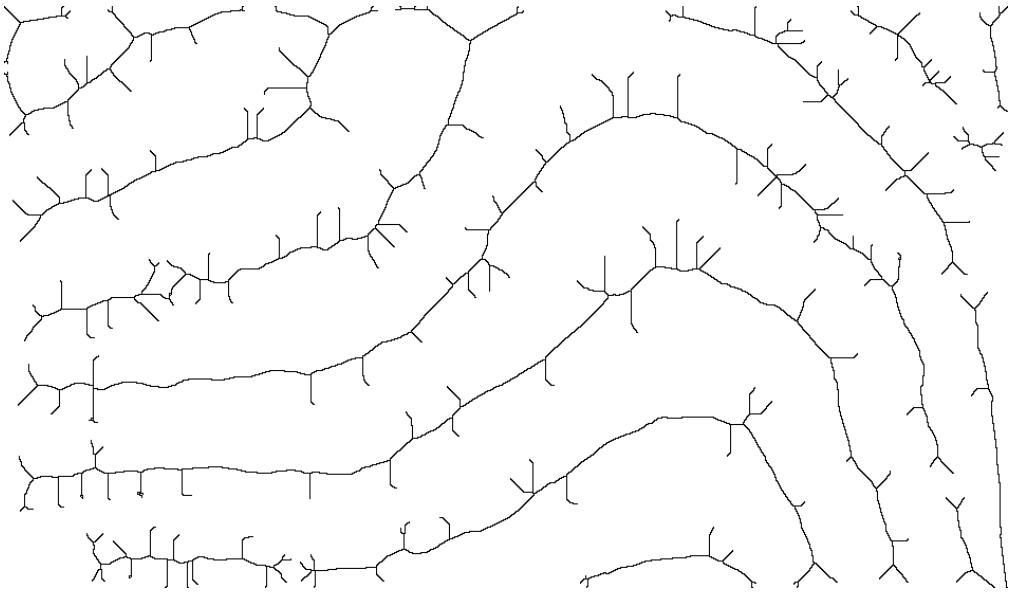

Figure 3.5: The identification of centerlines using mathematical morphological operations.

intermittent broken centerlines can still be visible in Figure 3.6. Some of these defects are caused by optical defects in the original image. Appropriate joining of broken centerlines could considerably improve the quality of interpretation of the optical experimental image. Mahotas package was used for performing mathematical morphological operations.

3.4. Identification of continuous curves

So far fringe thinning operations resulted into a matrix of black and white pixels. The joining of broken centerlines requires identification of continuous intervals of curves in produced digital image. The main objective of this section is to develop a reliable method for grouping sets of adjacent pixels into curves and filling possible fractures inside separate curves. The proposed method can be divided into the following steps:

- Division of image into grid cells
- Derivation of approximate line equation in each cell containing black pixels
- Grouping contacting cells into curves
- Identification and joining of curves with fractures

3.4.1. The generation of the grid

In general, the selection of the size of the grid cell w_g is an empirical procedure, but it should be related to the density of moiré fringes in the original optical image. The main requirement from the point of the reliable functionality of the proposed algorithm

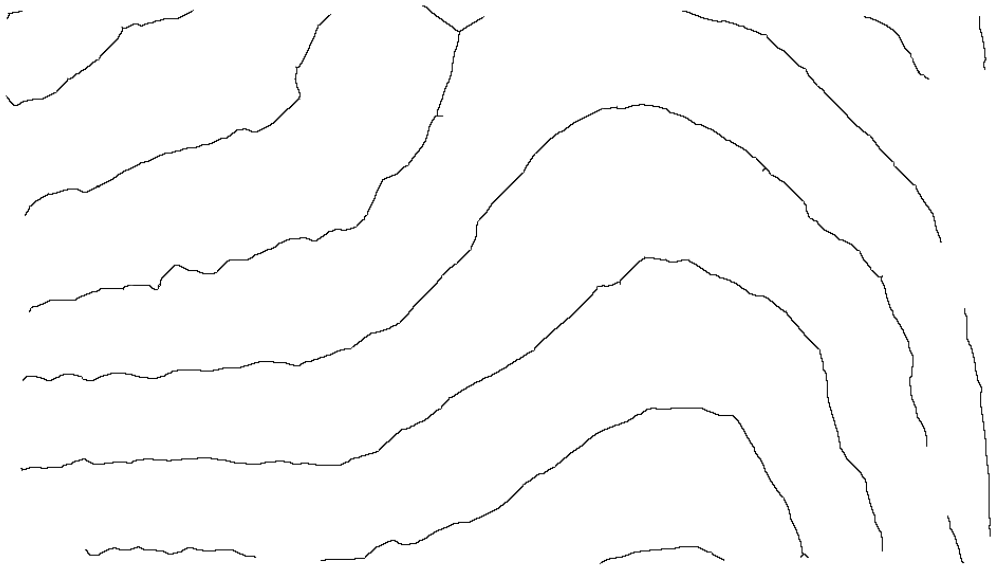

Figure 3.6: The results of the pruning operation applied to the thinned image.

0	0	0
	1	
1	1	1

	0	0
1	1	0
1	1	0

Figure 3.7: The structuring elements used for morphological thinning operation.

is that there should be only one centerline passing through each grid cell. On the other hand, a larger cell size increases the performance of the proposed method.

3.4.2. Identification of line equations

The algorithm is started by sweeping cells of the thinned image (from left to right and from top to bottom) searching for cells containing black pixels. In case the current cell contains black pixels the following parameters of the line crossing that cell should be identified: the slope, the intercept, the angle, and the mid-point of the line (it is assumed that the cell size is small enough to represent a curve as a line segment inside the cell). Several alternative options for the construction of a line in a cell exist:

(i) Identification of black pixels on the boundaries of the current cell and the construction of a line running through these pixels.

(ii) Construction of the linear statistical regression line through the array of black pixels in the current cell.

(iii) Exploiting Hough (Radon) digital image transforms for the identification of a line in the current cell.

The first option is the fastest solution from all three, but is not viable because the thinned curves may break near the boundary of the current cell. Moreover, this method is not resistant to the additive noise what could significantly distort the resulting image.

The method based on the linear statistical regression would cope with the additive noise well, but problems would occur when vertical lines should be reconstructed in the current cell.

Radon (Radon, 1917) or Hough (Duda et al., 1972) transforms are probably the most reliable solution for robust identification of a line in a cell. Both transforms can be effectively used for the detection of simple shapes such as lines, circles, ellipses by making a transformation from the image space to the parameter space.

A line in plane can be defined by:

$$x \cos(\theta) + y \sin(\theta) = r \tag{68}$$

where r is the distance between the line and the origin (the bottom-left corner of the rectangular cell); θ is the angle of the vector from the origin to this closest point of the line. The main idea behind Hough transform is based on the fact that points in the image space correspond to sinusoids in the parameter space. If an array of points in the image space does form a line, then the intersection of sinusoids creates a point in parameter space (parameters of the line in the image space can be deduced from the coordinates of that point). To gain better performance a variant of Hough transform, Randomized Hough transform (RHT) (Xu et al., 1990) was selected and then applied to every cell of the thinned image. Randomized Hough Transform uses a many-to-one mapping from the image space to the parameter space. The algorithm works by randomly selecting two points (x_1, y_1) and (x_2, y_2) and solving the system of equations:

$$\begin{cases} y_1 = k_{12} x_1 + b_{12} \\ y_2 = k_{12} x_2 + b_{12} \end{cases} \tag{69}$$

where (k_{12}, b_{12}) determines a point in the parameter space. The linked list of points in the parameter space is organized incrementally; a threshold value for the numbers points that are required for the recognition of a line in the image space must be defined beforehand. A new matrix of vectors comprising basic line parameters (the angle θ and the location of the line mid-point x and y in each grid cell) is constructed from the output data of the RHT:

$$G = \{(\theta_{i,j}, x_{i,j}, y_{i,j}) \,|i \in [1, m_g], j \in [1, n_g]\} \tag{70}$$

where $m_g \times n_g$ is the number of grid cells in the vertical and the horizontal directions. It is possible that more than one line can be discovered in a cell due to noise or spurs; thus the longest line interval is identified as the part of the reconstructed curve.

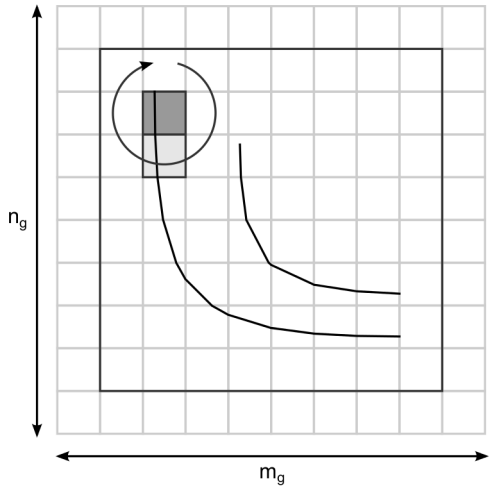

Figure 3.8: Scanning for cells with assigned lines around the current cell (marked as the dark gray cell).

3.4.3. Grouping contacting grid cells into curves

The proposed method for grouping contacting cells into curves is given below:

(i) Append a single layer of empty grid cells around the grid matrix G.

(ii) Proceed with cells from left to right and from top to bottom starting at cell $G_{1,1}$.

(iii) Check if there are cells with an assigned line in the immediate surroundings of $G_{i,j}$ (Figure 3.8).

(iv) Select a nearest cell with the assigned line $G_{k,l}$ to the current cell $G_{i,j}$ and assign $G_{k,l}$ to the set of cells belonging to the same curve C_i (Figure 3.8 b)). Remove cell $G_{i,j}$ from the G matrix.

(v) Repeat step (iii - iv) with cells $G_{k,l}$ until $G_{k,l}$ has no surrounding cells with assigned lines.

(vi) Return to cell $G_{i,j}$ and continue with the next cell in a row (column); go to step (iii).

3.4.4. Joining curves with fractures

Some curves may have fractures larger than one cell due to defects in the initial image or loss of information during the previously described steps. An adaptive method for the identification and joining of curves with fractures is proposed in this section.

A set of curves is already identified (each curve is associated to a set of cells). Thus, it is possible to define various criteria that could be used to decide if two separate curves could be joined. The first criterion that is the distance between the edge cells of

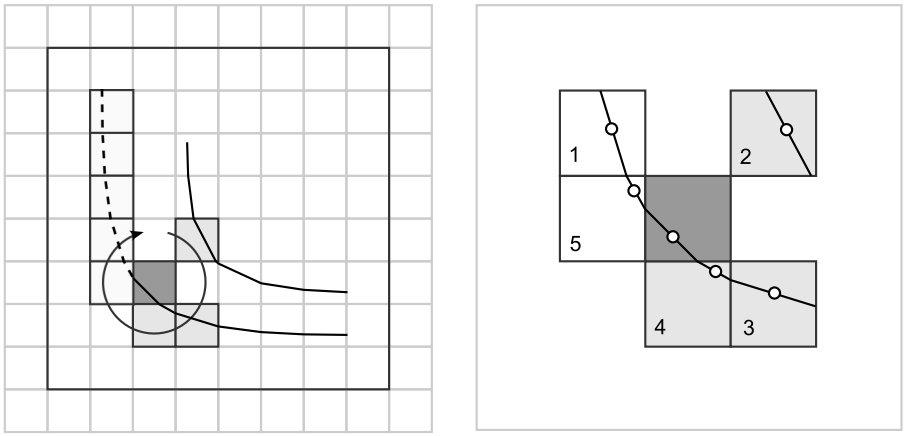

Figure 3.9: A schematic diagram illustrating the selection of the next grid cell. Part a) shows the current cell in dark gray and unprocessed cells (with the assigned line) in the vicinity of the current cell in light gray. The thick light gray line denotes the set of cells assigned to the current curve. Part b) illustrates the selection of correct nearest neighbors –- cell 4 is selected instead of cell 3 or cell 2 (it belongs to the other curve); empty circles denote line centers inside appropriate cells.

the curve:

$$d_{i,j} = \sqrt{(x_i - x_j)^2 - (y_i - y_j)^2} \tag{71}$$

where (x_i, y_i) and (x_j, y_j) are all possible pairs of the center points of the edge cells of the identified curves. The other criterion could be the orientation between edge cells of curves $|\theta_i - \theta_j|$. Anyway, a number of computational experiments have shown that there could be situations where that criterion does not work as expected. Thus, an alternative criterion reads Figure 3.10 b):

$$a_{i,j,1} = |\theta_i - \theta_{i,j}| \text{ or } a_{i,j,2} = |\theta_j - \theta_{i,j}| \tag{72}$$

where $\theta_{i,j}$ is the angle of line running through points (x_i, y_i) and (x_j, y_j) and the x-axis.

Maximum allowed values for defined criteria should be selected depending on the complexity initial image. Parameter $d_{i,j}$ should be constrained to average distance between fringes and the values of parameters $a_{i,j,1}$ and $a_{i,j,2}$ are limited to 30 degrees.

The parameter $J_{i,j}$ is defined, which is used when there are more than one curve holding against defined criterion constraints:

$$J_{i,j} = \frac{1}{d_{i,j} + \alpha\,(a_{i,j,1} + a_{i,j,2})} \tag{73}$$

where α is a weight which allow to emphasize the importance of the distance between the edges or the variation of angles at the edges. The defined curve joining criterions are incorporated into the proposed algorithm for curve joining.

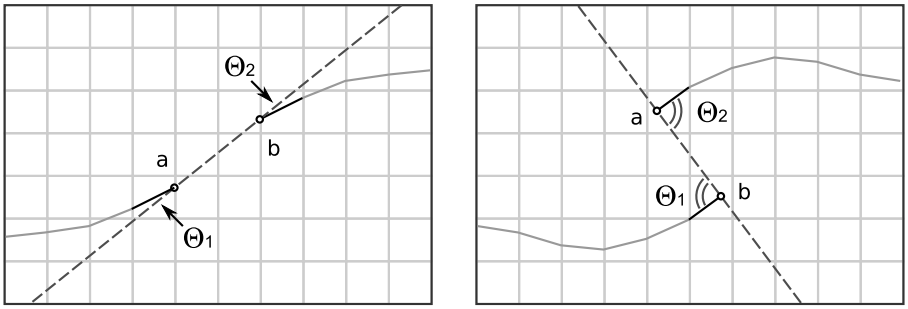

Figure 3.10: A schematic diagram in a) illustrates a favorable connection between two curves; the $|\theta_i - \theta_j|$ criterion would be sufficient for the detection of similar angles between lines in the edge cells. A schematic diagram in b) illustrates an unfavorable connection between two curves; the $|\theta_i - \theta_j|$ criterion would suggest a connection while the alternative criterion eliminates a possible connection between the edge cells

(i) Select a curve C_i from the set C.

(ii) Compute criteria $d_{i,j}$, $a_{i,j,1}$, $a_{i,j,2}$ between curves C_i and C_j ; $i \neq j$ for all available edges.

(iii) Merge all cells of the curve C_j with C_i for such i and j minimizing the value of $J_{i,j}$ on the corresponding edges. Remove C_j from the set C and repeat steps (ii-iii) until there are no more favorable connections.

(iv) Proceed with the curve C_i and repeat steps (i-iii).

The result of this procedure can be seen in Figure 3.11.

3.5. Application scenarios

The proposed method can be applied in various industrial areas such as PCB warpage identification, MEMS reliability control, and others. The application of whole field projection moiré method for the registration of radial pulses will is discussed in this section. The pulse of a wrist is considered to be one of the most fundamental signals of life, which carries essential information about a health of the person. Pathologic changes in a body are reflected by fluctuation patterns of radial pulses. For example, clinical studies indicate that patients with hypertension, cardiovascular disease, and diabetes exhibit premature loss of arterial elasticity, The projection moiré technique allows obtaining the relief of an object. The application of the projection moiré method used for measuring of out-of-plane displacements by the changes in relief between the two prompting states is used in this section. The field of displacements can be extracted from the pattern of fringes produced by a double exposition of images in both states.

3.5.1. Mathematical representation of the projected image

A paraxial model was used in the following steps (this condition can be implemented by using a projector that is placed far from the object and by placing the imag-

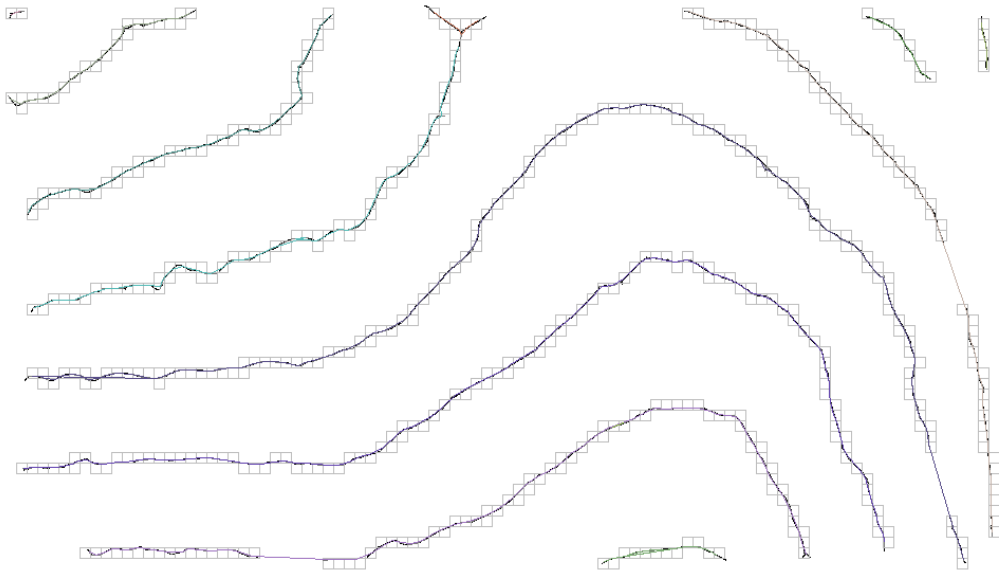

Figure 3.11: The reconstructed pattern of fringe centerlines.

ing system far away from the object). In practical applications, one should consider an important factor – a depth of focus. A camera can focus only one plane; all the other points on the analyzed surface experience a change of coordinates, as this can introduce errors. Thus a paraxial model is adopted here, so we no longer need to deal with the depth of focus and the effects of perspective that are caused by a source of light. In this case, the angle between the direction of observation and the direction of illumination is θ and the direction of observation is perpendicular to the x-axis. Representation of the optical projection, which is one-dimensional, on a diffuse surface is given in Figure 3.12. The projected image $F(y)$ is defined in a frame $y0F$, that is rotated by an angle θ with respect to frame $x0G$. The function $F(y)$ determines a gray value level of a ray traveling through a point y_0 along the F-axis. Therefore, it is assumed that $0 \leq F(y) \leq 1$, where 0 represents the black color, 1-white color and all intermediate values are appropriate grayscale levels. The functional illustration is given in Figure 3.12:

$$\vec{e}_y = (\cos\theta; \sin\theta) \tag{74}$$

$$\vec{n}_y = (-\sin\theta; \cos\theta) \tag{75}$$

$$\vec{t}_G = \left(\frac{1}{\sqrt{1 + (G'_x(x))^2}}; \frac{G'_x(x)}{\sqrt{1 + (G'_x(x))^2}} \right) \tag{76}$$

$$\vec{n}_G = \left(-\frac{G'_x(x)}{\sqrt{1 + (G'_x(x))^2}}; \frac{1}{\sqrt{1 + (G'_x(x))^2}} \right) \tag{77}$$

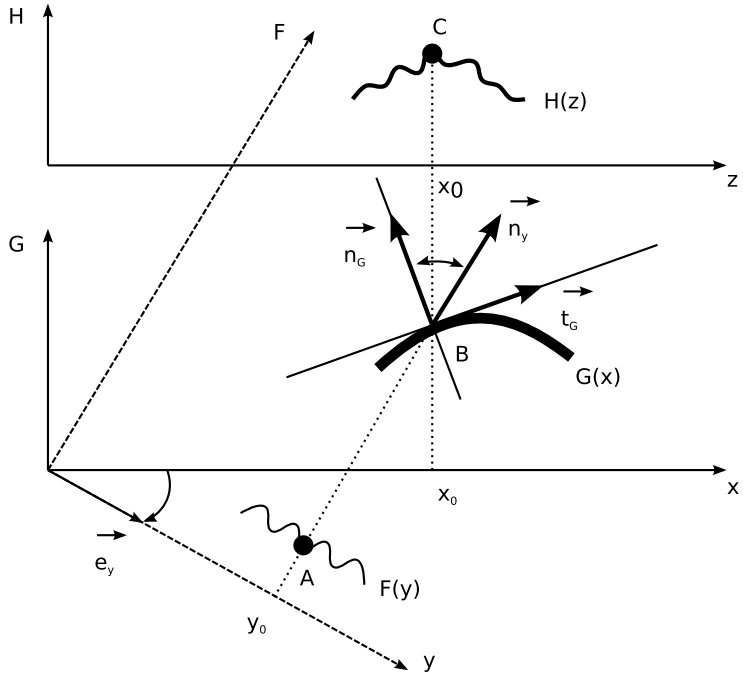

Figure 3.12: Geometrical representation of an optical projection on a diffuse surface. $F(y)$ is projected image, $G(x)$ is diffuse deformed surface, $H(z)$ is an observed image.

As mentioned previously, $G\,(x)$ defines a diffuse surface. Therefore, an observed grayscale level at a point z is:

$$H\,(z) = H\,(x) = F\,(x)\cos\alpha \tag{78}$$

$$\cos\,(\alpha) = (\vec{n}_y \cdot \vec{n}_G) = \frac{\cos\theta + G_x^{'}\,(x)\sin\theta}{\sqrt{1 + (G_x^{'}\,(x))^2}} \tag{79}$$

The following equation holds for all positive x and y:

$$y = x\cos\theta - G\,(x)\sin\theta \tag{80}$$

Thus, an exact description of the image formation process can be described as:

$$H\,(x) = F\,(x\cos\theta - G\,(x)\sin\theta)\,\frac{\cos\theta + G_x^{'}\,(x)\sin\theta}{\sqrt{1 + (G_x^{'}\,(x))^2}} \tag{81}$$

The double-exposure projection moiré method comprises two steps. In the first step, the grating is projected on a surface $G\,(x)$ obliquely to the direction of viewing and the photo of an observed grating is captured. Then, the object is deformed (imaging and the grating projection systems remain unchanged) and the photo of the observed grating

is captured again. Moiré fringes are produced by superposition of these two images, so they can be used to identify the scale of object deformation. The surface of the deformed object is described as $G(x)+g(x)$, where $g(x)$ is the absolute deformation of the object in the direction of observation after applying the load. We will assume is a harmonic moiré grating is projected:

$$F(y)=\frac{1}{2}+\frac{1}{2}\cos\left(\frac{2\pi}{\lambda}y\right) \tag{82}$$

here λ is the pitch of the grating. Also, we will define function $g(x)$ as a slowly varying function. Thus, it is required that:

$$F(y)=\frac{1}{2}+\frac{1}{2}\cos\left(\frac{2\pi}{\lambda}y\right) \tag{83}$$

Then, subtractive superposition of the grating before and after applying the load gives:

$$\begin{gathered}\frac{1}{2}+\frac{H_1(x)-H_2(x)}{2}\times\frac{\sqrt{1+\left(G'_x(x)\right)^2}}{\cos\theta+G'_x(x)\sin\theta}\approx\\ \approx\frac{1}{2}+\frac{1}{4}\cos\frac{2\pi}{\lambda}\left(x\cos\theta-G(x)\sin\theta\right)-\\ -\frac{1}{4}\cos\frac{2\pi}{\lambda}\left(x\cos\theta-\left(G(x)+g(x)\sin\theta\right)\right)=\\ =\frac{1}{2}-\frac{1}{2}\left(\sin\frac{2\pi}{\lambda}\left(x\cos\theta-G(x)\sin\theta-\frac{g(x)\sin\theta}{2}\right)\right)\times\\ \times\sin\left(\frac{2\pi}{\lambda}\frac{g(x)\sin\theta}{2}\right)\end{gathered} \tag{84}$$

where $H_1(x)$ and $H_2(x)$ are observed gratings before and after applying the load. The previous equation represents the effect of beats. In this case, the envelope function is:

$$\frac{1}{2}\pm\frac{1}{2}\sin\left(\frac{2\pi}{\lambda}\frac{g(x)\sin\theta}{2}\right) \tag{85}$$

Moiré fringes form at:

$$\frac{\pi g(x)\sin\theta}{\lambda}=\pi N;\ N=0,\pm1,\pm2,\ldots \tag{86}$$

Finally, the displacement $g(x)$ in terms of fringe order N is as follows:

$$g(x)=\frac{(0.5+N)\lambda}{\sin\theta} \tag{87}$$

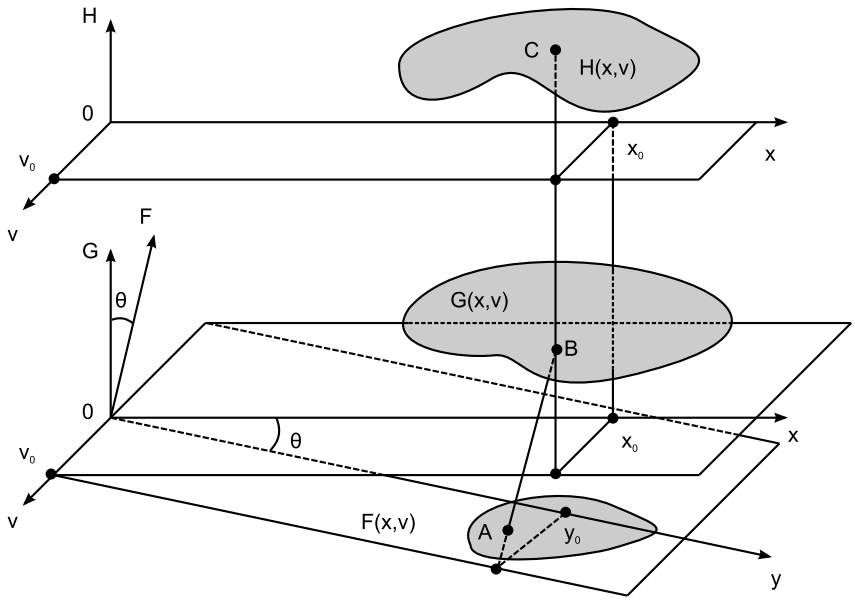

Figure 3.13: Schematic representation of the projection process.

The image plane, of the observation plane and the surface plane is located independently in the 3D space. As the angle of observation is assumed to be zero, the H-plane and the G-plane are parallel (Figure 3.13). The angle of illumination is θ. Thus, it is assumed (without the loss of generality) that the angle between the F-plane and the G-plane is also θ. As previously, the gray-scale levels of the projected image are determined by function $F(y, v)$, the shape of the surface as $G_K(x, v)$, the gray-scale levels of the observed image as $H_K(x, v)$. Then:

$$F(x, v) = \frac{1}{2} + \frac{1}{2}\cos\left(\frac{2\pi(x\cos\alpha - v\sin\alpha)}{\lambda}y\right) \tag{88}$$

$$H_K(x, v) = F(x\cos\theta - G(x, v)\sin\theta, v)\,\frac{\cos\theta + \frac{\partial G_K(x,v)}{\partial x}\sin\theta}{\sqrt{1 + \left(\frac{\partial G_K(x,v)}{\partial x}\right)^2}} \tag{89}$$

3.5.2. Experimental setup

Experimental setup for registration of artificial radial pulses and the result of experiment are provided in Figure 3.14 and Figure 3.15 respectively. The artificial artery is placed under a deformable layer of polyurethane of $2[mm]$ thickness and is covered by a thin deformable rubber membrane. Such a setup mimics human tissue and skin over an artery located near the surface of the skin. A radial pulse of the artificial artery generated by the non-uniform blood flow induces deformation of the artificial skin (and hypodermic layer). Such skin deformation can be measured by the

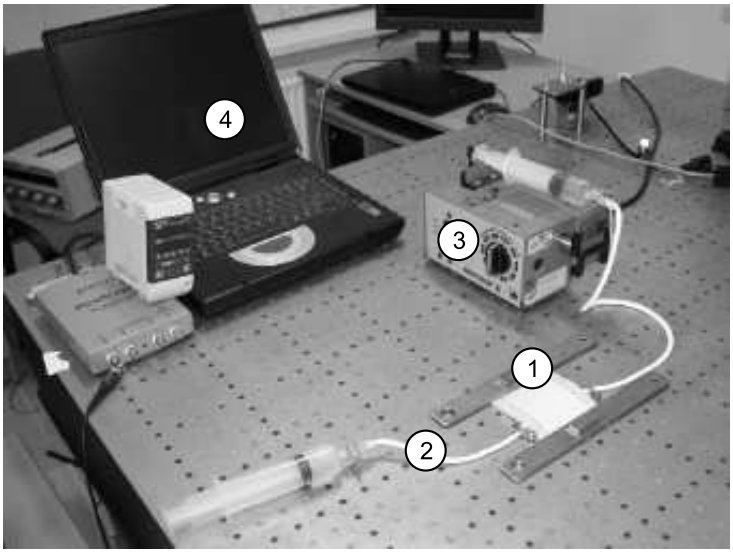

Figure 3.14: Experimental setup for registration of artificial radial pulses: (1) measurement location (test point); (2) vascular graft; (3) flow speed controller; (4) data registration and presentation.

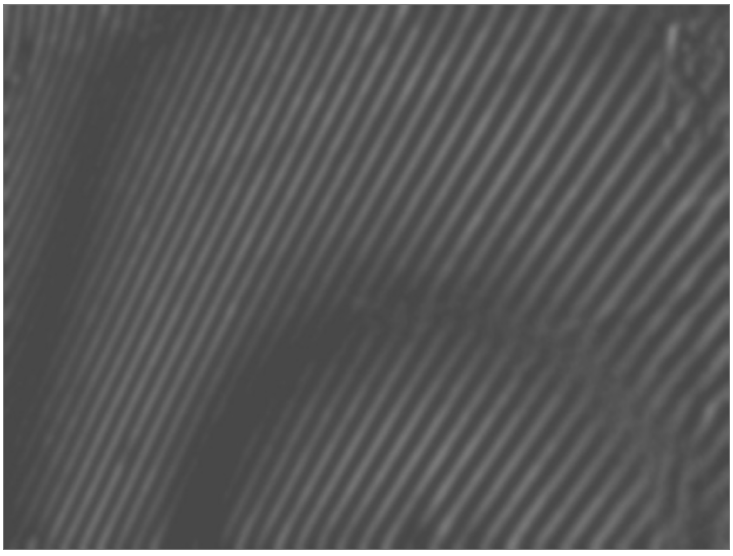

Figure 3.15: The experimental result of artificial radial blood flow pulsation by means of double-exposure whole-field projection moiré.

double-exposure whole-field projection moiré, when the surface of the artificial skin is illuminated at $45°$ and the camera continuously captures images of the projected grating.

3.6. Conclusions

A unified scheme for the identification of centerlines of interference fringes from optical experimental images is presented in this chapter. This scheme is partly based on standard algorithms of digital image processing. On the other hand, specific algorithmic implementation and original line tracing methods make this scheme robust to noise and various distortions in the original optical image.

The main objective of this chapter was to propose a reliable scheme for the construction of 2D map of fringe centerlines, since that in the main source of errors and uncertainties in the quantitative interpretation of fringe based optical experimental images. In other words, the reconstruction of 3D maps of the measured physical quantity (strain, amplitude of deformation, etc.) is not here, since it can be effectively done by using standard contour-based 3D plotting algorithms.

Robust identification of fringe centerlines is particularly important in shadow and projection moiré applications where it is common that poor illumination conditions, non-uniform distribution of moiré fringes in the observation area, complex surfaces of the investigated systems and noisy backgrounds do not allow a reliable interpretation of optical measurement results. Reliable identification of fringe centerlines is especially important in optical MEMS analysis.

4. VISUAL ENCRYPTION SCHEME BASED ON CGH AND DVC

A novel application of dynamic visual cryptography has been applied for mechanical vibration testing, where encoded cover image was fixed on the head of a vibration shaker system, and a human operator could detect the parameters of the vibration processes. To apply this technique for the investigation and testing of MEMS devices, and integration of computer generated holography and dynamic visual cryptography is proposed, that could enable monitoring of the parameters of MEMS elements.

4.1. Integration of DVC and CGH methods

A new image encryption scheme based on computer generated holography and time-averaging moiré is proposed in this Section. The proposed encryption scheme comprises the following steps:

(i) An image hiding technique based on optical time-averaged moiré is used to encrypt the secret image.

(ii) Encrypted data are used as the target image for Gerchberg-Saxton algorithm in order to obtain phase data.

(iii) Various fabrication techniques can now be used to fabricate DOE based on retrieved phase data.

The computational decryption is performed as follows:

(i) DOE is illuminated by a coherent laser beam in the virtual optical environment. The light distribution of the encrypted data is formed in the observation (or the reconstruction) plane.

(ii) Oscillation of DOE by a predefined amplitude allows to decrypt encrypted the image and to acquire the secret image.

A flow chart diagram describing the encryption and the decryption processes is illustrated in Figure 4.1.

4.2. Computational experiments

Results of computational experiments, that were implemented in Matlab R2012b environment, illustrating the proposed scheme are shown in Figure 4.3, Figure 4.4 and Figure 4.5 (the secret image is shown in Figure 4.2). Parts (a) and (b) in Figure 4.3 show the original encrypted image (the encryption is performed according to the algorithm presented in Section 1.5). Two computational experiments were performed with 1x1 composite pixel size in (a) and 3x3 composite pixel size in part (b) (note that the resolution of digital images in parts (a) and (b) are different). Corresponding phase data are given in Figure 4.4 parts (a) and (b). The resulting reconstructed image is given in Figure 4.4 parts (c) and (d). Figure 4.3 parts (c) and (d) illustrates the decryption step of a standard digital visual cryptography scheme. Figure 4.5 parts (a) and (b) show results

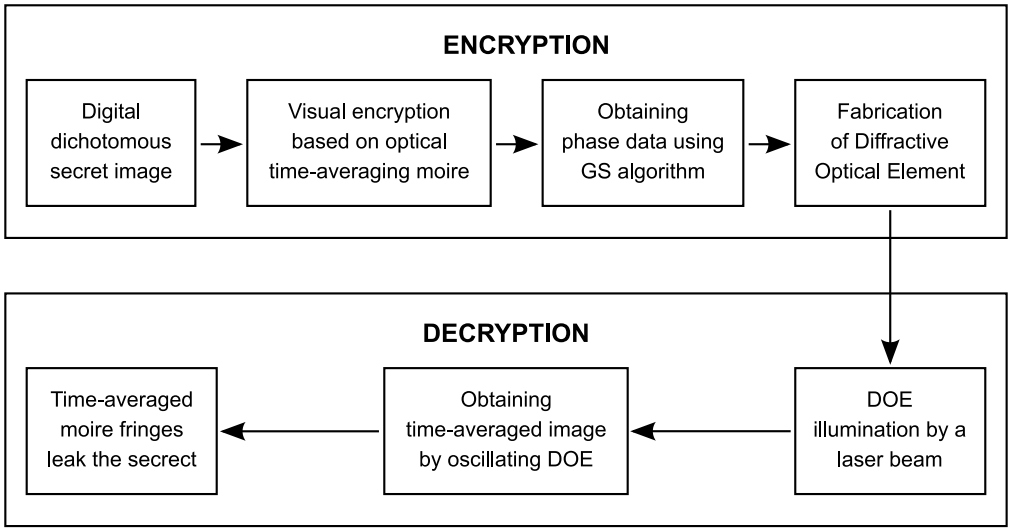

Figure 4.1: The encryption and decryption processes.

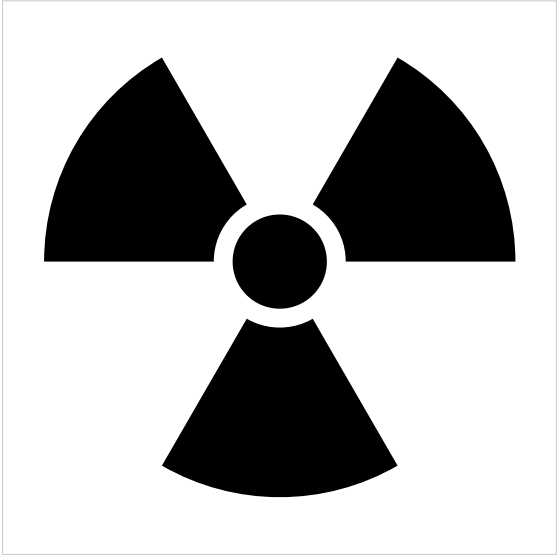

Figure 4.2: The secret image.

when Gerchberg-Saxton algorithm is applied to the encrypted image; parts (c) and (d) show the contrast enhanced images of (a) and (b). A technique based on (Ragulskis and Aleksa, 2009) can be used for the contrast enhancement.

The quality of the reconstructed secret images could be assessed using formal metrics. A PSNR type metrics is a common choice for the evaluation of the quality of the decryption algorithms (Au Yeung et al., 2010). However, a PSNR type metrics is not directly applicable for the proposed technique simply because the original secret digital image is a black and white image – and the reconstructed image is a grayscale image. The secret image is leaked in a pattern of time-averaged moiré fringes in a stochastic grayscale background. A direct pixel by pixel comparison between these two images is irrelevant.

The quality of the reconstruction of the secret image in our case could be evaluated by the ratio of the smoothness of areas occupied by time-averaged moiré fringes and the smoothness of the background (the smaller is this ratio, the better is visual interpretability of the decoded secret image). The standard deviation of the grayscale level around the mean grayscale level in a particular zone of the time-averaged image is introduced in (Ragulskis, Saunoriene, et al., 2009). Lets denote the quality parameter of the reconstruction of the time-averaged secret image Q as:

$$Q = \frac{\sigma\left(\overline{F_S}\right)}{\sigma\left(\overline{F_B}\right)} \tag{90}$$

where σ is the standard deviation of grayscale levels of pixels in a given area; $\overline{F_S}$ denotes the area of the digital image occupied by time-averaged moiré fringes (the secret) and $\overline{F_B}$ – the area occupied by the background. It is clear that $0 \leq Q \leq 1$. The secret image is clearly seen when $Q = 0$ (the secret image is revealed by ideal time-averaged moiré fringes), but it is not interpretable when $Q = 1$.

The computed values of the quality parameter Q for decrypted images are listed below: $Q = 0.2195$ for Figure 4.3 c); $Q = 0.2162$ for Figure 4.3 d); $Q = 0.6675$ for Figure 4.5 a); $Q = 0.5806$ for Figure 4.5 b); $Q = 0.5692$ for Figure 4.5 c) and $Q = 0.3464$ for Figure 4.5 d). It is clear from the results that 3x3 size of the composite pixel makes the algorithm less prone to noise, that is induced by Gerchberg-Saxton algorithm ($Q = 0.5692$ for 1x1 and $Q = 0.3464$ for 3x3 sizes of composite pixels). Note that Gerchberg-Saxton algorithm is not employed for 4.3 parts (a) and (b) – the additional noise is not added to the cover moiré grating and the resulting time-averaged moiré fringes are almost ideally smooth. But the decrypted secret image is well-interpretable by a naked eye even though the values of Q are much higher for parts (c–d).

As mentioned previously, Gerchberg-Saxton algorithm does introduce additional noise to the cover image. Therefore it is important to assess the sensitivity of the time-averaged image to the noise and occlusion contaminations to the encrypted cover image. Thus, a computational experiment is performed by adding a random noise to the digital cover image illustrated in Figure 4.3 (b).

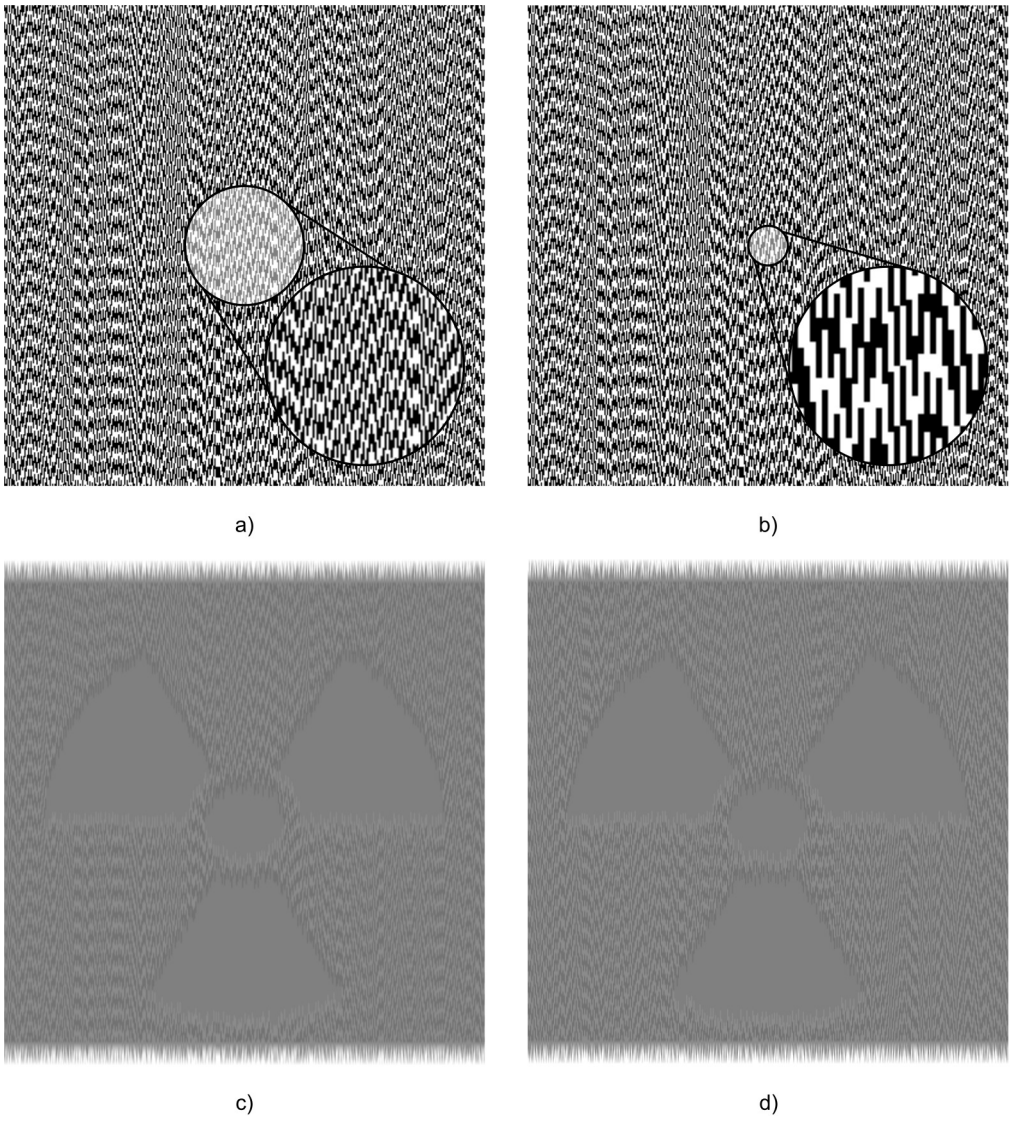

Figure 4.3: Computational results of digital visual cryptography scheme. The encrypted image with different composite pixel sizes is shown in parts a) and b); The decryption results are shown in parts c) and d).

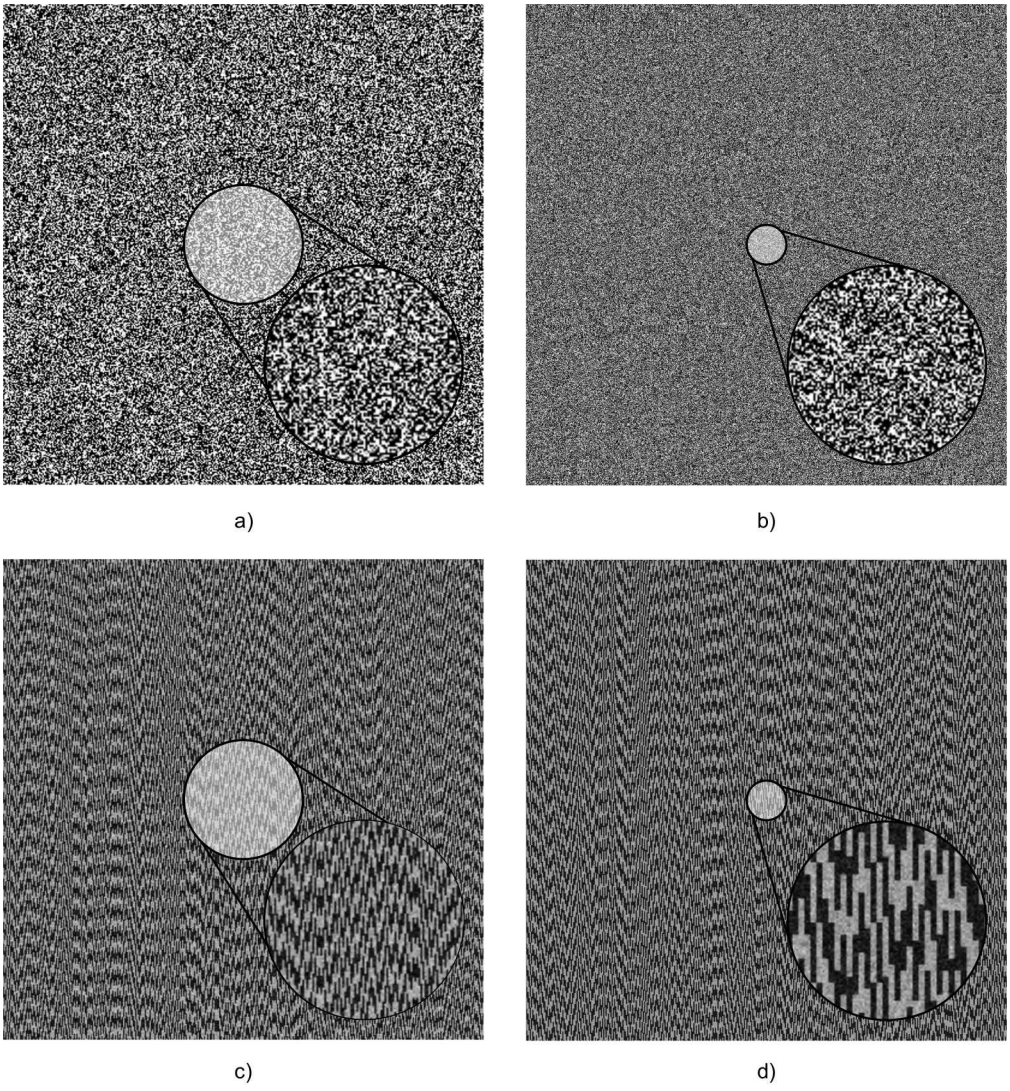

Figure 4.4: Computational results for the proposed scheme – the encryption step. Phase data acquired by Gerchberg-Saxton algorithm is shown in parts a) and b); the reconstructed image is shown in parts c) and d).

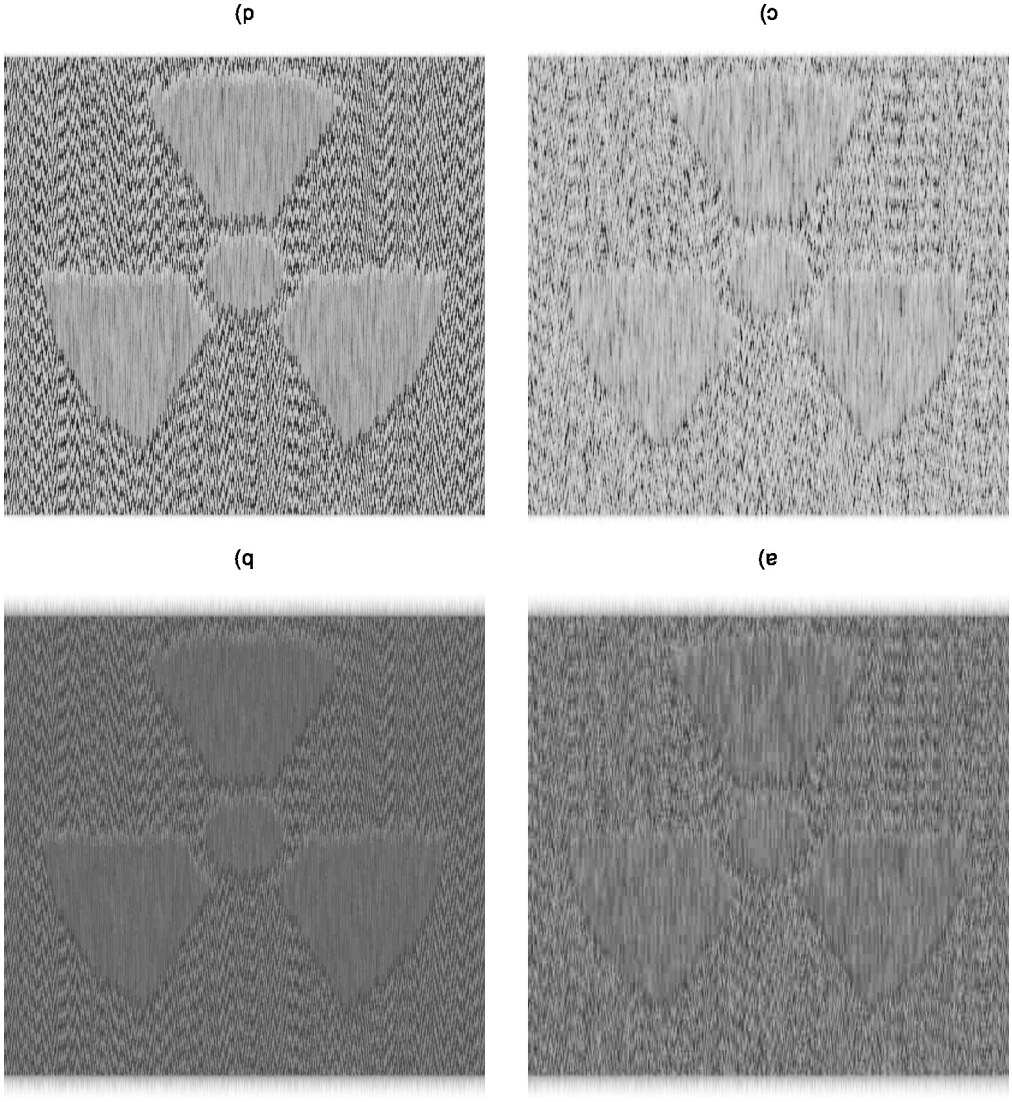

Figure 4.5: Computational results for the proposed scheme – the decryption step. The results with Gerchberg-Saxton algorithm are shown in parts a) and b); contrast enhanced images are illustrated in parts c) and d).

Figure 4.6 (a) shows the encrypted cover image with added noise uniformly distributed in interval $[-0.1, 0.1]$. Note that 256 grayscale discrete levels are used (0 stands for the black color; 1 – for the white color). Each pixel of the cover image is affected by the additive noise; the pixel level is rounded to the nearest discrete grayscale level (the pixel level is set to 0 if the altered grayscale level is lower than 0; analogously the pixel level is set to 1 if the altered level is higher than 1). The time-averaged image of Figure 4.6 (a) is shown in Figure 4.6 (c).

Computational experiments are repeated with the random noise uniformly distributed in interval $[-0.2, 0.2]$; the cover image is shown in Figure 4.6 (b) and the time-averaged image – in Figure 4.6 (d). A naked eye confirms that the proposed optical encryption scheme is robust to noise contamination. Nevertheless, the parameter of the quality of reconstruction Q for Figure 4.6 (c) ($Q = 0.2898$) and Figure 4.6 (d) ($Q = 0.3933$) are computed. That confirms the robustness of the system to the additive noise (the value of Q for Figure 4.3 c) is $Q = 0.2195$). Another method to evaluate noise influence to decrypted image is PSNR (peak signal-to-noise ratio) (Huynh-Thu et al., 2008), which is defined as:

$$\text{PSNR} = 10 \cdot \log_{10} \left(\frac{MAX_I^2}{\frac{1}{mn} \sum_{i=0}^{m-1} \sum_{j=0}^{n-1} \left[I\left(i,j\right) - K\left(i,j\right) \right]^2} \right) \tag{91}$$

where I is original image; K is image contaminated with noise; MAX_I is the maximum possible value of the image. It allows to find the ratio between the power of corrupting noise, that affects the quality of its representation, and the maximum possible power of a signal . In case the two images are identical, a value of PSNR tends to infinity. PSNR values were computed for Figures 4.3 c) - 4.6 c) and Figures 4.3 d) - 4.6 d). The values are respectively PSNR $= +40.95dB$ and PSNR $= +36.21dB$, which indicates also indicates that this method is robust to noise contamination.

4.3. Experimental applications

Note that the illustrated optical decryption scheme is implemented in a virtual optical environment. Physical realization of the decryption requires an experimental implementation of the DOE on a surface of an oscillating structure. That enables interesting potential of the proposed optical technique for image hiding and optical monitoring applications. The proposed technique can be exploited for vibration monitoring of the whole experimental setup when the reconstructed image performs oscillations around the state of equilibrium in the observation plane. Alternatively the proposed technique can be exploited for visual monitoring of the vibrations of micro-components carrying the DOE. However, in the later case the visual encoding scheme must account deformations happening in the cover image itself – the image hiding technique based on deformable moiré gratings (Palivonaite et al., 2014) must be used then. In any case, the main objective of this chapter is to propose the fusion of dynamic visual cryptography and computer generated holography. All experimental results presented in this

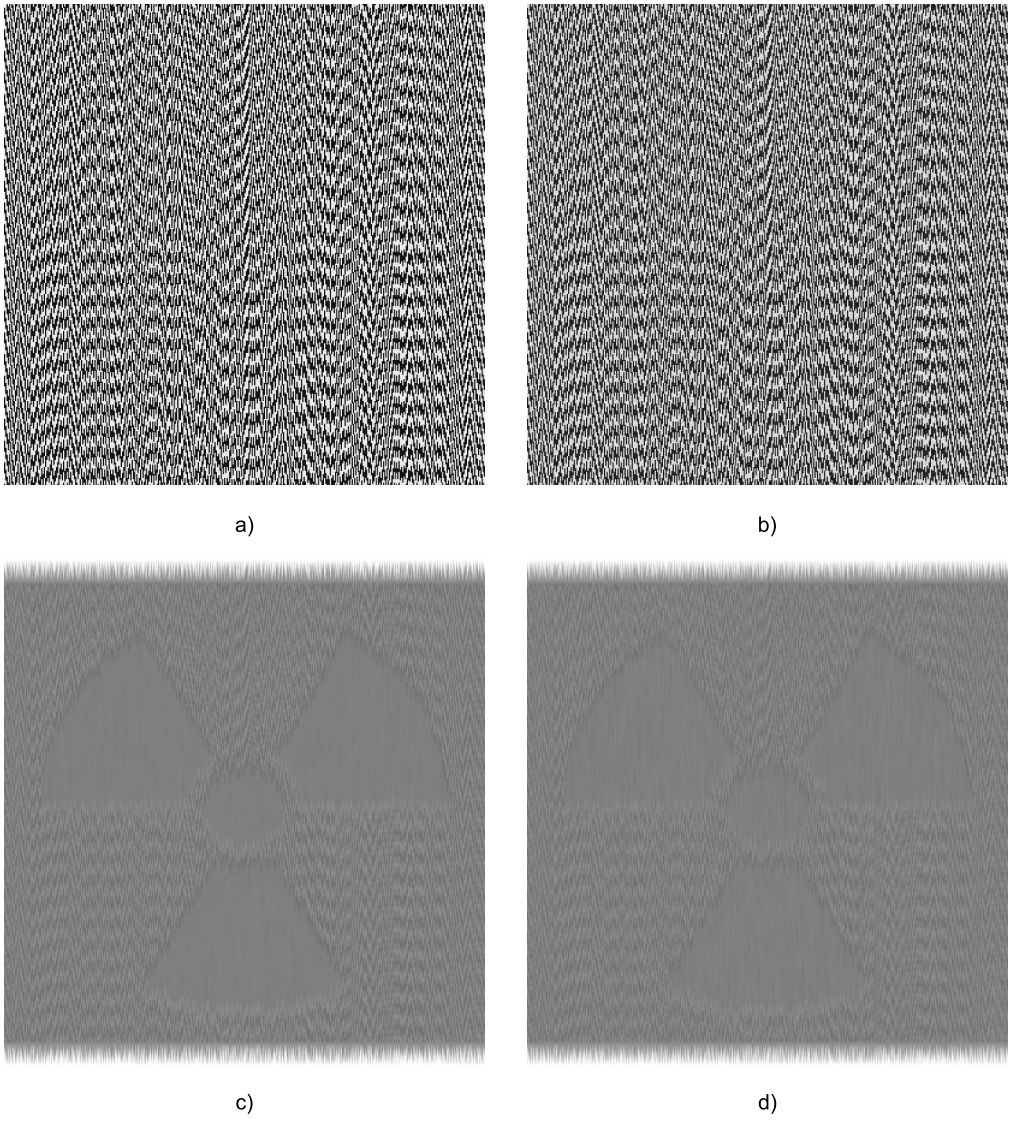

Figure 4.6: The robustness of the proposed scheme to the additive noise: the encrypted cover with the added noise uniformly distributed in interval $[-0.1, 0.1]$ is shown in a); with the noise distributed in interval $[-0.2, 0.2]$ – in b). The decrypted images of a) and b) are shown respectively in c) and d).

chapter are performed in virtual optical environment.

4.4. Conclusions

An image hiding scheme based on computer generated holography and dynamic visual cryptography is proposed in this chapter. The secret image is embedded into the stochastic geometric moiré cover image. Gerchberg-Saxton algorithm is used to produce phase data from the encrypted cover image and is directly incorporated into CGH. The secret image is leaked from time-averaged pattern of fringes generated by an oscillating CGH image in the projection plane; the decryption is completely optical and does not require an application of a computing device. Moreover, the secret image is not shared into components – the secret is embedded into a single stochastic cover image which is directly used as a target image for the Gerchberg-Saxton algorithm. So far, only the applicability of this technique in virtual optical environments was demonstrated though the proposed technique has high potential in experimental applications (especially for optical monitoring of movable components of MEMS).

5. CONCLUSIONS

1. The performed literature analysis suggested an investigation of time-averaged holography method application for MEMS analysis. It also shows, that a fringe interpretation techniques are crucial for MEMS development thus reliable fringe centerline interpretation is needed. Finally, application of the dynamic visual cryptography for mechanical vibration testing, indicated high potential for adaptation of this technique for MEMS analysis, by integrating it with the computer generated holography.

2. It was demonstrated that complex, chaotic motions can be generated even in rather simple microelectromechanical systems. A model of fixed-fixed beam was created to demonstrate generation of time-averaged fringes. Three computational simulations were performed ($V_{DC} = 40V$, $V_{DC} = 38V$ and $V_{AC} = 2V$, $V_{DC} = 35V$ and $V_{AC} = 5V$). A decay of intensity was observed when the system was performing nonlinear oscillations. Therefore, a straightforward interpretation of time-averaged holographic interferograms of micro-mechanical components can be not only be misguiding but the experimental holographic images may not reveal any interpretable fringes at all. The derived analytical results yield a deeper insight into the dynamical properties of MEMS components.

3. A reliable scheme is proposed for the construction of 2D map of fringe centerlines, since that is the main source of errors and uncertainties in the quantitative interpretation of fringe based optical images in optical MEMS analysis. The developed algorithmic implementation and original line tracing methods make this scheme robust to noise and various distortions in the original optical image.

4. An image hiding scheme based on computer generated holography and dynamic visual cryptography is proposed. The secret image is embedded into the stochastic geometric moiré cover image. Gerchberg-Saxton algorithm is used to produce phase data from the encrypted cover image and is directly incorporated into CGH and can be effectively applied for optical monitoring of MEMS components. The reliability of the technique was assessed, which indicated Q values ranging from $Q = 0.2195$ (for standard dynamic visual cryptography technique) to $Q = 0.5806$ (for integrated method). This indicates a quality loss due to noise, though a result is still interpretable. $PSNR$ values between the decrypted image and decrypted images with added noise are $PSNR = +40.95dB$ and $PSNR = +36.21dB$

REFERENCES

1. Abdelsalam, D. et al. Highly accurate film thickness measurement based on automatic fringe analysis. *Optik - International Journal for Light and Electron Optics*. 2012, 123(16), 1444–1449. ISSN: 00304026.
2. Al Na'mneh, R. A. et al. An efficient bit reversal permutation algorithm. *Robotics, Biomimetics, and Intelligent Computational Systems (ROBIONETICS)*. 2013. 121–124.
3. Al Na'mneh, R. et al. Five-step FFT algorithm with reduced computational complexity. *Information Processing Letters*. 2007, 101(6), 262–267. ISSN: 00200190.
4. Anand, A. Tracing of interference fringes using average gray value and simultaneous row and column scan. *Optics & Laser Technology*. 2003, 35(2), 73–79. ISSN: 00303992.
5. Asundi, A. Computer Aided Moiré Methods. *Optics and Lasers in Engineering*. 1993, 18(3), 213–238. ISSN: 01438166.
6. Asundi, A. *Digital holography for MEMS and microsystem metrology*. Chichester, West Sussex, U.K. ; Hoboken, N.J:Wiley. 2011. ISBN: 9780470978696.
7. Au Yeung, S.-K. et al. Quality assessment for a perceptual video encryption system. *2010 IEEE International Conference on Wireless Communications, Networking and Information Security*. 2010,
8. Banon, G. *Mathematical morphology and its applications to signal and image processing: 11th International Symposium, ISMM 2013, Uppsala, Sweden, May 27-29, 2013. Proceedings*. 1st edition. New York:Springer. Lecture notes in computer science, 2013. ISBN: 9783642382932.
9. Bao, M. et al. Squeeze film air damping in MEMS. *Sensors and Actuators A: Physical*. 2007, 136(1), 3–27. ISSN: 09244247.
10. Breque, C. et al. Calibration of a system of projection moiré for relief measuring: biomechanical applications. *Optics and Lasers in Engineering*. 2004, 41(2), 241–260. ISSN: 01438166.
11. Bustillo, J. et al. Surface micromachining for microelectromechanical systems. *Proceedings of the IEEE*. 1998, 86(8), 1552–1574. ISSN: 00189219.
12. Chen, Y.-C. et al. A new authentication based cheating prevention scheme in Naor-Shamir's visual cryptography. *Journal of Visual Communication and Image Representation*. 2012, 23(8), 1225–1233. ISSN: 1047-3203.
13. Chen, W. and X. Chen. Optical multiple-image authentication based on modified Gerchberg-Saxton algorithm with random sampling. *Optics Communications*. 2014, 318, 128–132. ISSN: 0030-4018.
14. Chen, W., X. Chen, et al. Phase-Modulated Optical System With Sparse Representation for Information Encoding and Authentication. *IEEE Photonics Journal*. 2013, 5(2), 6900113. ISSN: 1943-0655.
15. Chiu, P.-L. et al. User-friendly threshold visual cryptography with complementary cover images. *Signal Processing*. 2015, 108, 476–488. ISSN: 01651684.
16. Comtois, J. et al. Surface-micromachined polysilicon MOEMS for adaptive optics. *Sensors and Actuators A: Physical*. 1999, 78(1), 54–62. ISSN: 09244247.
17. De Pasquale, G. Experimental analysis of viscous and material damping in microstructures through the interferometric microscopy technique with climatic chamber. *Journal of Sound and Vibration*. 2013, 332(18), 4103–4121. ISSN: 0022460X.

18. Du, H. et al. Calibration of the high sensitivity shadow moiré system using random phase-shifting technique. *Optics and Lasers in Engineering*. 2014, 63, 70–75. ISSN: 01438166.
19. Duda, R. O. et al. Use of the Hough transformation to detect lines and curves in pictures. *Communications of the ACM*. 1972, 15(1), 11–15. ISSN: 00010782.
20. Dufresne, E. R. et al. Computer-generated holographic optical tweezer arrays. *Review of Scientific Instruments*. 2001, 72(3), 1810. ISSN: 0034-6748.
21. Gao, F. et al. Electron-beam lithography to improve quality of computer-generated hologram. *Microelectronic Engineering*. 2002, 61-62, 363–369. ISSN: 0167-9317.
22. Geng, P. et al. Application of Shadow Moiré Technique to Board Level Manufacturing Technologies. *Electronic Components and Technology Conference*. 2006. 1816–1820. ISBN: 1-4244-0152-6.
23. Gerchberg, R. W. et al. A practical algorithm for the determination of the phase from image and diffraction plane pictures. *Optik*. 1972, 35, 237–246.
24. Ghayesh, M. H. et al. Nonlinear behaviour of electrically actuated MEMS resonators. *International Journal of Engineering Science*. 2013, 71, 137–155. ISSN: 00207225.
25. Gonzalez, R. C. *Digital image processing*. 3rd ed. Upper Saddle River, N.J:Prentice Hall. 2008. ISBN: 9780131687288.
26. Guan, T. et al. MOEMS uniaxial accelerometer based on EpoClad/EpoCore photoresists with built-in fiber clamp. *Sensors and Actuators A: Physical*. 2013, 193, 95–102. ISSN: 09244247.
27. Guo, Y. et al. Robust phase unwrapping algorithm based on least squares. *Optics and Lasers in Engineering*. 2014, 63, 25–29. ISSN: 01438166.
28. Haghighi, H. S. et al. Chaos prediction and control in MEMS resonators. *Communications in Nonlinear Science and Numerical Simulation*. 2010, 15(10), 3091–3099. ISSN: 10075704.
29. Han, B. Recent advancements of moiré and microscopic moiré interferometry for thermal deformation analyses of microelectronics devices. *Experimental Mechanics*. 1998, 38(4), 278–288. ISSN: 0014-4851, 1741-2765.
30. Hariharan, P. *Basics of interferometry*. 2nd ed. Amsterdam ; Boston:Elsevier Academic Press. 2007. ISBN: 0123735890.
31. Hayman, G. et al. Holographic PRISMA System for Investigation of Mechatronic Systems. 2006, Kaunas:Technologija. 27–29.
32. He, Y. et al. Deformation and profile measurement using the digital projection grating method. *Optics and Lasers in Engineering*. 1998, 30(5), 367–377. ISSN: 01438166.
33. Hou, Y.-C. Visual cryptography for color images. *Pattern Recognition*. 2003, 36(7), 1619–1629. ISSN: 0031-3203.
34. Huo, J. et al. A technique of phase-shifting for 3-D measurement using spectral-transform. *Optics and Lasers in Engineering*. 2013, 51(10), 1133–1137. ISSN: 01438166.
35. Huynh-Thu, Q. et al. Scope of validity of PSNR in image/video quality assessment. *Electronics Letters*. 2008, 44(13), 800. ISSN: 00135194.
36. Iannacci, J. Reliability of MEMS: A perspective on failure mechanisms, improvement solutions and best practices at development level. *Displays*. 2015, 37, 62–71. ISSN: 01419382.

37. Iannacci, J. et al. Enhancement of RF-MEMS switch reliability through an active anti-stiction heat-based mechanism. *Microelectronics Reliability*. 2010, 50(9-11), 1599–1603. ISSN: 00262714.

38. Jia, X. et al. Resonance frequency response of geometrically nonlinear micro-switches under electrical actuation. *Journal of Sound and Vibration*. 2012, 331(14), 3397–3411. ISSN: 0022460X.

39. Kim, S.-W. et al. Reverse engineering: high speed digitization of free-form surfaces by phase-shifting grating projection moiré topography. *International Journal of Machine Tools and Manufacture*. 1999, 39(3), 389–401. ISSN: 08906955.

40. Kley, E.-B. et al. Fabrication and properties of refractive micro-optical beam-shaping elements. *Micromachine Technology for Diffractive and Holographic Optics*. 1999,

41. Kobayashi, A. S. et al. *Handbook on experimental mechanics*. New York, N.Y.; Bethel, CT, USA:VCH. 1993. ISBN: 1560816406 9781560816409 3527896406 9783527896400.

42. Koev, S. T. et al. Interferometric readout of multiple cantilever sensors in liquid samples. *Sensors and Actuators B: Chemical*. 2010, 146(1), 245–252. ISSN: 09254005.

43. Kovacs, G. et al. Bulk micromachining of silicon. *Proceedings of the IEEE*. 1998, 86(8), 1536–1551. ISSN: 00189219.

44. Krishna Mohan, N. et al. Recent developments in interferometry for microsystems metrology. *Optics and Lasers in Engineering*. 2009, 47(2), 199–202. ISSN: 01438166.

45. Krupa, K. et al. Interferometric study of reliability of microcantilevers driven by AlN sandwiched between two metal layers. *Sensors and Actuators A: Physical*. 2011, 171(2), 306–316. ISSN: 09244247.

46. Kujawinska, M. Modern optical measurement station for micro-materials and micro-elements studies. *Sensors and Actuators A: Physical*. 2002, 99(1-2), 144–153. ISSN: 09244247.

47. Lehmann, M. et al. Shape measurements on large surfaces by fringe projection. *Experimental Techniques*. 1999, 23(2), 31–35. ISSN: 0732-8818, 1747-1567.

48. Li, J. et al. Compressive optical image encryption with two-step-only quadrature phase-shifting digital holography. *Optics Communications*. 2015, 344, 166–171. ISSN: 00304018.

49. Li, Y. et al. Phase unwrapping method based on multiple recording distances for digital holographic microscopy. *Optics Communications*. 2015, 346, 38–42. ISSN: 00304018.

50. Liang, C. et al. Time-averaged moire method for in-plane vibrational analysis. *Journal of Sound and Vibration*. 1979, 62(2), 267–275. ISSN: 0022-460X.

51. Lim, J. et al. Determination of Young's modulus of epoxy coated polyethylene micro-cantilever using phase-shift shadow moiré method. *Optics and Lasers in Engineering*. 2011, 49(11), 1301–1308. ISSN: 01438166.

52. Lin, W. et al. Bifurcations and chaos in a forced cantilever system with impacts. *Journal of Sound and Vibration*. 2006, 296(4-5), 1068–1078. ISSN: 0022460X.

53. Liu, J. et al. Optical color image encryption based on computer generated hologram and chaotic theory. *Optics Communications*. 2013, 307, 76–79. ISSN: 0030-4018.

54. Liu, Z. et al. Deformation analysis of MEMS structures by modified digital moiré methods. *Optics and Lasers in Engineering*. 2010, 48(11), 1067–1075. ISSN: 01438166.

55. Lu, X. et al. 3D profile reconstruction of biological sample by in-line image-plane phase-shifting digital microscopic holography. *Optics and Lasers in Engineering*. 2012, 50(10), 1431–1435. ISSN: 01438166.

56. Luo, H. et al. Color transfer in visual cryptography. *Measurement*. 2014, 51, 81–90. ISSN: 02632241.

57. Mamilla, V. R. et al. Micro Machining for Micro Electro Mechanical Systems (MEMS). *Procedia Materials Science*. 2014, 6, 1170–1177. ISSN: 22118128.

58. Meadows, D. M. et al. Generation of Surface Contours by Moiré Patterns. *Applied Optics*. 1970, 9(4), 942. ISSN: 0003-6935, 1539-4522.

59. Miranda, M. et al. Monte Carlo based techniques of two-stage phase shifting algorithms. *Optics and Lasers in Engineering*. 2011, 49(3), 439–444. ISSN: 01438166.

60. Moo-Young, M. *Comprehensive biotechnology*. Amsterdam; Boston:Elsevier. 2011. ISBN: 9780080885049 0080885047.

61. Naor, M. et al. Visual Cryptography. *Lecture Notes in Computer Science*. 1995. 1–12.

62. Nibouche, O. et al. Algorithms and pipeline architectures for 2-D FFT and FFT-like transforms. *Digital Signal Processing*. 2010, 20(4), 1072–1086. ISSN: 10512004.

63. Ostasevicius, V. et al. Synergy of contact and noncontact techniques for design and characterization of vibrating MOEMS elements. *Journal of Micro/Nanolithography, MEMS, and MOEMS*. 2005, 4(4), 041602. ISSN: 1932-5150.

64. Ou, D. et al. Non-expansible XOR-based visual cryptography scheme with meaningful shares. *Signal Processing*. 2015, 108, 604–621. ISSN: 01651684.

65. Palivonaite, R. et al. Image hiding in time-averaged deformable moire gratings. *J. Opt.* 2014, 16(2), 025401. ISSN: 2040-8986.

66. Parthiban, V. et al. Interactive Fringe processing algorithm for interferogram analysis. *Optics and Lasers in Engineering*. 1989, 11(2), 103–113. ISSN: 01438166.

67. Paul Kumar, U. et al. Measurement of static and vibrating microsystems using microscopicTV holography. *Optik - International Journal for Light and Electron Optics*. 2011, 122(1), 49–54. ISSN: 00304026.

68. Pedrini, G. et al. Measurement of in-plane deformations of microsystems by digital holography and speckle interferometry. *Chinese Optics Letters*. 2009, 7(12), 1109–1112.

69. Petrauskiene, V., A. Aleksa, et al. Dynamic visual cryptography for optical control of vibration generation equipment. *Optics and Lasers in Engineering*. 2012, 50(6), 869–876. ISSN: 01438166.

70. Petrauskiene, V., R. Palivonaite, et al. Dynamic visual cryptography based on chaotic oscillations. *Communications in Nonlinear Science and Numerical Simulation*. 2014, 19(1), 112–120. ISSN: 1007-5704.

71. Pourvais, Y. et al. Experimental and finite element analysis of higher order behaviour of sandwich beams using digital projection moiré. *Polymer Testing*. 2014, 38, 7–17. ISSN: 01429418.

72. Quentel, F. et al. Multilevel diffractive optical element manufacture by excimer laser ablation and halftone masks. *Laser Applications in Microelectronic and Optoelectronic Manufacturing VI*. 2001,

73. Radon, J. Über die Bestimmung von Funktionen durch ihre Integralwerte längs gewisser Mannigfaltigkeiten. *Akad. Wiss.* 1917, 69, 262–277.

74. Rafiee, P. et al. A fast reliability assessment method for Si MEMS based microcantilever beams. *Microelectronics Reliability*. 2014, 54(9-10), 2180–2184. ISSN: 00262714.

75. Ragulskis, M. and Z. Navickas. Time Average Geometric Moire-Back to the Basics. *Experimental Mechanics*. 2009, 49(4), 439–450. ISSN: 1741-2765.

76. Ragulskis, M., A. Palevicius, et al. Plotting holographic interferograms for visualization of dynamic results from finite-element calculations. *International Journal for Numerical Methods in Engineering*. 2003, 56(11), 1647–1659. ISSN: 0029-5981, 1097-0207.

77. Ragulskis, M., L. Saunoriene, et al. The Sructure of Moire Grating Lines and its Influence to the Time-Averaged Fringes. *Experimental Techniques*. 2009, 33(2), 60–64. ISSN: 1747-1567.

78. Ragulskis, M. and A. Aleksa. Image hiding based on time-averaging moire. *Optics Communications*. 2009, 282(14), 2752–2759. ISSN: 0030-4018.

79. Rai-Choudhury, P., ed. *MEMS and MOEMS technology and applications*. Bellingham, Wash:SPIE Optical Engineering Press. 2000. ISBN: 0819437166.

80. Ryu, W.-J. et al. A study on the 3-D measurement by using digital projection moiré method. *Optik - International Journal for Light and Electron Optics*. 2008, 119(10), 453–458. ISSN: 00304026.

81. Salbut, L. et al. Interferometric methods for static and dynamic characterizations of micromembranes for sensing functions. Gorecki, C. et al., eds. 2004. 16–24.

82. Sankur, B. Survey over image thresholding techniques and quantitative performance evaluation. *Journal of Electronic Imaging*. 2004, 13(1), 146. ISSN: 1017-9909.

83. Schilling, A. et al. Efficient Beam Shaping of Linear, High-Power Diode Lasers by Use of Micro-Optics. *Appl. Opt.* 2001, 40(32), 5852. ISSN: 1539-4522.

84. Sciammarella, C. A. et al. Strain measurements in the nanometer range in a particulate composite using computer-aided moiré. *Experimental Mechanics*. 2003, 43(3), 341–347. ISSN: 0014-4851, 1741-2765.

85. Seebacher, S. et al. The determination of material parameters of microcomponents using digital holography. *Optics and Lasers in Engineering*. 2001, 36(2), 103–126. ISSN: 01438166.

86. Shang, H. et al. Thermal Properties Measurement of Micro-electromechanical System Sensors by Digital Moiré Method. *Strain*. 2005, 41(4), 157–162. ISSN: 00392103, 14751305.

87. Sharpe, J. et al., eds. *Springer handbook of experimental solid mechanics*. Berlin:Springer. 2008. ISBN: 0387268839 9780387268835.

88. Shea, D. *Diffractive optics : design, fabrication, and test*. Bellingham, Wash:SPIE Press. 2004. ISBN: 9780819451712.

89. Shoji, E. et al. Development of quasi common path phase-shifting interferometer for measurement of natural convection fields. *International Journal of Heat and Mass Transfer*. 2012, 55(25-26), 7460–7470. ISSN: 00179310.

90. Siewe, M. S. et al. Homoclinic bifurcation and chaos control in MEMS resonators. *Applied Mathematical Modelling*. 2011, 35(12), 5533–5552. ISSN: 0307904X.

91. Singh, V. R., G. Hedge, et al. Digital in-line holography for dynamic micrometrology. *Optical Micro- and Nanometrology in Microsystems Technology*. Gorecki, C. et al., eds. 2006.

92. Singh, V. R., J. Miao, et al. Dynamic characterization of MEMS diaphragm using time averaged in-line digital holography. *Optics Communications*. 2007, 280(2), 285–290. ISSN: 00304018.

93. Smith, D. C. Testing Diamond Turned Aspheric Optics Using Computer-Generated Holographic (CGH) Interferometry. *Contemporary Methods of Optical Fabrication*. 1982,

94. Steward, E. G. *Fourier optics: an introduction (second edition)*. Mineola, N.Y:Dover Publications. 2004. ISBN: 0486435040.

95. Suleski, T. J. et al. Fabrication of high-spatial-frequency gratings through computer-generated near-field holography. *Optics Letters*. 1999, 24(9), 602. ISSN: 1539-4794.

96. Takasaki, H. Moiré Topography. *Applied Optics*. 1970, 9(6), 1467. ISSN: 0003-6935, 1539-4522.

97. Teijido, J. M. et al. Manufacturing computer-generated holograms (CGH) by electron-beam. *Microelectronic Engineering*. 1989, 9(1-4), 255–257. ISSN: 0167-9317.

98. Turunen, J. *Diffractive optics for industrial and commercial applications*. Berlin:Akademie Verlag. 1997. ISBN: 3055017331.

99. Valamanesh, M. et al. Combining moiré patterns and high resolution transmission electron microscopy for in-plane thin films thickness determination. *Ultramicroscopy*. 2011, 111(2), 149–154. ISSN: 03043991.

100. Van Paepegem, W. et al. Use of projection moiré for measuring the instantaneous out-of-plane deflections of composite plates subject to bird strike. *Optics and Lasers in Engineering*. 2008, 46(7), 527–534. ISSN: 01438166.

101. Vest, C. M. *Holographic interferometry*. New York:Wiley. Wiley series in pure and applied optics, 1979. ISBN: 0471906832.

102. Wagemann, E. et al. Fast shape and position control by Moiré-filtering and object-adapted fringe projection. *Optics Communications*. 1999, 165(1-3), 7–10. ISSN: 00304018.

103. Wang, Q. et al. Investigation on LIGA-like process based on multilevel imprint lithography. *Microelectronics Journal*. 2009, 40(1), 149–155. ISSN: 00262692.

104. Wang, Y.-Y. et al. Optical image encryption based on binary Fourier transform computer-generated hologram and pixel scrambling technology. *Optics and Lasers in Engineering*. 2007, 45(7), 761–765. ISSN: 0143-8166.

105. Wise, K. D. Integrated sensors, MEMS, and microsystems: Reflections on a fantastic voyage. *Sensors and Actuators A: Physical*. 2007, 136(1), 39–50. ISSN: 09244247.

106. Xie, H. et al. Phase shifting SEM moiré method. *Optics & Laser Technology*. 2004, 36(4), 291–297. ISSN: 00303992.

107. Xu, L. et al. A new curve detection method: Randomized Hough transform (RHT). *Pattern Recognition Letters*. 1990, 11(5), 331–338. ISSN: 01678655.

108. Yan, X. et al. Generalized random grids-based threshold visual cryptography with meaningful shares. *Signal Processing*. 2015, 109, 317–333. ISSN: 01651684.

109. Yan, X. et al. Halftone visual cryptography with minimum auxiliary black pixels and uniform image quality. *Digital Signal Processing*. 2015, 38, 53–65. ISSN: 10512004.

110. Yang, C.-N. et al. Colored visual cryptography scheme based on additive color mixing. *Pattern Recognition*. 2008, 41(10), 3114–3129. ISSN: 00313203.

111. Yang, L. et al. Stroboscopic digital speckle pattern interferometry for vibration analysis of microsystem. *Optics and Lasers in Engineering*. 2009, 47(2), 252–258. ISSN: 01438166.

112. Yang, S. Y. et al. Chip warpage model for reliability prediction of delamination failures. *Microelectronics Reliability*. 2012, 52(4), 718–724. ISSN: 00262714.

113. Yen, K. et al. Comparison of in-plane displacement measurement from circular grating moiré fringes using Fourier transformation and graphical analysis. *Optics and Lasers in Engineering*. 2012, 50(5), 687–702. ISSN: 01438166.

114. Zaal, J. et al. Packaging influences on the reliability of MEMS resonators. *Microelectronics Reliability*. 2008, 48(8-9), 1567–1571. ISSN: 00262714.

115. Zhang, S. Composite phase-shifting algorithm for absolute phase measurement. *Optics and Lasers in Engineering*. 2012, 50(11), 1538–1541. ISSN: 01438166.

116. Zhang, W.-M. et al. Noise-induced chaos in the electrostatically actuated MEMS resonators. *Physics Letters A*. 2011, 375(32), 2903–2910. ISSN: 03759601.

117. Zhou, Y. et al. Fast Fourier transform using matrix decomposition. *Information Sciences*. 2015, 291, 172–183. ISSN: 00200255.

LIST OF AUTHOR'S PUBLICATIONS

Papers in Master List Journals of the Institute of Scientific Information (ISI):

1. Palevičius, Paulius; Sudintas, Antanas Rimantas; Fedaravičius, Algimantas; Ragulskienė, Jūratė. A robust scheme for the identification of centerlines of moiré fringes from optical experimental images // Journal of Vibroengineering / Vibromechanika, Lithuanian Academy of Sciences, Kaunas University of Technology, Vilnius Gediminas Technical University. Vilnius : Vibromechanika. ISSN 1392-8716. 2012, Vol. 14, iss. 4, p. 1807-1814. [Science Citation Index Expanded (Web of Science); Academic Search Complete; Central & Eastern European Academic Source; Computers & Applied Sciences Complete; Current Abstracts; INSPEC; TOC Premier]. [0,250]. [IF (E): 0,452 (2012)]

2. Malinauskas, Karolis; Palevičius, Paulius; Ragulskis, Minvydas; Ostaševičius, Vytautas; Daukševičius, Rolanas. Validation of noninvasive MOEMS-assisted measurement system based on CCD sensor for radial pulse analysis // Sensors. Basel : Molecular Diversity Preservation International, MDPI. ISSN 1424-8220. 2013, vol. 13, iss. 4, p. 5368-5380. DOI: 10.3390/s130405368. [Science Citation Index Expanded (Web of Science); Academic Search Complete]. [0,200]. [IF (E): 2,048 (2013)]

3. Palevičius, Paulius; Ragulskis, Minvydas; Palevičius, Arvydas; Ostaševičius, Vytautas. Applicability of time-averaged holography for micro-electro-mechanical system performing non-linear oscillations // Sensors. Basel : Molecular Diversity Preservation International-MDPI. ISSN 1424-8220. 2014, Vol. 14, iss. 1, p. 1805-1821. DOI: 10.3390/s140101805. [Science Citation Index Expanded (Web of Science); Academic Search Complete]. [0,250]. [IF (E): 2,048 (2013)]

4. Palevičius, Paulius; Ragulskis, Minvydas Kazys. Image communication scheme based on dynamic visual cryptography and computer generated holography // Optics Communications. Amsterdam : Elsevier. ISSN 0030-4018. 2015, vol. 335, p. 161-167. DOI: 10.1016/j.optcom.2014.09.041. [Science Citation Index Expanded (Web of Science); Academic Search Premier; COMPENDEX; Science Direct]. [0,500]. [IF (E): 1,542 (2013)]

Publications in peer-reviewed journals and conferences:

1. Palevičius, Paulius; Saunorienė, Loreta; Ragulskis, Minvydas Kazys. A secure communication system based on self-organizing patterns // SAM 2012 : proceedings of the 2012 International Conference on Security & Management, July 16-19, 2012, Las Vegas Nevada, USA. [S.l.] : CSREA Press, 2012, ISBN 1601322305. p. 421-426. [0,333]

2. Palevičius, Paulius; Ragulskis, Minvydas Kazys; Janušas, Giedrius; Palevičius, Arvydas. A technique for the reconstruction of a map of continuous curves from interference fringes // Proceedings of SPIE [elektroninis išteklius] : 2nd international conference on applications of optics and photonics / Edited by Manuel Filipe P. C. Martins Costa, Rogério Nunes Nogueira. Bellingham : SPIE. ISSN 0277-786X. 2014, vol. 9286, art. 92861G, p. [1-8]. DOI: 10.1117/12.2060743. [Conference Proceedings Citation Index]. [0,250]

3. Palevičius, Paulius; Ragulskis, Minvydas Kazys; Palevičius, Arvydas. Applicability of time-averaged holography for reliability assessment of chemical sensors // Nanotechnology in the security systems : NATO advanced research workshop on nanotechnology in the security systems, Yalta, Ukraine, September 29 - October 03, 2013 / Edited by J. Bonča, J. Kruchinin. Dordrecht : Springer Science+Business Media, 2015. (NATO Science for Peace and Security Series C: Environmental Security, ISSN 1874-6519), ISBN 9789401790048. p. 193-203. DOI: 10.1007/978-94-017-9005-5_17. [Conference Proceedings Citation Index; SpringerLINK]. [0,333]

4. Ragulskienė, Jūratė; Palevičius, Paulius; Maskeliūnas, Rimas; Stankūnas, Jonas; Maskeliūnas, Vytautas. Quality assessment of book covers using shadow moiré technique // Vibroengineering Procedia : international conference Vibroengineering - 2014, Katowice, Poland, 13-15 October, 2014. Kaunas : JVE International. ISSN 2345-0533. 2014, vol. 3, p. 283□287. [Compendex; Scopus]. [0,200]

ACKNOWLEDGEMENTS

I would like to express my special appreciation and thanks to my advisor Professor Dr. Minvydas Ragulskis, for encouraging my research and for allowing me to grow as a research scientist. Your advice on research as have been priceless and your guidance helped me in all the time of research and writing of this thesis.

I am grateful to the staff of the Department of Mathematical Modeling and KTU for the opportunity to aspire the PhD studies.

The depth of my feeling and gratitude is sent to my wife, family, relatives, and friends. Thank you for your patience, support and love.

I also place on record, my sense of gratitude to one and all, who directly or indirectly, have helped me during research and writing this thesis.

UDK 531.715:621-181.48(043.3)
SL344. 2015-05-26, 6 leidyb. apsk.1. Tiražas 12 egz. Užsakymas 150187.
Išleido leidykla „Technologija“, Studentų g. 54, 51424 Kaunas.
Spausdino leidyklos „Technologija“ spaustuvė, Studentų g. 54, 51424 Kaunas